

Metal-Induced Fluorescence Quenching in Carbon Dots for Sensing Applications

Farah Noun

A Thesis  
in  
The Department  
of  
Chemistry and Biochemistry

Presented in Partial Fulfillment of the Requirements  
for the Degree of Master Science (Chemistry) at  
Concordia University  
Montréal, Québec, Canada

August 2020

© Farah Noun, 2020

**CONCORDIA UNIVERSITY**

**School of Graduate Studies**

This is to certify that the thesis prepared

By: Farah Noun

Entitled: Metal-Induced Fluorescence Quenching in Carbon Dots for Sensing Applications

and submitted in partial fulfillment of the requirements for the degree of

**Master of Science (Chemistry)**

complies with the regulations of the University and meets the accepted standards with respect to originality and quality.

Signed by the final examining committee:

\_\_\_\_\_  
Dr. Jung Kwon Oh Chair

\_\_\_\_\_  
Dr. Yves Gélinas Examiner

\_\_\_\_\_  
Dr. Christopher Wilds Examiner

\_\_\_\_\_  
Dr. Rafik Naccache Supervisor

Approved by:

\_\_\_\_\_  
Dr. Yves Gélinas, Graduate Program Director

13 August, 2020

\_\_\_\_\_  
Dr. Pascale Sicotte, Dean of the Faculty of Arts and Science

## Abstract

Metal-Induced Fluorescence Quenching in Carbon Dots for Sensing Applications

Farah Noun

Overexposure to metals can induce adverse health and environmental effects, thus monitoring metal concentrations is crucial. While current detection techniques are highly sensitive, they come at elevated costs, which limit their global use. As such, cheap and accessible sensors, providing both sensitivity and selectivity, are in high demand. With high surface area-to-volume ratios, tunable fluorescence and surface chemistries, nanoparticles are under investigation for development as metal sensors. However, many challenges exist including photobleaching, toxicity and a lack of selectivity.

Owing to their low cytotoxicity, water-dispersibility and photostability, carbon dots have emerged as interesting alternatives. These amorphous carbon-based particles are ~10 nm in diameter and mainly composed of carbon, oxygen and hydrogen. While they have been investigated in metal sensing applications, the focus remains primarily on the application rather than the fundamental understanding of the mechanism of carbon dot-metal interactions in solution.

In this work, we study the synthesis of carbon dots using several cheap and accessible precursors resulting in a surface decorated with functional groups such as amines, carboxylic acids and thiols. Following extensive purification protocols aimed at removing impurities that could bind to metal cations, we evaluate how these surface groups impact metal-carbon dot interactions. We demonstrate that some of our systems evidence sensitivity to  $\text{Pb}^{2+}$  and  $\text{Hg}^{2+}$  and exploit our knowledge of charge density and hard-and-soft acid-base theory to explain these findings and the underlying mechanism. This work provides a better understanding of metal-carbon dot interactions, which can allow us to design more sensitive and selective optical probes.

## Acknowledgements

I am incredibly grateful to my supervisor, Dr. Rafik Naccache, who took a chance on me and allowed me to become one of his first graduate students. I would never have been able to complete this degree without his continual guidance, support, kindness and understanding. Without any senior graduate students to guide us in a brand-new lab, Dr. Naccache took it upon himself to train us and teach us the skills required in academia. Looking back to where I started, with little lab experience and even less research skills, I'm in awe of the progress I have made thanks to him. Your dedication to your students and to your research remain unmatched. I will always look up to you as both an incredible supervisor and an even more wonderful person.

I would also like to thank my committee members, Dr. Yves Gélinas and Dr. Christopher Wilds, who have continually guided me and supported me throughout the various challenges of my degree. I am grateful to their invaluable contributions to my work and to my education.

I am also grateful to the entire faculty and staff in the Department of Chemistry and Biochemistry at Concordia University for their help and support throughout my graduate studies. In particular: Maria Ciaramella, Lisa Montesano, Marika Dochia, Dr. Christine DeWolf, Dr. Louis Cuccia, Dr. John Capobianco, Rolf Schmidt, Vincent Lau, Khalil Rahman, Neema Chirwa, and Zornitsa Stoyanova have been instrumental in helping me succeed.

To my colleague, Dr. John Manioudakis, you have helped me grow as both a person and a scientist. Your guidance, friendship, honesty and support have pushed me to go further than I had thought possible. Despite what some may think, including you, you have been a great influence on me and on many of my colleagues in the Naccache Lab.

My friends, I always knew that with you, I had a safe place to go when I felt overwhelmed.

I enjoyed every movie night, every boardgame weekend and every birthday party and picnic together. A special thank you to my Swim Team<sup>+</sup>, especially Melissa, Cameron, Nugent, Margaret and Frontenac.

Nadine, you have always stood by me and been there to help when I made mistakes or when I had no one else to turn to. Your friendship has changed my life and I thank you for it.

To my siblings, Moussa, Nada and Sami, you have all helped me grow, and your love and support have been *superior!* to anyone else's. Most importantly, you have taught me not to always take things so seriously. I would especially like to thank my parents for the many sacrifices they have made to allow me to lead the life I live today. I wish only to make you proud of the daughter you have raised.

انا احبكما ماما و بابا

To my fiancé, JR, your friendship, love and support are what helped me through the most challenging periods. You never stopped believing in me. I hope to show you the same devotion for the rest of our lives together. *Mahal Kita*.

Although I am eternally thankful to all those who have supported me unconditionally, I would also like to thank those who have challenged me the most, for they too are my teachers.

## Contribution of Authors

Chapter 1 discusses the properties of carbon dots based on a co-authored invited review paper. This work is published as: de Medeiros, T. V.; Manioudakis, J.; **Noun, F.**; Macairan, J.-R.; Victoria, F.; Naccache, R., Microwave-assisted synthesis of carbon dots and their applications. *Journal of Materials Chemistry C* **2019**, 7 (24), 7175-7195. I was responsible for writing the section on the use of carbon dots in solar cell applications.

Chapter 3 in this thesis, *The Role of Purification in Carbon Dot Synthesis*, is based on published work that was co-authored with Dr. John Manioudakis. This work is published as a cover article: **Noun, F.**; Manioudakis, J.; Naccache, R., Towards Uniform Carbon Dot Properties, *Particle and Particle Systems Characterization*, **2020** (ppsc.202000119R1 – *in press*). Both Dr. Manioudakis and I are co-first authors and have contributed equally to this work. Dr. Manioudakis conceived the idea and ran initial experiments; however, upon his departure from the University, I took over the project completing the experimentation and data analysis. I was responsible for writing the manuscript and editing the entire text, graphs and images. Dr. Manioudakis assisted in writing the results and discussion, as well as in conceptualizing and producing some of the figures.

Chapter 4 is based on metal sensing in solution and our efforts to investigate the mechanism of carbon dot-metal quenching. A draft of the manuscript is near completion: **Noun, F.**; Naccache, R., Elucidating the Quenching Mechanism in Carbon Dot-Metal Interactions – Designing Sensitive and Selective Optical Probes, *Sensors* (4Q2020 Submission).

## Table of Contents

List of Figures .....	x
List of Tables .....	xiv
List of Equations .....	xv
List of Abbreviations .....	xvi
Chapter 1. Introduction .....	1
1.1. Metal Contamination .....	1
1.2. Conventional Metal Sensing Techniques.....	5
1.3. Nanoparticle Metal Sensors .....	8
1.4. Carbon Dots .....	16
1.5. Statement of the Problem.....	20
1.6. Project Objectives .....	21
Chapter 2. Materials and Methods .....	23
2.1. Chemicals and Reagents .....	23
2.2. Synthesis of CDs.....	23
2.2.1. Synthesis of Citric Acid and Ethylenediamine CDs .....	23
2.2.2. Synthesis of Citric Acid and Diethylenetriamine CDs .....	24
2.2.3. Synthesis of Formamide and Glutathione CDs.....	25
2.3 Characterization and Quenching Evaluation Techniques .....	25
2.3.1 FTIR-ATR.....	26
2.3.2. Transmission Electron Microscopy (TEM) .....	26
2.3.3. X-ray Photoelectron Spectroscopy (XPS) .....	26
2.3.4. X-Ray Diffraction (XRD).....	26
2.3.5. Zeta Potential .....	27
2.3.6. Absorbance Spectroscopy .....	27
2.3.7. Fluorescence Spectroscopy .....	27
2.3.8. Quantum Yield Determination.....	28
2.3.9. Fluorescence Lifetimes .....	28
2.4. Quenching Assays.....	28
Chapter 3. The Role of Purification in Carbon Dot Synthesis.....	31
3.1. The Challenges Encountered in the Literature.....	31

3.2. Monitoring the CD Surface Throughout purification .....	33
3.3. Optical Properties as a Function of Purification .....	36
3.3.1. Discerning Differences Through Absorbance Spectroscopy .....	36
3.3.2. How Fluorescence Can Be Misleading.....	39
3.3.3. Seeking the Answers in Fluorescence Quantum Yield Analysis.....	41
3.3.4. Insights Into Purification Through Photostability and Photobleaching.....	44
3.4. The Importance of Tailoring Purification Protocols.....	47
Chapter 4. Metal Sensing.....	48
4.1. Characterization .....	48
4.1.1 Exploring Differences in Size and Composition .....	48
4.1.1.1. Single-Fluorescent CDs .....	48
4.1.1.2. Dual-Fluorescent CDs.....	52
4.1.2. Investigating the Optical Properties.....	57
4.1.2.1. Single-Fluorescent CDs .....	57
4.1.2.2. Dual-Fluorescent CDs.....	58
4.2. Single vs. Dual-Fluorescent Systems.....	60
4.3 Optimizing and Determining the Quenching Capabilities of CDs .....	62
4.3.1. Metal Selection .....	62
4.3.2. Time Dependence .....	63
4.3.3. Concentrations .....	64
4.3.5. Water vs. Buffer.....	67
4.3.6. Water Contamination .....	68
4.3.7. Water Dilution Effects .....	70
4.3.8. Quenching Assay Results .....	72
4.3.8.1. Mercury Assay .....	72
4.3.8.2. Lead Assay.....	74
4.3.8.3. Chromium, Cobalt, Copper, Nickel, Iron, Gadolinium & Dysprosium.....	75
4.4. Quenching Mechanism .....	77
4.4.1. Absorbance Spectra .....	77
4.4.2. Fluorescence Lifetimes .....	78
4.4.3. Temperature Studies .....	79

4.5. The Root of Metal-CD Interactions .....	81
Chapter 5. Conclusion & Future Works .....	84
References.....	87
Appendix.....	95

## List of Figures

<b>Figure 1:</b> Diagram showing possible causes of decreased magnesium levels in the body (left) with the direct (top right) and indirect (bottom right) effects that can lead to osteoporosis. Image source: Castiglioni et. al. <sup>3</sup> .....	1
<b>Figure 2:</b> Pie chart showing the global percent usage of lead for various products in 2018. Image source: Natural Resources Canada. <sup>17</sup> .....	2
<b>Figure 3:</b> Global renewable energy generation (in TWh) from 1965 to 2018. Image source: Hannah Ritchie and Max Roser. <sup>22</sup> .....	3
<b>Figure 4:</b> Location of the Ring of Fire in northern Ontario. Image source: Noront Resources Ltd. <sup>28</sup> .....	5
<b>Figure 5:</b> Diagram showing conventional metal sensing techniques including Flame AAS, ICP-AES and ICP-MS. Image source: Hazel Davidson. <sup>32</sup> .....	7
<b>Figure 6:</b> Illustrated representation of the SPR phenomenon, showing changes in absorbance due to NP size, shape and material. Image source: Hyeon-Ho Jeong. <sup>47</sup> .....	9
<b>Figure 7:</b> (A) Graphical representation of a 3MPS-stabilized silver NP with (B) a graph showing changes in absorbance as a function of changing SPR due to the presence of Ni <sup>2+</sup> . Image source: Proposito et. al. <sup>44</sup> .....	10
<b>Figure 8:</b> Graphical summary of the differences between static and dynamic quenching. ....	14
<b>Figure 9:</b> (A) TEM image of the CdTe QDs (B) Plot showing quenching of fluorescence with the addition of increasing concentrations of Cr <sup>3+</sup> . Image source: Elmizadeh et. al. <sup>55</sup> .....	15
<b>Figure 10:</b> Graphical illustration of the increasing bandgap with decreasing CD size in the quantum confinement effect. ....	19
<b>Figure 11:</b> Graphical illustration of the core and surface states fluorescence mechanism, showing the possibility of energy transfers between the two states. ....	20
<b>Figure 12:</b> Graphical representation of the purification process of DT3-CDs showing all sample aliquots being kept for analysis and the purification methods they were subjected to. ....	24
<b>Figure 13:</b> Demonstrating the effect of purification on the surface chemical moieties of CDs using FTIR. Stacked FTIR spectra are shown at different purification stages for 750DT3 (A-C) and 375DT3 CDs (D-F). The spectra showcase bands ascribed to amide, carboxylic acid carbonyls, as well as C=C/N-H groups. Following extensive purification, the spectra display a notable increase in the carboxylic acid carbonyl band (1705 cm <sup>-1</sup> ) for both CD systems, in addition to a discernable increase in band resolution. ....	35
<b>Figure 14:</b> Effect of purification on the optical properties of CDs. Overlay of UV/Vis spectra at different purification stages for 375DT3 (A, B and C) and 750DT3 CDs (D, E and F), where absorbance has been adjusted to 0.2 a.u. at 350 nm for all samples. The spectra exhibit 2 main peaks at 240 and 350 nm, corresponding to the $\pi \rightarrow \pi^*$ and $n \rightarrow \pi^*$ transitions, respectively. The dialysates exhibit the starkest changes for both systems as impurities and smaller, incomplete fluorophores and CDs are successively dialysed out. This is reflected in the purified samples as sharper bands centered at 240 and 350 nm. ....	38

**Figure 15:** Selected fluorescence contour plots of samples normalized to 0.1 a.u. absorbance at 350 nm chosen to highlight spectral differences. The contour plots for the dialysate after the first and fifth dialysis step for the 375DT3 sample (**A & B**) and the 750DT3 sample (**C & D**). The contour plots both before and after a full series of dialysis without any organic washes for 375DT3 CDs (**E & F**) and 750DT3 CDs (**G & H**). The contour plots both before and after a full series of dialysis followed by organic washes for 375DT3 CDs (**I & J**) and 750DT3 CDs (**K & L**)...... 40

**Figure 16:** Effect of purification on the photoluminescence quantum yield values of CDs. Graphical representation of the changes in fluorescence quantum yield for (**A**) 375DT3 and (**B**) 750DT3 CDs, respectively. (**C**) Tabulation of quantum yield values for 375DT3 and 75750DT3 CDs at each step of the purification process. The results illustrate that similar systems may yield drastically different purification profiles. .... 42

**Figure 17:** Graphic representation of the dialysis purification profile for crude 750DT3 CDs. Four main constituents comprise the crude sample, as described in the figure legend. Dialysis successively removes small, low QY particles, which increase the QY to its maximum value of 77.8% for Dialysate #3. Subsequent dialysis steps remove most high QY fluorophores and incomplete CDs, ultimately levelling off at ~63%. Proportions of the different components are for illustrative purposes only. .... 43

**Figure 18:** Plot and accompanying table showing percent fluorescence remaining compared to initial fluorescence intensity at 445 nm emission maximum after direct exposure to a 365 nm light source for a varying number of hours of 750DT3 CDs. .... 45

**Figure 19:** TEM image and size distribution plot of (**A**) ED2-CDs and (**B**) DT3-CDs alongside the (**C**) XRD patterns for both CDs. Images adapted from: Manioudakis *et. al.*<sup>64</sup> ..... 49

**Figure 20:** FTIR spectrum of (**A**) ED2-CDs and (**B**) DT3-CDs showing the presence of amide and carboxyl stretches as well as N-H, C-H and O-H functional groups. .... 50

**Figure 21:**(**A**) TEM image of FG-CDs with in-laid size distribution plot showing an average size of  $7.3 \pm 1.2$  nm. (**B**) XRD pattern of FG-CDs showing an amorphous halo. .... 53

**Figure 22:** FTIR spectrum of FG-CDs showing the presence of amide and carboxyl stretches as well as N-H and O-H functional groups. .... 53

**Figure 23:** (**A**) XPS survey spectrum of FG-CDs showing binding energies of C1s, N1s, O1s and S2p. Spectra of deconvoluted binding energies reveal (**B**) a maximum for C1s at 286.08 eV, (**C**) a maximum at 400.08 eV for N1s (**D**) a maximum at 532.08 eV for O1s and (**E**) for S2p a maximum at 165.08 eV. .... 55

**Figure 24:** UV-vis and overlaid fluorescence spectrum for (**A**) ED2-CDs and (**B**) DT3-CDs. Both absorbance spectra show a  $\pi \rightarrow \pi^*$  electronic transition at ~245 nm and a  $n \rightarrow \pi^*$  transition at ~350 nm. Fluorescence shows a single emission at ~445 nm in both spectra when excited at 350 nm. .... 57

**Figure 25:** (**A**) The UV-Vis absorption spectrum of FG-CDs shows three main electronic transition regions: a  $\pi \rightarrow \pi^*$  transition at ~300 nm; a  $n \rightarrow \pi^*$  transition at ~420 nm ; and a  $n \rightarrow \pi^*$  transitions from 600 to 700 nm. (**B**) The fluorescence spectrum of FG-CDs shows dual emission at 485 nm and 680nm, with a shoulder at 650 nm. .... 59

**Figure 26:** (**A**) Graphical representation of the single-fluorescent CD spectrum (**B**) Integrated area under the curve of the single-fluorescent CD system before and (**C**) after a reduction of the peak

intensity **(D)** Graphical representation of the dual-fluorescent CD system **(E)** Integrated area under the curve of the dual-fluorescent CD system before and **(F)** after a reduction of the peak intensity. .... 61

**Figure 27:** Fluorescence spectra of a 1.25 µg/mL DT3-CD solution with 30 µM of cobalt (II) ions showing no time dependence over a 20 minute interval with accompanying table listing fluorescence intensity values over time. .... 64

**Figure 28:** Ratio of the integrated fluorescence area, relative to the original fluorescence values, of 4.5, 2.5 and 1 µg/mL ED2-CD solutions with 1 µM concentrations of different metal cations. .... 65

**Figure 29:** Quenching assay data for 2.5 µg/mL of ED2-CDs with concentration range from 0 – 1mM showing **(A)** absorbance spectra with evidence of inner-filter effect and **(B)** fluorescence spectra with excitation wavelength of 350 nm for maximum emission at 450 nm. .... 66

**Figure 30:** **(A)** Fluorescence spectra of a solution of 35 µg/mL of FG-CDs in the presence of increasing concentrations of lead (II) ions **(B)** Linear trend of the decreasing fluorescence area ratio for FG-CDs showing poor linearity..... 67

**Figure 31:** **(A)** Fluorescence spectra of 30 µg/mL of FG-CDs in PBS buffer with increasing concentrations of Hg<sup>2+</sup> **(B)** Plotted R/B ratio of FG-CDs as a function of metal concentration, showing a decreasing and poorly linear trend..... 68

**Figure 32:** Absorbance spectrum for FG-CDs with the addition of ~ 1000 nM Pb<sup>2+</sup> **(A)** Previously obtained data, showing a peak at 475 nm associated with the lead-CD complex<sup>96</sup> **(B)** repeated in contaminated MilliQ water showing only a very small peak at 475 nm **(C)** repeated in LC-MS water, free of metal contaminants, showing a strong peak at 475 nm. .... 69

**Figure 33:** A dilution control experiment with water was performed on 35 µg/mL FG-CDs showing **(A)** fluorescence spectra with a significant changes as a function of volume of water added and **(B)** the corresponding R/B ratio plot showing a decreasing trend down to 90% of the original R/B ratio value..... 70

**Figure 34:** Absorbance spectra for dilution control experiment with water performed on 35 µg/mL FG-CDs. .... 71

**Figure 35:** Plots showing R/B ratio as a function of metal concentration **(A)** before and **(B)** after water dilution correction. .... 72

**Figure 36:** Results of a FG-CD quenching assay with mercury (II) ions showing **(A)** the absorbance spectrum with a decrease in the 420 nm peak and the appearance of a new peak at ~ 450 nm related to the CD and mercury complex, **(B)** the fluorescence spectra showing changes in the 650 and 680 nm peak while the 485 nm peak remains unaffected by the presence of metal cations **(C)** the linear plot of the decreasing overall R/B area ratio with an r<sup>2</sup>=0.97..... 73

**Figure 37:** Results of a FG-CD quenching assay with lead (II) ions showing **(A)** the absorbance spectrum with a decrease in the 420 nm peak and the appearance of a new peak at ~ 475 nm related to the CD and lead complex, **(B)** the fluorescence spectra showing changes in the 650 and 680 nm peak while the 485 nm peak remains unaffected by the presence of metal cations **(C)** the linear plot of the decreasing overall R/B area ratio with an r<sup>2</sup>=0.98..... 74

**Figure 38:** R/B area ratio of FG-CDs with 1000 nM of various metallic cations showing comparison of quenching effectiveness. .... 75

**Figure 39:** Results of a FG-CD quenching assay with iron (III) ions showing (A) the absorbance spectrum with a smaller decrease in the 420 nm peak than the metal quenching assays performed with lead (II) and mercury (II) ions (B) the fluorescence spectra showing changes in the 650 and 680 nm peak while the 485 nm peak remains unaffected by the presence of metal cations (C) the R/B area ratio showing fluctuations in R/B area ratio values without a significant trend. .... 76

**Figure 40:** Absorbance spectra for FG-CDs (A) alone, (B) showing a new peak at ~450 nm in the presence of Hg<sup>2+</sup>, and (C) at ~ 475 nm in the presence of Pb<sup>2+</sup> ..... 77

**Figure 41:** Absorbance spectra of FG-CDs showing changes as a function of increasing temperatures (A) with 0 nM of Hg<sup>2+</sup> (B) with 1000 nM of Hg<sup>2+</sup> ..... 80

## List of Tables

<b>Table 1:</b> Tables of masses used to prepare metal salt solutions used in the quenching assays....	29
<b>Table 2:</b> Volumes of metal solution added to 8 mL CD samples during post-optimization quenching assays.....	30
<b>Table 3:</b> Summary of characterization for ED2-CDs showing (A) the functional groups observed from FTIR analysis (B) the functional groups observed from XPS analysis and (C) the elemental composition of the dots.....	51
<b>Table 4:</b> Summary of characterization for DT3-CDs showing (A) the functional groups observed from FTIR analysis (B) the functional groups observed from XPS analysis and (C) the elemental composition of the dots.....	52
<b>Table 5:</b> Summary of characterization for FG-CDs showing (A) the functional groups observed from FTIR analysis (B) the functional groups observed from XPS analysis and (C) the elemental composition of the dots.....	56
<b>Table 6:</b> Summary of the fluorescence lifetime values for ED2-CDs and DT3-CDs with populations.....	58
<b>Table 7:</b> Fluorescence lifetimes of FG-CDs at various concentrations of mercury (II) ions.....	78
<b>Table 8:</b> Fluorescence lifetimes of FG-CDs at various concentrations of lead (II) ions. ....	79
<b>Table 9:</b> Classification of various ions based on the HSAB theory. Table adapted from: EPA <sup>138</sup> .....	81
<b>Table 10:</b> Charge, ionic radii and charge densities of tested metal cations. Table adapted from: Rayner-Canham <sup>127</sup> .....	83

## List of Equations

<b>Equation 1:</b> The relationship between fluorophores and quenchers in static quenching.....	12
<b>Equation 2:</b> Lifetimes in a statically quenched system.....	12
<b>Equation 3:</b> The relationship between fluorophores and quenchers in dynamically quenched systems.....	13
<b>Equation 4:</b> The dependence of $k_q$ on quenching efficiency and diffusion-controlled bimolecular rate constant. ....	13

## List of Abbreviations

<b>AAS</b>	Atomic Absorption Spectroscopy
<b>AES</b>	Atomic Emission Spectroscopy
<b>CDs</b>	Carbon Dots
<b>DET</b>	Dexter electron transfer
<b>DOM</b>	Dissolved organic matter
<b>DT3</b>	Diethylenetriamine
<b>ED2</b>	Ethylenediamine
<b>FGCDs</b>	Formamide and glutathione-based CDs
<b>FLT</b>	Fluorescence Lifetime
<b>FRET</b>	Förster resonance energy transfer
<b>FTIR</b>	Fourier-transform infrared
<b>GNR</b>	Gold Nanorods
<b>ICP</b>	Inductively Coupled Plasma
<b>LOD</b>	Limit of Detection
<b>MS</b>	Mass Spectrometry
<b>MWCO</b>	Molecular weight cut-off
<b>NIR</b>	Near-infrared
<b>NP</b>	Nanoparticle
<b>PBS</b>	Phosphate buffered saline
<b>PDs</b>	Polymer Dots
<b>PET</b>	Photoinduced electron transfer
<b>QDs</b>	Quantum Dots
<b>QY</b>	Quantum yield
<b>SP</b>	Surface plasmon
<b>SPR</b>	Surface plasmon resonance
<b>TEM</b>	Transmission electron microscopy
<b>XPS</b>	X-ray photoelectron spectroscopy
<b>XRD</b>	X-ray diffraction

# Chapter 1. Introduction

## 1.1. Metal Contamination

Metals play a vital role in our everyday life and are required for many bodily functions. A well known example of this is iron, which is found in hemoglobin in our blood and is necessary for transporting oxygen and carbon dioxide throughout the body.<sup>1, 2</sup> Magnesium is another important metal that is essential for maintaining healthy bones.<sup>3</sup> Bones act as a reservoir of elements including magnesium and calcium, where there is a constant exchange with the rest of the body through an on-going bone formation and destruction process. When magnesium intake is too low, this directly causes the formation of larger hydroxyapatite crystals within the bones, which leads to osteoporosis through a weaker bone structure. Low magnesium intake also promotes the formation of osteoclasts, cells that break down bones, pushing the body's natural equilibrium towards bone loss.<sup>3</sup> Other indirect effects of low magnesium levels can be seen in Figure 1. Finally, chromium has been shown to help maintain healthy glucose levels.<sup>4</sup> A rise in blood sugar levels causes the release of chromium ions in the blood stream which then bind to an oligopeptide called

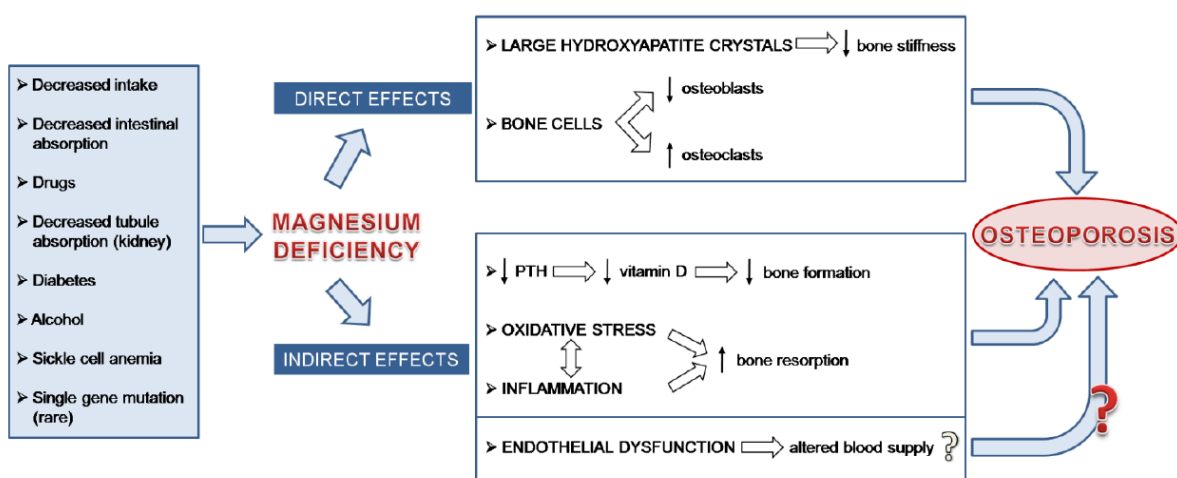


**Figure 1:** Diagram showing possible causes of decreased magnesium levels in the body (left) with the direct (top right) and indirect (bottom right) effects that can lead to osteoporosis. Image source: Castiglioni et. al.<sup>3</sup>

Chromodulin. Once this binding is complete, Chromodulin can itself bind to insulin receptors triggering an auto-amplification mechanism in insulin signaling.<sup>4-6</sup> While metals are clearly necessary for our biological functions, above certain threshold concentrations<sup>7</sup>, they can become toxic and have many adverse effects on the human body. Among these effects are reduced growth and development, peripheral neuropathy, organ failure, and cancer.<sup>7-10</sup> More concerningly, unlike organic contaminants, the metal ones do not degrade, but simply accumulate both within our bodies and within the environment, a process referred to as bioaccumulation.<sup>11, 12</sup> Moreover, moving up in the food chain, metal contaminants are further amassed from the consumption of contaminated prey. Thus, the higher along the food chain an animal is, the greater the bioaccumulation, which itself is a phenomenon called biomagnification.<sup>13</sup> In many cases, natural processes such as weathering of metal-containing rocks and volcanic eruptions are important sources of environmental metal contamination.<sup>14</sup> This is especially true in areas where there exists a large reserve of metal ores, thus causing a natural abundance of a metal that can leech into the environment. This is the case for iron contamination in many places in Canada, a country that possesses the 6<sup>th</sup> most crude iron ore reserves in the world.<sup>15</sup> However, this issue is often times

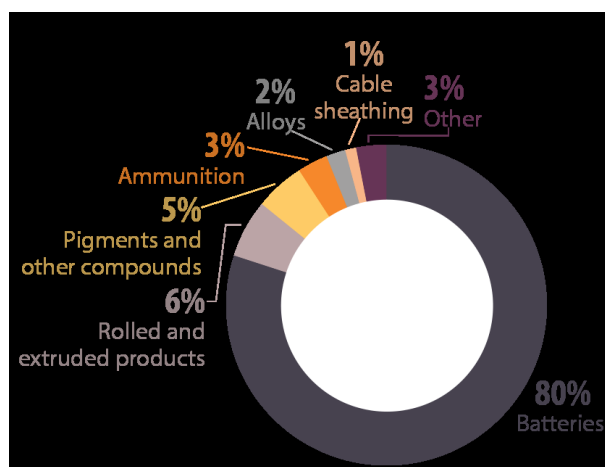


**Figure 2:** Pie chart showing the global percent usage of lead for various products in 2018. Image source: Natural Resources Canada.<sup>17</sup>

significantly exacerbated by additional metal contamination sources from anthropogenic activities like mining, agriculture, industrial processes and urban run-off.<sup>8, 16</sup>

Canada is one of the leading producers and suppliers of refined lead, ranking as 8<sup>th</sup> in the world in 2018. Currently, the main uses of lead, shown in Figure 2, include car batteries, metallic wires, ribbons and extrusions, pigments, and ammunition.<sup>17</sup> Due to the large scale of lead production and use, it is an important source of lead contamination in soil, water and air in Canada. However, a main source of the lead found in tap water is its use in plumbing and distribution systems in many countries, including Canada, which utilized lead for its service lines until 1986.<sup>18</sup> To this day, much of this plumbing has yet to be replaced in areas like Montreal, resulting in potentially unsafe levels of lead in drinking water.<sup>19</sup> As such, food and water are the most common sources of lead exposure for Canadians.<sup>18</sup>

Mercury has not been mined in Canada since 1975.<sup>18</sup> In fact, in 2013, Canada signed the Minamata convention, which aims to reduce the use and supply of mercury to diminish

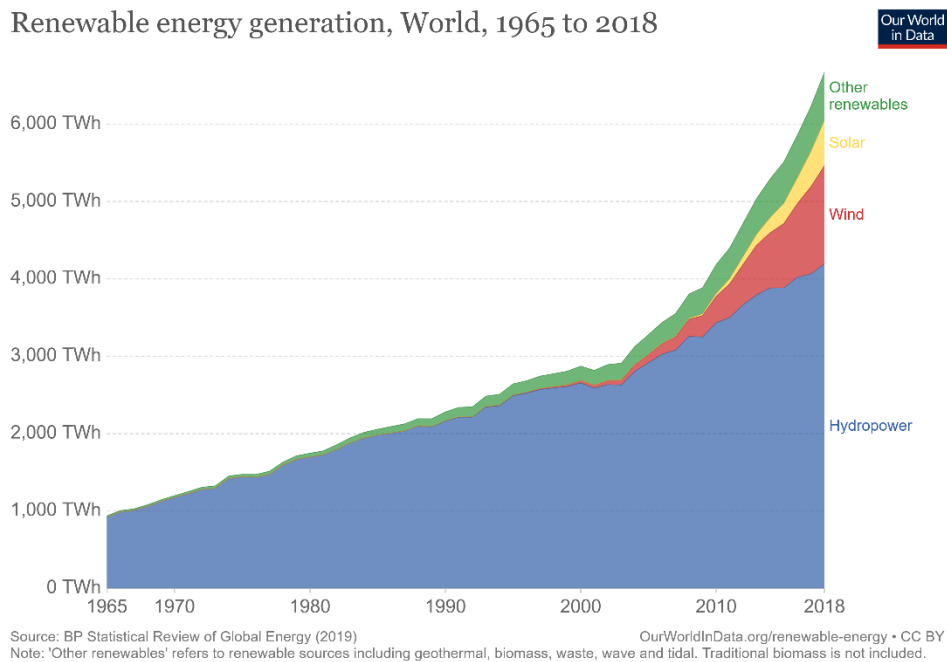


**Figure 3:** Global renewable energy generation (in TWh) from 1965 to 2018. Image source: Hannah Ritchie and Max Roser.<sup>22</sup>

environmental contamination with this notoriously toxic metal.<sup>20</sup> However, approximately 95% of anthropogenic mercury deposited in Canada is a result of long-range transportation from elsewhere in the world.<sup>13</sup> The main sources of mercury emission stem from by-products of coal-fired power plants and artisanal gold mining. In many countries, coal-fired power plants account for up to 50% (USA) to 75% (China) of energy production, with 1 mg of mercury contained in every kilogram of coal.<sup>20</sup> Moreover, artisanal gold miners in Latin America, Africa and Oceania, use mercury to form an amalgam with gold in gold-bearing mud, then heat the amalgam to evaporate the mercury, thus separating it from the gold. This process is thought to release 300 tonnes of mercury into the atmosphere every year.<sup>20</sup> Despite the on-going global transition towards renewable energy (see Figure 3) and the shift away from mercury-based products and processes,<sup>20-22</sup> the mercury released from its natural reserves, continually circulates in the atmosphere and in the environment leading to its possible long-range transportation and transformation into different forms, such as methylmercury, as well as its accumulation in soils, waters and foods, most notably seafood.<sup>13, 18,</sup>  
<sup>23</sup> Nearly all cases of mercury exposure in Canada and in the U.S., primarily in the form of methylmercury, come from the consumption of fish and shellfish.<sup>13, 23, 24</sup>

Nevertheless, growing global demands for metals and minerals have continually pushed the growth of the mining industry. Between 2005 and 2018, Canada's mining industry GDP more than doubled from 40 to 90 billion dollars, with the number of mining establishments growing from 859 to 1060.<sup>12</sup> Meanwhile, mineral exploration/appraisal spending has grown from 1.3 to 2.3 billion dollars, as additional places are explored as potential mining sites.<sup>12</sup> Natural Resources Canada's 2019 Major Natural Resource Projects Inventory shows that there were 114 new mineral projects

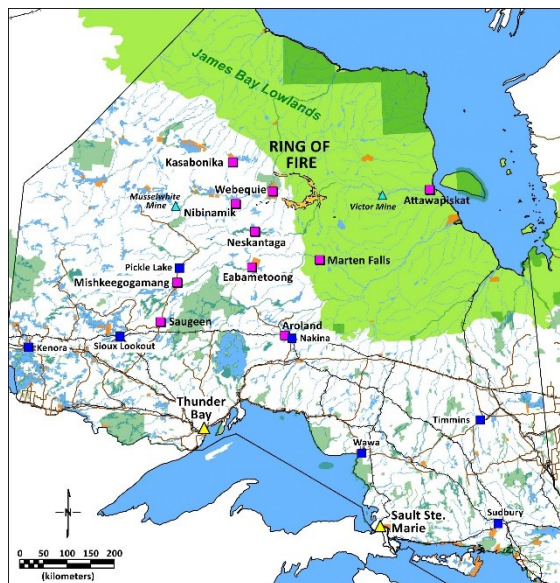


**Figure 4:** Location of the Ring of Fire in northern Ontario. Image source: Noront Resources Ltd.<sup>28</sup>

that were either planned or under-construction for the 2019-2029 time period.<sup>25</sup> One such project, the Ring of Fire (shown in Figure 4) aims to increase Canada’s chromium mining to compete with countries such as Kazakhstan and South Africa, which possess 95% of the world’s chromium mines.<sup>19-21.</sup><sup>26-28</sup>

Regardless of whether Canada’s metal contamination sources are natural, anthropogenic, local or foreign, the environmental and health concerns caused by this contamination remain the same. For this reason, and due to the forecasted increase in mining activities in Canada, it is more important than ever to track metal concentrations for the prevention and regulation of metal contamination.

## ***1.2. Conventional Metal Sensing Techniques***

Over the years, many techniques have been developed in order to detect of a wide variety of metals, while maintaining low limits of detection (LODs).<sup>29-31</sup> Figure 5 summarizes some of these methods.<sup>32</sup> One widely used quantitative technique is atomic absorption spectroscopy (AAS),

developed in 1955, where a flame or furnace is used to heat samples until complete atomization of its components.<sup>29, 31</sup> The absorbance is then measured for each metal atom of interest and can be correlated to its concentration in the sample.<sup>29</sup> Atomic absorption spectra present several different wavelengths of absorption in the UV and visible regions of the spectrum, which are unique to each atom. As such, atoms can be differentiated by one of their several wavelengths of absorption, which often do not overlap. Moreover, in the unusual case of spectral overlap between two atoms, a different absorption can be selected although in this case, some loss in sensitivity may be experienced.<sup>31</sup> This permits multi-element analysis of a sample containing more than one metal analyte.<sup>29</sup> Furthermore, this technique provides low LODs reaching low- to mid- ppb ranges with flame atomization and sub-ppb ranges when using a furnace for atomization.<sup>31</sup> AAS provides rapid and sensitive analysis of metal atoms in both liquid and solid samples.<sup>29, 31</sup> However, in the case of flame AAS, a large sample size is required and the sample must be in the solution phase. This is due to the fact that the sample is introduced into the system through continuous aspiration.<sup>31</sup> Thus, when working with small sample volumes, furnace AAS is preferred. However, the cost of new instruments ranges from 10,000\$-50,000\$ for flame AAS and 20,000\$-80,000\$ for furnace AAS, with additional costs for training and upkeep.<sup>31</sup> Moreover, this large instrumentation cannot be used for in-field analysis, and extensive sample preparation is required to avoid clogging of the nebulizer (in the case of flame AAS) and loss of sensitivity.<sup>29, 31</sup>

Another important technique is inductively couple plasma (ICP), which can be used in conjunction with atomic emission spectroscopy (AES) and mass spectrometry (MS). Similar to AAS, the sample is introduced into the system and heated using plasma to first atomize, then ionize metal analytes. The plasma, composed of hot, partially ionized gas with a high concentration of cations and electrons, provides better atomization than a flame or furnace due to its higher

temperature, which means less extensive sample preparation is required.<sup>30, 31</sup> When coupled with AES, ICP allows for rapid, multi-elemental detection in a single sample. When excited, the atoms

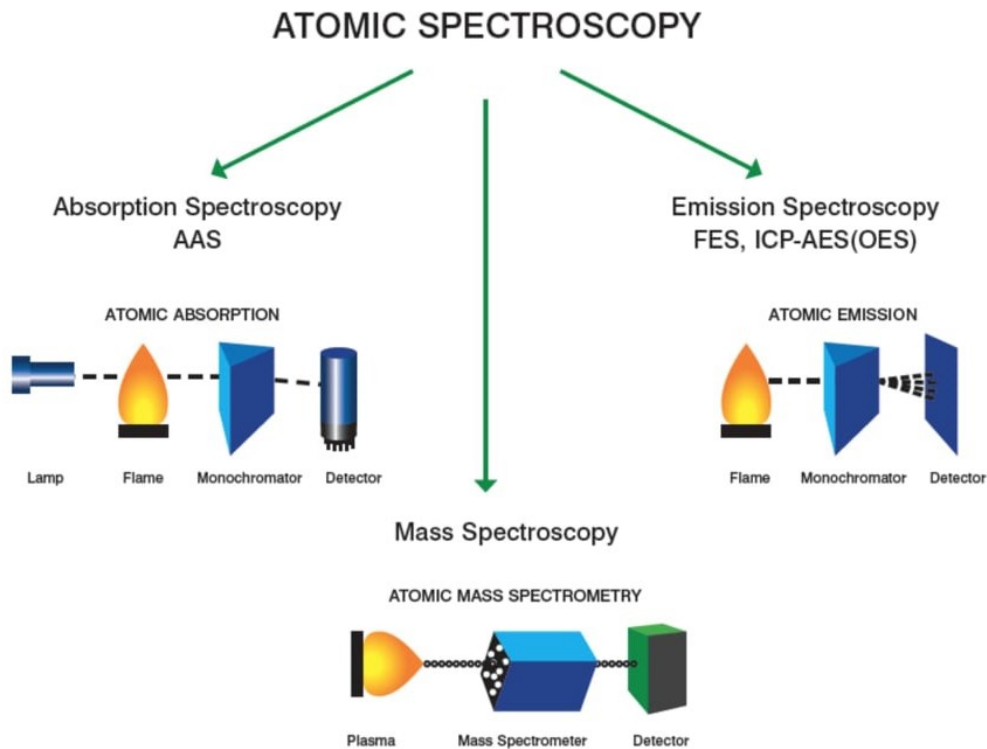


**Figure 5:** Diagram showing conventional metal sensing techniques including Flame AAS, ICP-AES and ICP-MS. Image source: Hazel Davidson.<sup>32</sup>

emit at specific wavelengths, which are used to determine the metals present within the sample. In some instruments, a multi-channel spectrometer can allow for simultaneous detection at several different wavelengths, reducing analysis time. However, there is always a risk of spectral overlap, which can be dealt with in the same way as in AAS (i.e. by choosing a different detection wavelength for the analyte).<sup>31</sup> ICP-AES provides detection limits in the low-ppb to sub-ppb range. Conversely, ICP-MS can have even lower LODs with the added possibility of isotope analysis.<sup>30, 31</sup> ICP suffers from many of the same drawbacks as AAS, including cost and the inability to perform in-field analysis. The cost of a new ICP system is in the range of \$55,000 to \$150,000 with system costs increasing to ~100,000\$ for ICP-AES and ~180,000\$ for ICP-MS, with even

higher costs for a multichannel system.<sup>31, 33</sup> This is of course coupled with the cost of running and maintaining the instrument with trained technicians. In addition to this, ICP also suffers from low ionization efficiency when working with natural water samples, which have a much more complex sample composition and a higher concentration of dissolved solids, thus lowering detection sensitivity.<sup>30</sup>

In many ways these exceptional instruments fulfill the need for accurate and sensitive metal detection. Still, they fall short when it comes to in-situ testing of water for metal contamination in remote areas, or in developing nations where such sophisticated instruments are not available and time cannot be spent sending samples back and forth to better equipped testing facilities.

### ***1.3. Nanoparticle Metal Sensors***

It is in this regard that an urgent need still exists for the development of cheap and sensitive metal sensing techniques with a possibility of use in remote or economically under-developed areas. With the development of new, portable technologies such as handheld fluorescence spectrometers<sup>34-36</sup>, the use of nanoparticle-based metal sensors has recently come under investigation. Nanoparticles (NPs) are defined as materials ranging in size from 1-100 nm in a single dimension, a size that imparts them with several interesting properties.<sup>11, 37-40</sup> NPs possess a high surface-area-to-volume ratio meaning a greater potential for interaction with analytes.<sup>37-41</sup> As most metal-NP interactions occur solely at the surface, NPs can be ideally suited in metal sensing applications. Some NP systems also have a versatile surface chemistry, which allows the surface groups to be modified pre- or post-synthesis to better target analytes of interest or to endow desired properties such as hydrophilicity.<sup>37, 38, 41-43</sup> In some cases, nanoparticles have been shown to have optical properties such as fluorescence, or surface plasmon resonance,<sup>11, 38, 40, 42, 43</sup> which can be advantageous for sensing through monitoring changes in the optical signature upon interaction with analytes of interest.<sup>11, 38, 39, 43</sup> Moreover, the optical properties can often be tuned by varying

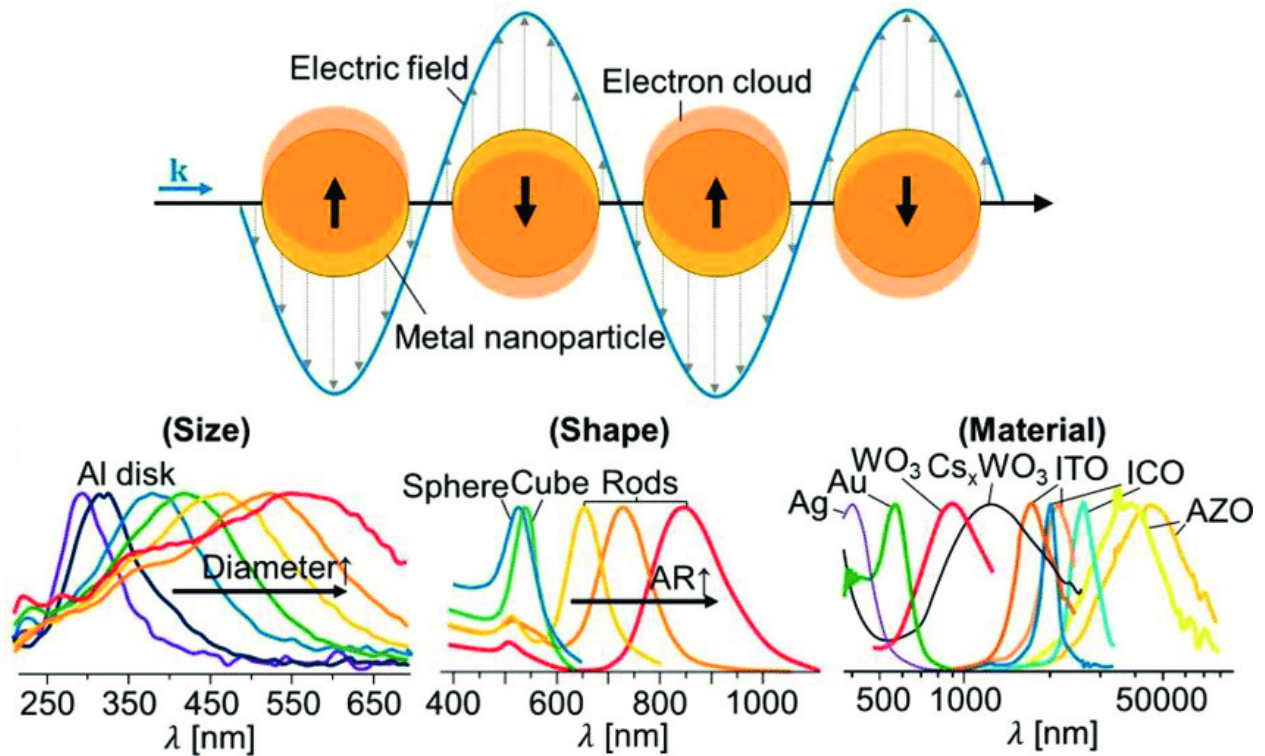


**Figure 6:** Illustrated representation of the SPR phenomenon, showing changes in absorbance due to NP size, shape and material. Image source: Hyeon-Ho Jeong.<sup>47</sup>

the size and composition of the nanomaterials allowing for specific design when targeting an application.<sup>38</sup> Recently, several NP systems have been investigated in the detection and sensing of metals in aqueous systems. Among these are metallic NPs, which possess a special optical property called surface plasmon resonance (SPR).<sup>40, 44, 45</sup> SPR is a phenomenon which occurs when light interacts with a thin metallic surface, as is the case with metallic NPs, causing the polarization of the electronic cloud on the surface of the particle. The resulting charge separation causes a linear restoring force by the positively charged nuclei. This creates a collective, in-phase oscillation of the NP's surface valence electrons, known as surface plasmon (SP). In the case that the natural frequency of this oscillation matches the frequency of the incident light, resonance is achieved, causing SPR. This creates an absorption band with a wavelength related to the size and shape of the NP in question as well as the dielectric constant of the medium directly in contact with the NP

surface, a process depicted in Figure 6.<sup>11, 40, 46, 47</sup> With the binding of an analyte to (or close to) the metallic surface, there is a change in the surrounding medium's index of refraction and inter-particle interactions, which alters the plasmonic resonance. This allows for the detection of target analytes through changes in SPR.<sup>11, 40, 46</sup> A first example of this phenomenon comes from Proposito *et. al.* who synthesized silver nanoparticles stabilized by sodium 3-mercaptopropene sulfonate (3MPS), illustrated in Figure 7A.<sup>44</sup> With the addition of nickel ions, changes in the SPR were observed via absorbance spectroscopy (shown in Figure 7B), which led to the quantitation of nickel cations within the sample. Proposito and their group determined an LOD of 0.3 ppm for

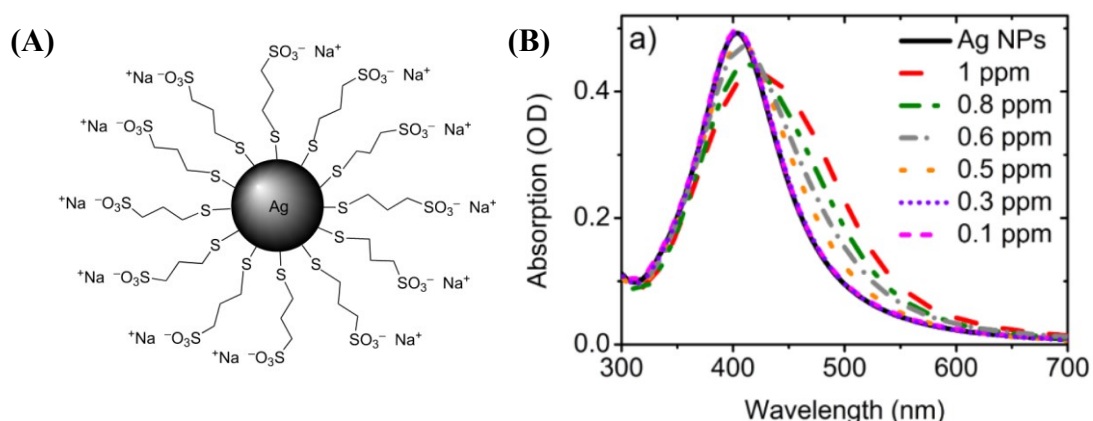


**Figure 7:** (A) Graphical representation of a 3MPS-stabilized silver NP with (B) a graph showing changes in absorbance as a function of changing SPR due to the presence of  $\text{Ni}^{2+}$ . Image source: Proposito *et. al.*<sup>44</sup>

$\text{Ni}^{2+}$  in water. A less significant response to  $\text{Cr}^{3+}$  was also observed while  $\text{Cu}^{2+}$ ,  $\text{Nd}^{3+}$  and  $\text{Ca}^{2+}$  produced no significant changes in the SPR.<sup>44</sup> Similarly, Huang *et. al.* synthesized gold nanorods (GNR) in the presence of cetyltrimethylammonium bromide (CTAB) to provide them with stability and a hydrophilic surface.<sup>48</sup> In this work, the  $\text{Hg}^{2+}$  ions in solution were first reduced to  $\text{Hg}^0$  by  $\text{NaBH}_4$  present in solution. It was explained that mercury would quickly deposit onto the gold due to their high affinities for each other. The authors also speculated that the longitudinal tips of the GNRs were where metal ions will accumulate, thus causing a pseudo-elongation of the GNR leading to changes in their SPR. This was observed through the spectral shifts in their absorbance

spectra. Their reported LOD for mercury was  $\sim 10^{-13}$  M (0.27 ppt).<sup>48</sup>

While they are effective, the use of metallic NPs for SPR-based metal sensing offers a number of drawbacks. Firstly, the use of gold or silver incurs significant costs for the production of these NPs, especially considering the relatively long and complex synthesis procedures required.<sup>49, 50</sup> Additionally, as the detection is based on spectral shifts in the absorbance which occur indiscriminately of the metal analyte, differentiation of the response to different metals is difficult.<sup>44</sup> Thus, the sensing of metals in real water samples where several different metal ions are present may be problematic. In the case of using gold NPs, their high affinity for mercury may hinder the detection of other metals present in solution. Lastly, some evidence also suggests that SPR-based nanosensors may be less sensitive in comparison to their fluorescence-based counterparts.<sup>38</sup>

Fluorescence-based nanosensors have indeed been extensively investigated for metal detection. At the nanoscale, semi-conductor nanomaterials such as quantum dots (QDs)<sup>51</sup>, carbon dots (CDs)<sup>43, 52</sup> and polymer dots (PDs)<sup>52</sup> exhibit fluorescence, which is absent in the bulk domain. Fluorescence-based detection of metal ions depends on fluorescence quenching through metal-NP interactions and can be categorized as static or dynamic quenching. In static quenching, a non-emissive complex is formed between the fluorophore (in this case, the NP) and the quencher (the metal cation). In this case, a previously emissive state is rendered non-emissive meaning that following excitation, the fluorophore returns to the ground state without the emission of a photon.<sup>53</sup><sup>54</sup> As such, the change in fluorescence of the system, that is the initial fluorescence over the fluorescence at a specific quencher concentration ( $F_0/F$ ), is solely a function of the concentration of the metal quencher, denoted as  $[Q]$ , and of the association constant of the newly formed metal quencher-NP complex,  $K_s$ . This constant is itself a ratio of the concentration of the formed

complex, [P-Q], over the concentrations of the NP and the metal denoted as [P] and [Q], respectively.<sup>53</sup> This relationship is shown in Equation (1):

$$\frac{F_0}{F} = 1 + K_s[Q] = 1 + \frac{[P-Q]}{[P][Q]}[Q] \quad (1)$$

Static quenching can be identified by a few characteristic properties. First, when a system is undergoing static quenching, the fluorescence lifetime (FLT) of the NP remains constant, regardless of the concentration of metal cations present. This occurs because the previously emissive states that are quenched become non-emissive, thus they no longer contribute to the FLT. As such, only the remaining unquenched particles, which are not in contact with the metals, are contributing to the FLT, so it remains the same.<sup>53, 54</sup> In such a case, the ratio of the initial lifetime ( $\tau_0$ ) over the lifetime at a given quencher concentration ( $\tau$ ), represented by Equation (2), will be equal to 1:

$$\frac{\tau_0}{\tau} = 1 \quad (2)$$

A second characteristic of this quenching mechanism is an observable change in the absorption spectrum due to the formation of a NP-Metal complex.<sup>53, 54</sup> Finally, this type of quenching also shows a temperature dependence. When the temperature is increased, the system is provided with more energy, thus the complex formed becomes more unstable. Hence, quenching declines as the complexes break apart.<sup>54</sup>

On the other hand, dynamic quenching, also known as collisional quenching, results from the energy transfer during a collision of the metal quencher and the excited-state NP which causes

the system to return to the ground state without emission of a photon.<sup>53, 54</sup> Dynamic quenching is an umbrella term which encapsulates several different mechanisms including: Förster resonance energy transfer (FRET), Dexter electron transfer (DET), and photoinduced electron transfer (PET). As the collision causes a faster return to the ground state, changes in the FLTs are expected with the introduction of metals. This change ( $\tau_0/\tau$ ) is proportional to that of the fluorescence intensity ( $F_0/F$ ), and both are linear functions of the concentration of the metal quencher  $[Q]$  and the Stern-Volmer quenching constant ( $K$ ).  $K$  is itself dependent on the bimolecular quenching constant  $k_q$  and the initial NP lifetime ( $\tau_0$ ).<sup>53, 54</sup> These relationships can be summarized by Equation (3):

$$\frac{F_0}{F} = \frac{\tau_0}{\tau} = 1 + K[Q] = 1 + k_q\tau_0[Q] \quad (3)$$

Therefore, dynamic quenching is first evidenced by a change in the FLT, which is not present in static quenching. Moreover, as dynamic quenching acts only upon excited-state systems, that is systems that have already absorbed incident light, the absorbance spectrum of a system does not change with increasing concentration of the metal quencher.<sup>53, 54</sup> Finally, as in static quenching, there exists a temperature dependence in dynamic quenching.<sup>53, 54</sup> This relationship, described in Equation (4), describes the dependence of  $k_q$  on the quenching efficiency ( $f_q$ ), and the diffusion-controlled bimolecular rate constant ( $k_0$ ).<sup>53</sup>

$$k_q = f_q k_0 \quad (4)$$

As described, the quenching is dependent on diffusion, meaning that as the temperature of the system increases, and the particles and metals move faster within the sample, there are more

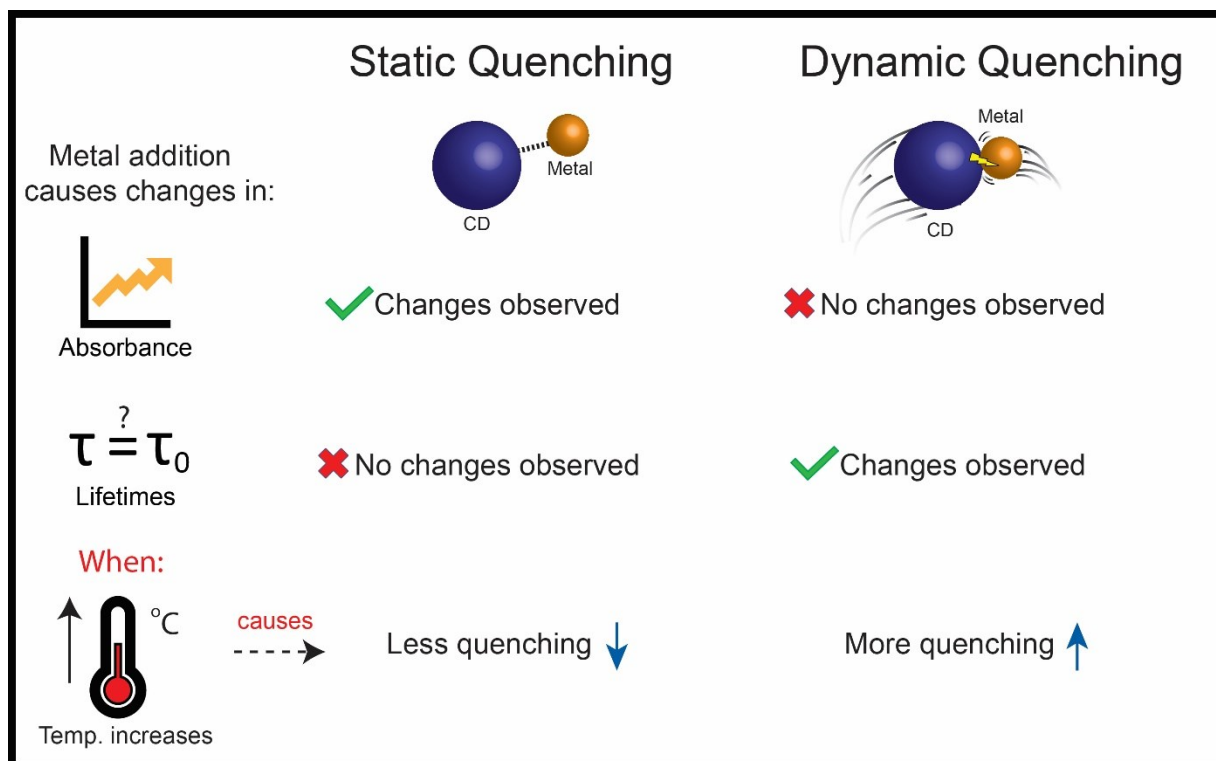


**Figure 8:** Graphical summary of the differences between static and dynamic quenching.

frequent collisions, causing an increase in dynamic quenching.<sup>53, 54</sup> The main differences between static and dynamic quenching in observed NP properties, following interactions with metal ions, are illustrated in Figure 8.

Both these quenching mechanisms result in a decrease of the fluorescence intensity with increasing metal quencher concentration. As such, it is possible to quantitate the metal concentration in a system based on changes in fluorescence. One example of this is from the work of Elmizadeh *et. al.* who synthesized CdTe QDs for the detection of chromium cations.<sup>55</sup> The surface of the QD was modified using a hydrophilic ligand, Bis(2-methylbenzaldehyde)butane-2,3-dihydrazone (TDSB), to allow the nanoparticle to be dispersed in water. A TEM image of these QDs is shown in Figure 9A. Quenching experiments were carried out in phosphate buffered saline

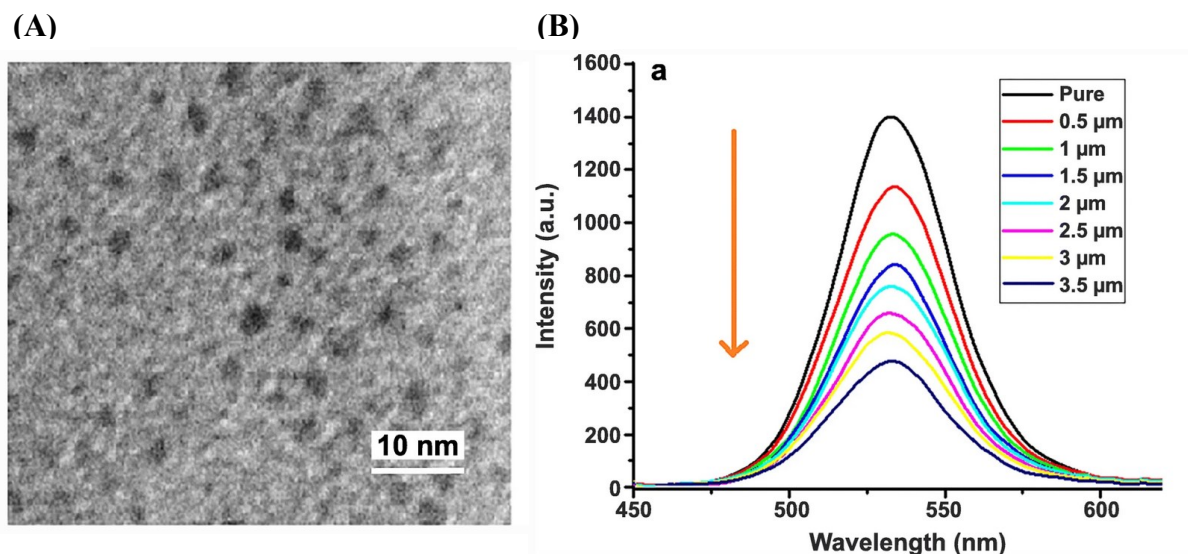


**Figure 9:** (A) TEM image of the CdTe QDs (B) Plot showing quenching of fluorescence with the addition of increasing concentrations of Cr<sup>3+</sup>. Image source: Elmizadeh *et. al.*<sup>55</sup>

(PBS) buffer with increasing concentrations of metal ions. The fluorescence intensity was measured following the addition of metal ions (Figure 9B) and it was found that this NP showed sensitivity only to Cr<sup>3+</sup> with an LOD of  $20 \times 10^{-9}$  M (3 ppb); the quenching mechanism was however not investigated.<sup>55</sup> While QD synthesis is mature and well studied, QDs suffer from a great number of drawbacks. Firstly, they often require extensive post-synthesis modification with a hydrophilic ligand to render them water-dispersible, an extra step not required for inherently hydrophilic NPs.<sup>51, 55</sup> Moreover, surface ligands, such as the ones reported in the work of Elmizadeh *et. al.*, may become unstable in acidic environments<sup>55</sup>, thus requiring a pH correction before any metal sensing experiments can be performed. QDs are also comprised of toxic metals, which could potentially find their way into the environment.<sup>11, 39, 56</sup> Finally, QDs are susceptible to what is called photoblinking, a phenomenon where the particle presents intermittent fluorescence emission. This is due to competing emissive and non-emissive states in the particle, which cause alternating radiative and non-radiative relaxation perceived as a blinking fluorescence.<sup>51</sup>

Zhang *et. al.* provide an example using PDs synthesized with branched polyethyleneimine and peryleneimide derivatives in dimethylacetamide.<sup>57</sup> As expected, the fluorescence of this system decreased with increasing metal concentration added. In this case, it was found that the system was especially sensitive to Fe<sup>3+</sup> with a calculated LOD of 20 x10<sup>-9</sup> M (5 ppb). The authors speculated that a special coordination interaction took place between the Fe<sup>3+</sup> ions and the amino and hydroxy surface functional groups on the PD. This coordination enabled aggregation of the particles which resulted in quenching of the fluorescence through an energy transfer, a type of dynamic quenching, between the excited state PD and the metal cation.<sup>57</sup> However, as with QDs, many of these PDs are hydrophobic and require post-synthesis modification with a hydrophilic surface ligand. Modifications of this kind can also impact the fluorescence quantum yield (QY) and stability of these NPs.<sup>58, 59</sup> The QY is a measure of the efficiency with which a NP converts an absorbed photon into radiative emission (release of a photon).<sup>53</sup> PDs also suffer from very broad fluorescence spectra, in comparison to other NPs such as QDs, which limits multiplexing applications. Their large batch-to-batch variability also results in large differences in particle size and optical properties.<sup>59</sup> Moreover, tuning PD fluorescence can only be realized through doping with organic dyes, which are prone to photobleaching.<sup>58</sup> Finally, PDs are found to have a shorter shelf-life and lower colloidal stability when compared to other NPs.<sup>59</sup>

#### ***1.4. Carbon Dots***

In light of the above, there has been significant interest in CDs, one of the most promising members of the carbon allotrope family. Discovered in 2004 by the Scrivens research group, as a by-product of the electrophoretic purification process of single-walled carbon nanotubes, these dots have continued to gain popularity due to their distinct properties.<sup>43, 52, 60-62</sup> CDs are spherical in shape ranging in diameter between 1 and 10 nm with a predominantly amorphous structure.<sup>43,</sup>

<sup>61-64</sup> They are mainly composed of carbon, hydrogen and oxygen, but also contain a certain percentage of nitrogen and sulfur, depending on the precursors and reaction conditions used.<sup>61, 64</sup> With regards to their synthesis, CDs can be produced using any carbon-containing compound. They can be synthesized using precursors ranging from simple molecules such as citric acid<sup>64, 65</sup>, amino acids<sup>66, 67</sup>, and sugars<sup>68, 69</sup> to more heterogeneous compounds like honey<sup>70, 71</sup>, orange juice<sup>71, 72</sup>, or milk<sup>71, 73, 74</sup>. However, due to the complex composition of heterogeneous precursors, the resultant CDs can show a wide variability in properties and chemical composition. As such, when aiming to produce CDs with uniform properties and a high batch-to-batch reproducibility, it is best to work with simple, homogeneous molecules as precursors.<sup>71</sup> These precursors also dictate which functional groups will be present on the CD surface. This is particularly important as the hydrophilic functional groups (e.g. carboxylic acids, amines, hydroxyls) present on the CD surface allow for dispersibility in water.<sup>43, 61-64</sup> These functional groups can likewise have a great impact on the charge, reactivity, and sensing capabilities of these NPs. As such, it is also noteworthy that the CD surface chemistry is quite versatile and can be easily modified to alter its properties or endow specific functionality to the surface.<sup>64</sup> In addition to these desirable and versatile properties, CDs have reportedly good biocompatibility as well as low chemical and cytotoxicities.<sup>43, 61-63, 66</sup> This renders them ideal candidates for *in vitro* and *in vivo* applications such as bioimaging and diagnostics.<sup>62, 63, 66, 71, 75</sup> However, it should be noted that no long-term studies on the toxicity of CDs have been conducted to date, as such these claims are based on a limited number of short-term studies.<sup>76, 77</sup> CDs are also reported to have a long shelf-life and good stability over a wide range of pHs.<sup>63, 75</sup>

What is most interesting about these dots are their optical properties, which have opened up investigation for their integration in several fields including imaging, sensing and catalysis.<sup>43, 61-63</sup>

Firstly, their fluorescence, which has a high QY, can be tuned to emit in all regions of the visible and near-infrared (NIR) spectrum through modification of the synthesis precursors and conditions.<sup>52, 61, 62</sup> Their high QYs can be attributed to the efficient passivation of surface traps on the particle by electron-donating species, such as nitrogen and sulfur groups. By filling surface traps with electrons donated by passivating agents, the probability of an excited electrons taking a non-radiative relaxation pathway is greatly reduced. As such, the QY of the CD is increased.<sup>61, 64, 78</sup> Surface passivation also plays an important role in dictating the optical properties of CDs. Unpassivated dots often display low fluorescence QYs that arise from a multitude of electronic states. A lack of passivation is characterized by excitation dependent fluorescence signatures, which exhibit blue- or red-shifted fluorescence as a function of the excitation wavelength. Passivation leads to a decreased number of these emissive states resulting in efficient and excitation independent states.<sup>61, 79, 80</sup> Finally, it is noteworthy to mention that CD fluorescence is generally photostable, showing low photobleaching and photoblinking.<sup>43, 61-64</sup>

The mechanism through which the fluorescence in CDs occurs is, to this day, a highly debated topic in the literature. Several mechanisms have been proposed, but three mechanisms stand out: quantum confinement, core states and surface/molecular states. The first theory, quantum confinement, occurs when the NP size approaches the De Broglie wavelength, a function related to the probability density of finding a particle at a specific point in space, which produces quantum effects not observed in the bulk material. Thus, the electrons behave like a particle in a box where the size of the box (i.e. the diameter of the CD) determines the size of the NP's band gap, which in turn alters the wavelength of emitted photons.<sup>52, 81, 82</sup> In this case, as the size of the particle increases, the bandgap size shrinks, meaning less energy is required to cross the bandgap, causing

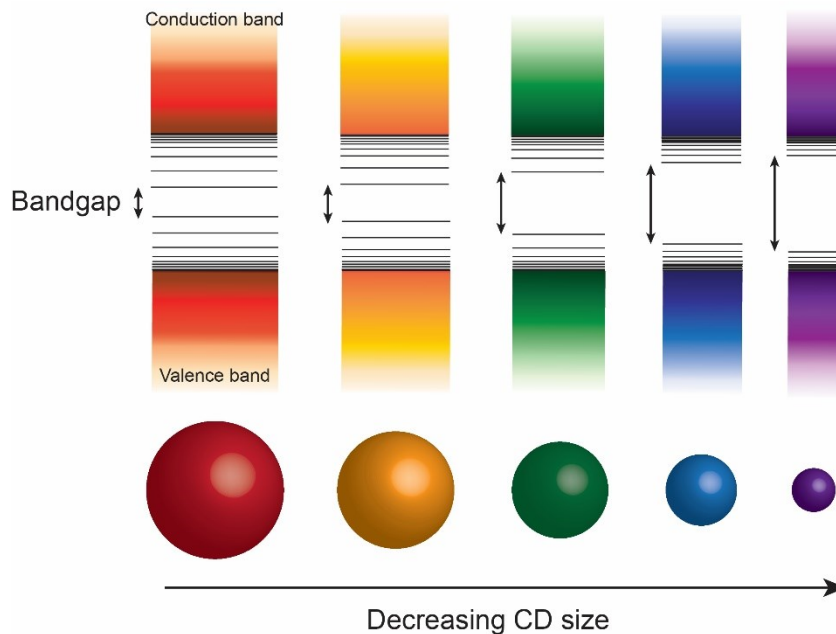


**Figure 10:** Graphical illustration of the increasing bandgap with decreasing CD size in the quantum confinement effect.

a red-shift in the NP's emission. Conversely, smaller particles will have larger bandgaps and a more blue-shifted emission.<sup>52, 82</sup> The relationship between CD size and emission wavelength is illustrated in Figure 10.

The second mechanism revolves around core states and explains that the fluorescence of the CDs stems from the excitation and subsequent radiative relaxation of the complex aromatic core.<sup>52, 66, 75</sup> This is believed to be the reason for the intrinsic blue fluorescence of most CDs, which is the most photostable type of CD fluorescence and least likely to be affected by the matrix environment.<sup>52, 66, 75, 83, 84</sup> Similarly, the third mechanism, surface/molecular states, stipulates that the fluorescence actually arises from the excitation and radiative relaxation of conjugated surface networks, where surface functional groups are responsible for altering the fluorescence wavelengths.<sup>52, 66, 75, 83, 85</sup> These networks may be composed of crosslinked fluorophores bound to the surface of the CDs, hence the name “molecular states”.<sup>52, 66, 75</sup> Finally, many reports describe

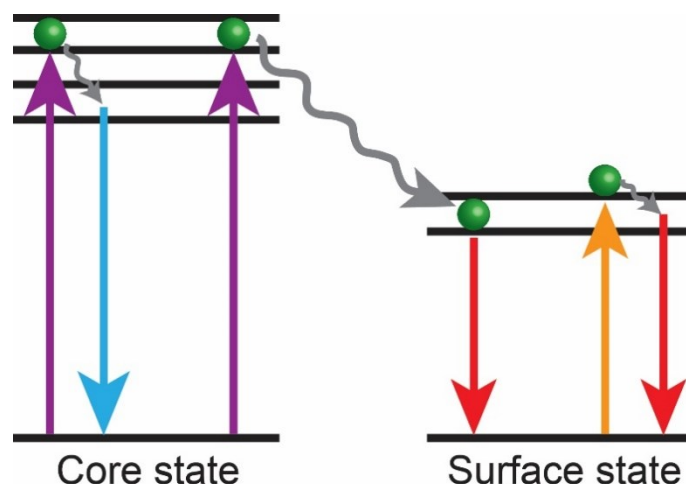


**Figure 11:** Graphical illustration of the core and surface states fluorescence mechanism, showing the possibility of energy transfers between the two states.

the possibility of an energy transfer from the aromatic core to the surface conjugated network. As such, fluorescence can result from both core and surface states in CDs (See Figure 11).<sup>66, 75, 83</sup> This claim is endorsed by reports of CDs exhibiting simultaneous fluorescence at more than one wavelength, where one fluorescence emission originates from the core and the other is ascribed to surface states.<sup>66, 75, 86</sup> Moreover, it has been shown that surface-state fluorescence is more sensitive to changes in the environment leaving the core fluorescence unaffected, further supporting this claim.<sup>66, 75</sup>

### ***1.5. Statement of the Problem***

With such unique and important properties, it is not surprising that CDs have already come under investigation for use in metal sensing applications. CDs have shown great sensitivity in sensing metals such as  $\text{Hg}^{2+}$ <sup>87-92</sup>,  $\text{Fe}^{3+}$ <sup>93, 94</sup> and  $\text{Pb}^{2+}$ <sup>95, 96</sup> among many others.<sup>61, 71, 79, 80</sup> Although CDs have been extensively studied in this area, there remains a lack of understanding when it comes to the fundamental chemistry and mechanism of the metal-CD interactions. For instance, in many publications, the quenching mechanism is completely overlooked or only briefly discussed without offering compelling evidence. Previous publications on metal sensing CDs have suggested

mechanisms related to unspecified non-radiative electron transfers from the CD to the metal cation, with some studies suggesting coordination of the metal to certain functional groups on the CD surface, such as hydroxyl groups. Yet, many of these claims remain unsupported by convincing evidence, and, in some cases, the suggested quenching mechanism can go against the data provided.<sup>91, 92, 94, 95</sup>

Clearly, a lack of understanding in this field persists and it is essential that the fundamental metal-CD interaction and quenching mechanisms be thoroughly investigated. This understanding can also provide additional insights into the reason for the observed selectivity of certain CDs. A better understanding of how these sensing systems work can also provide researchers with the tools necessary to design more sensitive and selective metal detecting NPs that can translate to concrete applications.

### ***1.6. Project Objectives***

Considering the knowledge gaps still present in the field of CD metal sensing, this work focuses on shedding light on the fundamentals of metal-CD interactions.

The first step was the synthesis of CDs using various precursors through a one-pot microwave synthesis reaction. Here, the purification procedure was extensively studied to determine the impact of purification on the observed physico-chemical and optical properties of the CD, as it is believed that improper purification can impart heterogeneous properties. With greater knowledge about the purification process, the construction of purification protocols tailored to each CD system could be achieved, thus ensuring the uniformity of their inherent properties and sensing capabilities. Once completed, extensive characterization was carried out using transmission electron microscopy (TEM) to determine the size, size distribution, and morphology

of the CDs. X-ray diffraction (XRD) was used to assess the crystallinity and phase of the NPs. Subsequently, Fourier-transform infrared (FTIR) and X-ray photoelectron spectroscopies (XPS) were used for the study of the surface and core composition of the CDs, providing insights into the functional groups present on the surface. Steady-state fluorescence and UV-Vis spectroscopy were used to characterize the optical properties of these CDs. Finally, the decay time(s) of the observed fluorescence signature(s) were analyzed in order to shed light on the optical centers present in the dots.

The sensing capabilities of the CDs were evaluated through a series of experiments, where several testing parameters were optimized including the type of CD used, metal cation selection, and experimental concentrations, amongst others. Once optimized, the quenching assays allowed for the determination of the effect of cationic size, charge, oxidation state and number of valence electrons. These quenching assays also helped ascertain whether there is selectivity or particular sensitivity to a specific cation. The LOD and linear range of the detection using CDs were determined for each metal species. Finally, the quenching mechanism for each metal cation was investigated by observing changes in the absorbance spectra, the fluorescence decay and through temperature-dependent analyses. Using this knowledge as well as the results of the quenching experiments, we present a theory that not only explains the quenching mechanism, but also describes the surface interactions occurring between the metal cations and the CDs.

## **Chapter 2. Materials and Methods**

### ***2.1. Chemicals and Reagents***

Citric acid, diethylenetriamine (DT3), ethylenediamine (ED2), glutathione, copper chloride (II), iron (III) chloride, cobalt (II) chloride hexahydrate, nickel (II) chloride, gadolinium (III) chloride hexahydrate, dysprosium (III) chloride hexahydrate, zinc (II) chloride, lead (II) chloride, mercury (II) chloride, PBS buffer and ethanol were purchased from Sigma Aldrich. Formamide, acetone and chromium (III) chloride were purchased from Fisher Scientific. LC-MS water was purchased from Fisher Scientific, while Milli-Q water was produced in-house. All reagents used were of analytical grade and did not necessitate additional purification prior to use.

### ***2.2. Synthesis of CDs***

A number of different precursors were investigated for the preparation of the CDs to allow for the controlled decoration of the CD surface with a variety of functional groups. This permitted the use and exploitation of the differences in physico-chemical properties of these CDs. Metal-sensing capabilities of these unique CDs were also determined and compared.

#### **2.2.1. Synthesis of Citric Acid and Ethylenediamine CDs**

CDs were prepared using 10 mL of 0.5 M citric acid solution and 455  $\mu$ L ethylenediamine (1:0.75 molar ratio). The mixture was placed into a 35 mL microwave vial and heated with constant stirring for 10 minutes at 210°C in a CEM Discover SP microwave reactor. The dark brown product was dialyzed using a 1 kDa molecular weight cut-off (MWCO) cellulose-ester membrane (Spectra/Por® 6 RC – Spectrum Laboratories) in 1 L MilliQ water. The dialysis water was changed twice daily for 4 days. The resultant light-brown solution was filtered through a 0.22  $\mu$ m nylon filter to remove large agglomerates. The solution was then placed in an 80°C oven to concentrate

it down. Finally, the ethylenediamine CDs (ED2-CDs) were dried to a powder in an 80°C oven and later re-dispersed in water at a known concentration.

### 2.2.2. Synthesis of Citric Acid and Diethylenetriamine CDs

These CDs were produced at two different concentrations of the DT3 precursor. In two separate microwave vials, a solution of 500 mM citric acid and 375 mM DT3 (375DT3 CDs), and a solution of 500 mM citric acid and 750 mM DT3 (750DT3 CDs) were microwaved for 10 minutes at 180 °C with vigorous stirring in a CEM Discover SP microwave reactor. To determine the effect of purification on the CD properties, an aliquot of this crude product was collected for analysis. The remainder was first filtered through a 0.22 µm nylon filter to remove large aggregates. Next, the samples were dialyzed against 1-L of Milli-Q water using 1 kDa MWCO cellulose-ester dialysis membrane (Spectra/Por® 6 RC – Spectrum Laboratories). This step was repeated 5 times

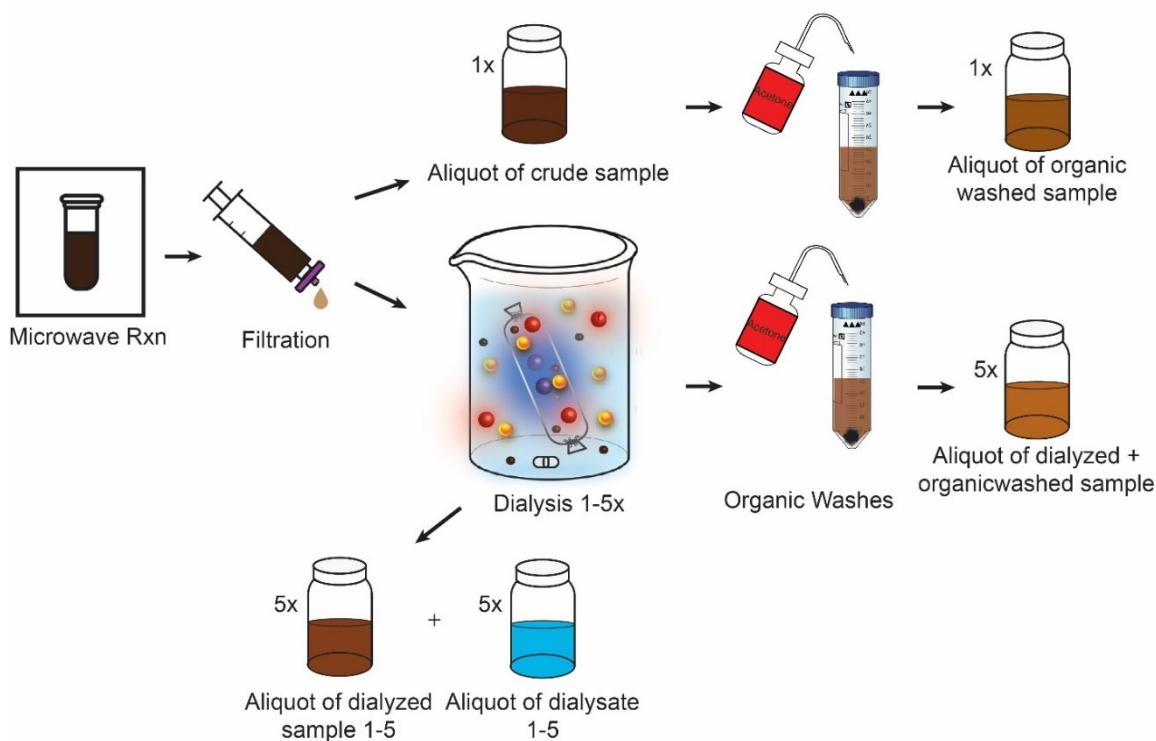


**Figure 12:** Graphical representation of the purification process of DT3-CDs showing all sample aliquots being kept for analysis and the purification methods they were subjected to.

over a period of 5 days, with an aliquot collected after each step. The 1-L dialysate, containing all ejected impurities, was also collected at each step and was concentrated from 1 L to 40 mL by drying in an oven at 80 °C. Each dialyzed sample was further purified by washing twice with acetone. After each wash, the sample was subsequently centrifuged at room temperature at 10 000  $x$  g for 10 minutes and the supernatant was discarded. This process is depicted in Figure 12, showing the purification undergone by each sample collected. The final precipitate was then dried in an 80 °C oven to then be dispersed in water at the desired concentration.

### **2.2.3. Synthesis of Formamide and Glutathione CDs**

Formamide and glutathione-based CDs (FG-CDs) were synthesized using 0.334g of glutathione dissolved in 10 mL of formamide to form a 0.1 M solution. The solution was sonicated until it was completely clear and transferred to a 35 mL microwave vial. The vial was then heated for 5 minutes at 180°C in a CEM Discover SP microwave reactor. The resulting dark green solution was dialyzed using a 3.5-5.0 kDa MWCO cellulose-ester membrane (Spectra/Por® 6 RC – Spectrum Laboratories). The solution was then concentrated down in an 80°C oven before being passed through a 0.22  $\mu$ m nylon-filter to remove large aggregates within the solution. Next, the sample was subjected to an organic acetone wash, followed by 2 organic ethanol washes and a final acetone wash with centrifugation at 10 000  $x$ g for 5 minutes following each wash. Finally, the CDs were dried at 80°C before being re-dispersed in water at a known concentration.

### **2.3 Characterization and Quenching Evaluation Techniques**

The synthesized CDs were characterized using Fourier transform infrared spectroscopy–attenuated total reflectance (FTIR-ATR), TEM, XPS, XRD, Zeta Potential, absorbance and fluorescence spectroscopies, and FLT measurements. The last three techniques were also used during quenching assays to assess the metal sensing capabilities of CDs.

### **2.3.1 FTIR-ATR**

FTIR-ATR spectra were acquired using a Thermo Scientific Nicolet iS5 equipped with iD5 ATR accessory. Dried powder CD samples were used as is, while 1  $\mu\text{L}$  of the aqueous CD dispersions was allowed to evaporate to dryness, at room temperature, for 15 min prior to spectrum acquisition. A total of 64 scans, at a resolution of  $0.4\text{ cm}^{-1}$ , were obtained on a laminate-diamond crystal window, using the following instrument settings: a DTGS KBr detector set to a gain of 1, an optical velocity of  $0.4747\text{ cm/s}$  and an aperture of 100. The Thermo Scientific Nicolet Omnic 9 software was used for all data processing.

### **2.3.2. Transmission Electron Microscopy (TEM)**

Grids were prepared by pipetting 2  $\mu\text{L}$  of a 5.0 mg/mL CD dispersion onto a 200mesh Formvar/carbon coated copper grid (3 mm in diameter) followed by evaporation of the solvent. The TEM images were collected using a Jeol JEM-2100F microscope operating at 100 kV. The Fiji imaging software<sup>97</sup> was used for image processing and to determine the size of the CDs.

### **2.3.3. X-ray Photoelectron Spectroscopy (XPS)**

XPS spectra were obtained using a Thermo Scientific K-Alpha X-ray Photoelectron Spectrometer equipped with an Al K alpha source gun in standard lens mode, a CAE analyser mode using 50.0 eV pass energy with a 0.100 eV energy step size and a 400 mm spot size. Each analysis was carried out in triplicates using 10 runs for each scan. The averages for both the survey and high-resolution scans were plotted. The Thermo Scientific Avantage Data System software was used for data collection and analysis.

### **2.3.4. X-Ray Diffraction (XRD)**

XRD patterns were evaluated on a Bruker D2 Phaser diffractometer using Cu  $K\alpha$  radiation ( $\lambda = 0.15405\text{ nm}$ ). Analysis of the dried CD powder was carried out over the range of  $10\text{--}80^\circ 2\theta$

with a step size of 0.02° and a 0.5 s count time. Data analysis was conducted using the MDI Jade software.

### **2.3.5. Zeta Potential**

The overall zeta potentials (surface charges) were measured using a Malvern Zetasizer Nano-S. All experiments were carried out using a disposable folded capillary cell (Malvern). For each sample, experiments were repeated three times at 25 °C using the average of 13-15 runs each. The concentration of the samples was ~0.35 µg/mL in LC-MS water. Measurements were conducted using approximately 0.7 mL of the solution. Data were analyzed using the software supplied with the instrument.

### **2.3.6. Absorbance Spectroscopy**

UV-Vis absorbance spectra of the aqueous CD dispersions were collected using a Cary 5000 Series UV-Vis-NIR Spectrophotometer from Agilent Technologies. The scans were acquired over a range of 200 – 800 nm in a 1-cm quartz cuvette at a speed of 600 nm/s, 1 nm resolution and a 2-nm bandwidth. Data collection and processing were performed using the Agilent Cary Eclipse Scan software package.

### **2.3.7. Fluorescence Spectroscopy**

The fluorescence spectra of the aqueous CD dispersions were recorded using a Cary Eclipse Fluorescence Spectrophotometer from Agilent Technologies. To minimize potential inner-filter effects, sample concentrations were adjusted to an absorbance value between 0.1 – 0.4 A.U. prior to the collection of the fluorescence spectra.<sup>98, 99</sup> Fluorescence spectra were acquired in a 1-cm quartz cuvette, using an excitation slit width of 2.5 nm, an emission slit width of 5 nm with a PMT voltage of 600 V. Data collection and processing were performed using the Agilent Cary Eclipse application software.

### **2.3.8. Quantum Yield Determination**

A FLS920 Fluorescence Spectrometer (Edinburgh Instruments) equipped with an integrating sphere was used to determine QY values for the CDs. Duplicate spectra were obtained in a 1-cm pathlength quartz cuvette, from 320 to 700 nm, using  $\lambda_{\text{ex}} = 350$  nm. Instrument parameters were set as follows: excitation and emission slit widths set to 15 nm and 5 nm, respectively, and a 0.2 s dwell time. Water was used as the reference solvent for the determination of scattering. Data acquisition and processing were performed using the F900 software supplied by the instrument manufacturer.

### **2.3.9. Fluorescence Lifetimes**

The EasyLife X fluorescence lifetime system (Optical Building Blocks Corporation) was used for acquisition of the CD's FLTs. Measurements were conducted in a 1 cm quartz fluorescence cuvette, using a 368 nm pulsed picosecond LED excitation source. The collection parameters were as follows: an emission slit width of 1.5 mm, 500 channels, 0.25 s integration time and an average of 3 readings for each sample. A bi-exponential decay was determined with a random collection mode to account for any potential photobleaching. Moreover, logarithmic collection steps were used to obtain more data points at the time of the pulse and at the beginning of the decay. The OBB EasyLife X software was used to collect and analyze the data.

## **2.4. Quenching Assays**

All solutions were prepared immediately before all quenching assays. Table 1 summarizes the mass of metal salts used to produce 5 mL of a concentrated 0.1 M metal solution in Milli-Q (pre-optimization) and LC-MS (post-optimization) water. A serial dilution was then performed to produce 0.01, 0.001, 0.0001 and 0.00001 M metal solutions, which were used for the quenching

**Table 1:** Tables of masses used to prepare metal salt solutions used in the quenching assays.

<b>Metal Salt</b>	<b>Molecular Weight</b>	<b>Mass</b>	<b>Concentration</b>
PbCl <sub>2</sub>	278.10 g/mol	0.139 g/5 mL	0.1 M
FeCl <sub>3</sub>	162.20 g/mol	0.081 g/5 mL	0.1 M
ZnCl <sub>2</sub>	136.28 g/mol	0.068 g/5 mL	0.1 M
HgCl <sub>2</sub>	271.50 g/mol	0.135 g/5 mL	0.1 M
NiCl <sub>2</sub>	129.60 g/mol	0.065 g/5 mL	0.1 M
CrCl <sub>3</sub>	158.36 g/mol	0.079 g/5 mL	0.1 M
GdCl <sub>3</sub> *6H <sub>2</sub> O	371.70 g/mol	0.185 g/5 mL	0.1 M
DyCl <sub>3</sub> *6H <sub>2</sub> O	376.95 g/mol	0.188 g/5 mL	0.1 M
CuCl <sub>2</sub>	134.45 g/mol	0.067 g/5 mL	0.1 M
CoCl <sub>2</sub> *6H <sub>2</sub> O	237.93 g/mol	0.118 g/5 mL	0.1 M

assays. Concentrated CD dispersions of known concentrations were sonicated and used to produce the following colloidal dispersions for quenching and optimization experiments: 3 mL of 1-10  $\mu\text{g/mL}$  ED2-CDs, 3 mL of 0.2-1.5  $\mu\text{g/mL}$  DT3-CDs, and 8 mL of 21-35  $\mu\text{g/mL}$  FG-CDs. UV-Vis and Fluorescence measurements of each CD sample were then taken at increasing concentrations of metal cation. Prior to spectroscopic measurements, the samples were stirred using a magnetic stirrer for approximately 20 seconds following the addition of a known volume of metal solution. These known volumes of metal solutions, which were used exclusively for the FG-CD quenching experiments after optimization, are displayed in Table 2.

**Table 2:** Volumes of metal solution added to 8 mL CD samples during post-optimization quenching assays.

<b>Sample (nM)</b>	<b>Metal Concentration (M)</b>	<b>Volume Metal Added (uL)</b>	<b>Sample Concentration (nM)</b>
<b>0</b>	0	0	0
<b>50</b>	0.0001	4	49.98
<b>100</b>	0.0001	4	99.93
<b>250</b>	0.0001	12.1	250.80
<b>400</b>	0.0001	12	400.20
<b>550</b>	0.0001	12.1	550.62
<b>700</b>	0.0001	12	699.60
<b>850</b>	0.0001	12.1	849.54
<b>1000</b>	0.0001	12.2	1000.52

## Chapter 3. The Role of Purification in Carbon Dot Synthesis

### 3.1. The Challenges Encountered in the Literature

This work began with a survey of the literature to seek out CDs with potential metal sensing capabilities. During a thorough search, many conflicting results were uncovered with respect to the reported sensing capabilities of CDs. Often, broad detection ranges were reported not only between different carbon dot systems but quite often for the same type of carbon dot prepared using the same precursors and synthesis technique. In one example, citric acid and ethylenediamine CDs were investigated for the detection of mercury (II) ions in solution and reported LODs ranged from 0.5 to 500 nM, showing that even the same CDs can have a 1000-fold difference in the detection of the same metal cation.<sup>87-90, 100</sup> When replicating these studies, our own lab achieved a LOD of 150 nM for mercury (II) ions. As such, it was difficult to ascertain the true sensing capabilities of these CDs due to inconsistencies in their reported physico-chemical, optical and sensing properties.

Such discrepancies were repeatedly observed when testing other CD systems for metal sensing purposes. Looking more closely at the literature, we uncovered more conflicting reports of a larger selection of CD properties. Reported synthesis yields ranged from 6% to 80%,<sup>101, 102</sup> while fluorescence QYs varied from 0.6% to 94.5%.<sup>64, 103-107</sup> Even in cases where CDs were synthesized using the same precursors, inconsistent QYs were reported, which highlighted a lack of reproducibility.<sup>64, 104, 108</sup> While attempting to pinpoint the root of this problem, it was found that these studies tend to show very slight differences, if any, in the reported synthesis methods. However, purification procedures, which were frequently underreported or completely overlooked, varied extensively between published studies. We hypothesized that the inconsistencies in the reported CD properties were ascribed to the highly variable and often inefficient purification methods used, which can impart heterogeneous physical and optical properties to the CDs.<sup>52, 64, 109,</sup>

<sup>110</sup> Therefore, it was imperative to further investigate the role of purification on the observed properties of CDs prior to embarking on a fundamental and mechanistic study of metal sensing.

This path first required us to determine the efficiency of various purification techniques. For this purpose, we meticulously observed changes in the physico-chemical and optical properties of two CD systems synthesized using citric acid and diethylenetriamine throughout an extensive purification protocol that we designed to achieve “optimal” CD purity. This protocol included filtering through a 0.22  $\mu\text{m}$  nylon filter to remove large aggregates within the sample, dialysis using a 1 kDa MWCO cellulose-ester membrane with a pore size below 1 nm<sup>111</sup> to remove small water-soluble and membrane-permeable impurities, as well as organic washing with acetone to remove any small impurities that could not be removed through dialysis. Changes in the physical properties of the CDs were probed throughout the purification procedure via FTIR to determine the surface chemical composition while differences in optical properties at each purification step were assessed through UV-Vis and fluorescence spectroscopies, as well as fluorescence QYs. As such, we attempted to demonstrate how a combination of optical and surface characterization techniques could together be used to tailor purification protocols for each unique CD system, and to accurately establish their purification endpoint.

The mechanism of formation of CDs is not yet entirely understood. However, recent research has focused on identifying the by-products and intermediates formed during the synthesis of the dots. These compounds are theorized to play an important role in the formation of CDs and endow them with specific physico-optical and chemical properties. Common theories stipulate that the first step in the CD synthesis process is the formation of various fluorophores and small molecules, which can then polymerize and aggregate before carbonizing to form the aromatic carbon core of the dots. Remaining fluorophores and small molecules can then attach themselves

to the aromatic core, interlinking to form a conjugated surface network resembling a shell around the carbon core.<sup>52, 112-114</sup> Several compounds have been identified as common fluorescent by-products of the CD synthesis, from citric acid and amines, including citrazinic acid and its derivatives as well as an array of fluorescent molecules and oligomers containing 5- and 6-membered rings.<sup>108, 115-118</sup> However, not all fluorophore by-products contribute to the formation of the dots and thus require removal from the final product. Here, the differences in the physical and optical properties of CDs were investigated as a function of the removal of such impurities to arrive at the inherent physico-optical properties of the CDs. The microwave synthesis of carbon dots, prepared from citric acid and diethylenetriamine, results in quasi spherical particles which are 2.5 nm in size with a distribution that spans 2-4 nm. The dots are amorphous in nature as evidenced by X-ray diffraction and the low contrast observed in the TEM images reported by Manioudakis *et al.*<sup>64</sup>

### ***3.2. Monitoring the CD Surface Throughout purification***

In this study, two citric-acid derived CD systems were synthesized using DT3 as the passivating agent, at concentrations of 375 or 750 mM. These carbon dots will henceforth be referred to as 375DT3 CDs and 750DT3 CDs, respectively. While having identical parent precursors would normally suggest similar physical, optical and chemical properties, this is in fact not the case. Indeed, differences in their respective optical and physical properties were examined at each stage of an extensive purification process involving multiple dialyses and organic washes. Both the 375DT3 and 750DT3 samples showcase important differences in their respective FT-IR spectra (Figure 13) and will be discussed separately prior to a comparative analysis. The 750DT3 CDs show FTIR spectra with features similar to those previously reported,<sup>64</sup> which include a broad band at  $\sim 1546\text{ cm}^{-1}$  corresponding to the unresolved C=C/N-H stretch/bend and a carbonyl stretch at

1650  $\text{cm}^{-1}$  ascribed to presence of amide functional moieties on the surface of the dots (Figure 13A, B and C). However, the 750DT3 CDs lack the carbonyl stretch ascribed to carboxylic acid groups at 1705  $\text{cm}^{-1}$ , suggesting that all of the citric acid was consumed during synthesis and the presence of excess amine passivating agent has likely resulted in amide bond formation. Upon comparison of the 750DT3 dialysate (Figure 13A) with the unwashed 750DT3 CDs (Figure 13B) and the organic washed 750DT3 CDs (Figure 13C), we observe a change in the ratio between the 1650  $\text{cm}^{-1}$  carbonyl amide stretch and the 1546  $\text{cm}^{-1}$  C=C/N-H stretch/bend with increasing purification steps. The dialysate (Figure 13A), being comprised of components expelled from the dialysis bag, naturally has the opposite trend in its spectra compared to those of the carbon dots that are retained in the membrane. As dialysis continues, the 1650  $\text{cm}^{-1}$  amide carbonyl stretch in the dialysate spectra decreases. Additionally, the intensity of the same amide stretches continually increase in both Figure 13B and C, which start to resemble the spectra of the CDs retained in the dialysis bag. This suggests that these stretches belong to the amide groups bound to the CD surface. Furthermore, adequate purification better reflects the actual CD surface composition by removing contributions from impurities expelled from the product, as can be seen by the increase in the small shoulder band at  $\sim 1700 \text{ cm}^{-1}$  ascribed to the carboxylic acid carbonyl stretch (Figure 13F). As such, the spectra of the dialysate and that of the CDs begin to appear more and more dissimilar. Even upon comparison of the two spectra in Figure 13B and C, and as more purification steps are added (i.e. with organic washing), the spectra become increasingly more resolved and begin to show a

lesser degree of change with each subsequent purification step. At this point, the spectra appear to accurately represent the CD surface and further purification does not indicate significant changes.

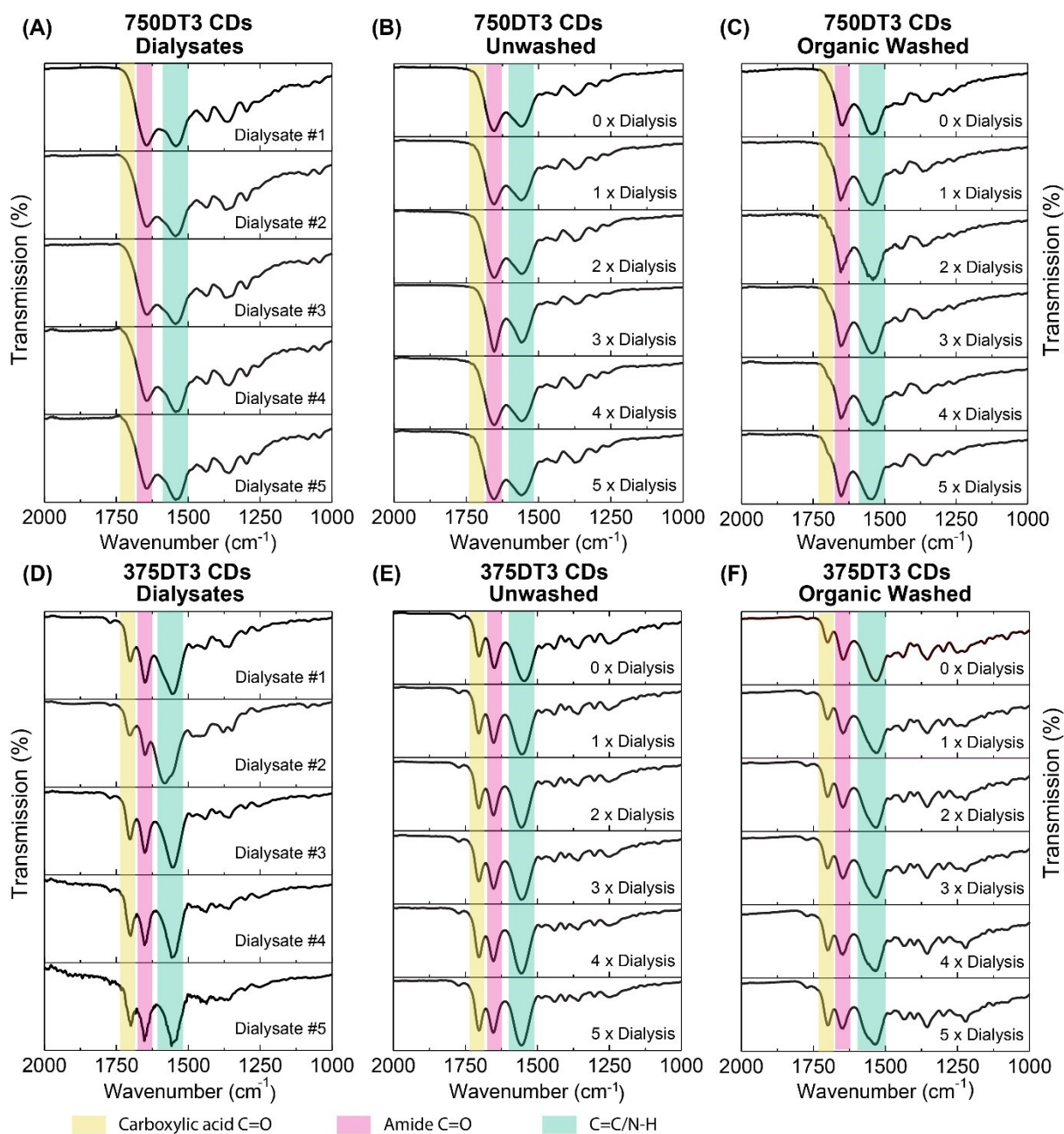


**Figure 13:** Demonstrating the effect of purification on the surface chemical moieties of CDs using FTIR. Stacked FTIR spectra are shown at different purification stages for 750DT3 (A-C) and 375DT3 CDs (D-F). The spectra showcase bands ascribed to amide, carboxylic acid carbonyls, as well as C=C/N-H groups. Following extensive purification, the spectra display a notable increase in the carboxylic acid carbonyl band ( $1705\text{ cm}^{-1}$ ) for both CD systems, in addition to a discernable increase in band resolution.

Similarly, the FTIR spectra for the 375DT3 CDs (Figure 13D, E and F) show the same previously discussed stretching vibrations. However, an additional peak is present at  $\sim 1700\text{ cm}^{-1}$  associated with the carboxylic acid carbonyl stretch, hinting at the presence of a lesser degree of amine passivation on the CD surface. This is ascribed to the lower concentration of the amine starting reagent relative to the citric acid precursor. Overall, as with the 750DT3 CDs, the resolution of the spectra improves with each additional purification step. With each subsequent dialysis, the spectra for both the unwashed and organic washed CDs show a continual decrease in the  $1650$  and  $1546\text{ cm}^{-1}$  stretches and bends associated with the amide carbonyl and C=C/N-H groups, respectively. Conversely, those same stretches are persistently stronger in the dialysate spectra, confirming that they are being expelled from the dialysis bag. The relative intensities in the dialysate spectra remain similar in all dialysate samples, however the overall intensity and signal-to-noise ratio decrease with further dialysis, suggesting that less impurities are being released from the dialysis bag.

### ***3.3. Optical Properties as a Function of Purification***

#### **3.3.1. Discerning Differences Through Absorbance Spectroscopy**

Steady-state UV/vis spectroscopy was used to evaluate the optical properties of all components throughout the CD purification process. Firstly, as expected, all the spectra exhibit 2 main absorbance peaks at approximately 240 and 350 nm commonly observed in amine-passivated CDs; these can be respectively attributed to the  $\pi \rightarrow \pi^*$  electronic transition of the aromatic  $\text{sp}^2$  core domain and the  $n \rightarrow \pi^*$  electronic transition of the C=O bond of amide moieties on the surface of the CDs.<sup>64, 86, 119, 120</sup> Both the core and shell of the dot are said to contribute to the observed optical properties. The CD sample and the impurities removed from this sample both contain some of the same fluorophores, thus it is unsurprising that both exhibit matching optical properties. These

absorbance spectra, with bands at 240 nm and 350 nm, show a striking resemblance to those of citrazinic acid and its derivatives, which have been specifically named as the most abundant by-products of CD synthesis from citric acid and polyamines.<sup>108, 121</sup> Figure 14 showcases overlaid absorbance spectra for 375DT3 and 750DT3 CDs at the different steps of the purification process. For the 750DT3 CDs, the spectra of both the unwashed and organic washed CDs are almost identical, save for a slight and consistent decrease in the overall intensity of all spectra after organic washing. This is expected, as every extra purification step will lead to a slight loss in product. In this case the addition of an organic wash step, after dialysis, prompts an almost identical loss in intensity for each separate sample. In contrast, the dialysates' spectra exhibit the starkest changes during the purification process, where we initially observe a broad, unresolved peak at 240 nm following the first dialysis step. This peak becomes successively more resolved with subsequent dialysis steps and is most likely due to the dialysate containing unreacted starting reagents, both incomplete and fully formed fluorophores, as well as fragmented CDs. As the sample undergoes dialysis, smaller, faster moving contaminants are removed first, followed by larger and diffusion-slow contaminants that are slowly excluded from the sample. This is shown by the increasing resolution of the peak, with the final spectrum being the one most closely resembling that of the purified CDs. The spectrum of Dialysate #3 shows a more intense 240 nm peak coupled with the appearance of a peak at ~ 280 nm. Recent studies have shown that, at high enough concentrations, citrazinic acid can form dimers and subsequently aggregate, thus causing drastic changes in its optical properties. Although these changes have yet to be extensively investigated, they often manifest themselves as shifts in the absorbance spectra resulting in absorbances in the 280 nm region.<sup>121, 122</sup> This 280 nm absorbance peak only appears in the third dialysate supporting the theory that these aggregates become larger and slower allowing them to be released at a later stage in the

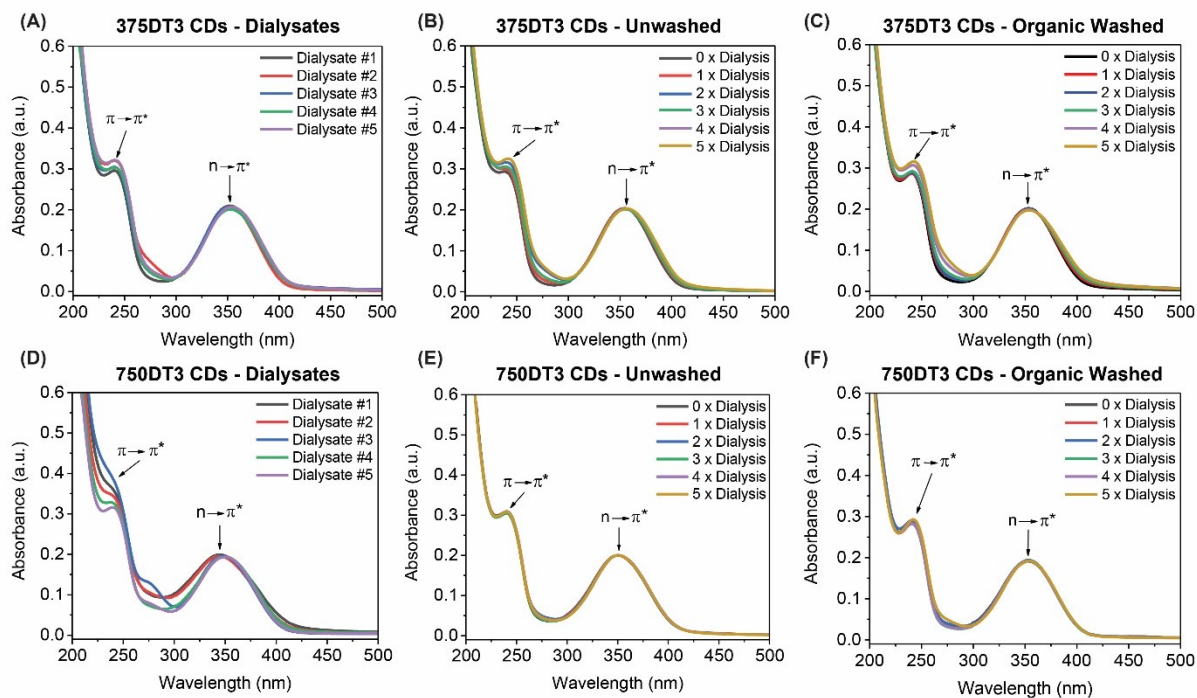


**Figure 14:** Effect of purification on the optical properties of CDs. Overlay of UV/Vis spectra at different purification stages for 375DT3 (A, B and C) and 750DT3 CDs (D, E and F), where absorbance has been adjusted to 0.2 a.u. at 350 nm for all samples. The spectra exhibit 2 main peaks at 240 and 350 nm, corresponding to the  $\pi \rightarrow \pi^*$  and  $n \rightarrow \pi^*$  transitions, respectively. The dialysates exhibit the starkest changes for both systems as impurities and smaller, incomplete fluorophores and CDs are successively dialysed out. This is reflected in the purified samples as sharper bands centered at 240 and 350 nm.

dialysis process relative to the smaller molecular impurities within the sample. Differences in precursor concentrations may also point to the reason as to why this is only observed in the 750DT3 CD dialysate, as a high enough concentration of citrazinic acid are present and required to observe such changes. It can be rationalized that purification allows certain fluorophores or particles with a high absorption at these wavelengths to become greater contributors in the absorption profile through their higher concentration at a specific stage in dialysis. This observation is further discussed (*vide infra*) when observing changes in the quantum yields. Interestingly, for the 375DT3 CDs, each successive measurement, at every purification step of both the organic washed and unwashed CDs, confers an increase in the absorbance band at 240 nm, suggesting an increase in the  $sp^2$  core domain content. This is likely due to the removal of unreacted starting reagents and

both small fluorophores and incompletely formed nanomaterials, resulting in a more significant contribution to the absorption spectrum from the fully formed CDs. That is, whereas before dialysis both the CDs and impurities contributed to the overall absorbance spectrum, as purification takes place, the impurities begin to contribute less and less to the overall absorption spectrum. This leaves the final absorption spectrum as the one most representative of the inherent absorption properties of the CDs. In the case of the dialysate, no such linear trend in the intensity is observed, as the intensity of the absorbance is dependent on the components being expelled at that stage of dialysis. As such, the intensity fluctuates with each successive dialysis step.

### **3.3.2. How Fluorescence Can Be Misleading**

Steady-state fluorescence spectroscopy was used to determine the photoluminescence properties of the CDs. These plots reveal that the profiles of all dispersions, throughout all stages of purification, exhibit essentially identical features, notably, excitation-independent fluorescence emission centered at  $\sim 445$  nm (Figure A1-A6), meaning that regardless of the excitation wavelength, the fluorescence maxima remain unchanged. However, slight variations in absolute intensities are observed and highlighted in Figure 15. The first involves the dialysate in Figure 15A-D where a weaker overall fluorescence intensity is observed for the 750DT3 dialysate than for the 375DT3 counterpart. Since an absorbance of 0.1 a.u. was used to normalize both sample concentrations and that the same precursors were used for synthesis in both samples, it can be deduced that the lower fluorescence intensities are a result of a difference in the abundance rather than the nature of the fluorescent by-products created during CD synthesis. Although the fluorescence intensity of the 375DT3 dialysate remains the same throughout the various dialysis steps, that of the 750DT3 dialysate increases significantly. This likely occurs since fewer small fluorophore by-products are produced during the 750DT3 CD synthesis. The first dialysate is likely

primarily composed of unreacted materials or non-fluorescent molecules. Once removed, larger components, such as incomplete CD-like entities and fluorophore aggregates are released into the dialysate, causing an increase in its fluorescence intensity. With respect to the CD samples in Figure 15E-F, dialysis does not seem to induce a change in the 375DT3 CD fluorescence contour plots. Moreover, no significant differences exist between any of the 375DT3 contour plots at any

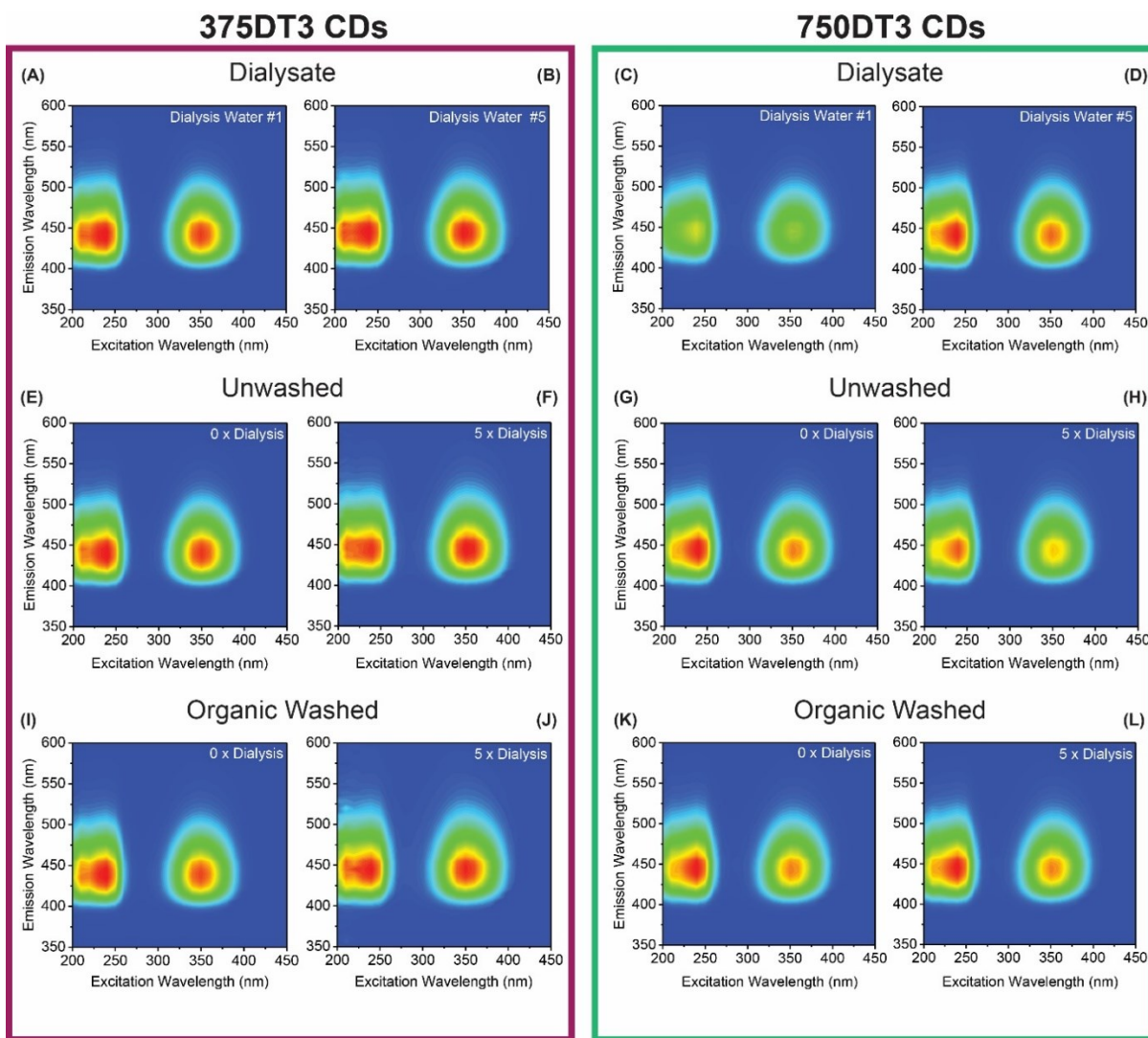


**Figure 15:** Selected fluorescence contour plots of samples normalized to 0.1 a.u. absorbance at 350 nm chosen to highlight spectral differences. The contour plots for the dialysate after the first and fifth dialysis step for the 375DT3 sample (A & B) and the 750DT3 sample (C & D). The contour plots both before and after a full series of dialysis without any organic washes for 375DT3 CDs (E & F) and 750DT3 CDs (G & H). The contour plots both before and after a full series of dialysis followed by organic washes for 375DT3 CDs (I & J) and 750DT3 CDs (K & L).

stage of the purification procedure. This could, once more, indicate the presence of a large number of impurities in the 375DT3 samples which require longer dialysis times to be completely removed. Conversely, the 750DT3 CD contour plots in Figure 15G-H evidence a minor decrease of the fluorescence intensity following dialysis, but no further changes are observed with organic washes in Figure 15K-L. These results are not surprising since it has previously been postulated that during the formation of CDs, fluorophores are generated first and upon further heating, subsequently undergo crosslinking, polymerization and carbonization to form a carbon core<sup>52, 112-114</sup> and functional groups on the surface that dictate the optical properties.

As such, monitoring changes in the optical properties of CDs throughout purification via fluorescence spectroscopy alone can lead to a false purification end-point. In this case, similar intensities and fluorescence peaks are observed for all samples at all stages of purification. By observing the fluorescence alone, it would be determined that purification need not be several steps long. Fluorescence spectroscopy reveals only the emission wavelength and intensity of a given sample at a given concentration. However, several components within the sample can emit at the same wavelength, especially considering that the precursors and intermediates formed are often incorporated into the CD product. As such, removal of one or more components may not affect the fluorescence spectrum. Herein lies the importance of expanding the study to include different optical properties in order to glean additional information about the CD optical properties and how these change as a function of purification.

### **3.3.3. Seeking the Answers in Fluorescence Quantum Yield Analysis**

We further examined how sample purification affected the optical properties of CDs, prior to and following every purification step, by monitoring the changes in fluorescence QYs. The QY value is a ratio of the efficiency with which a particle can convert absorbed photons into emitted

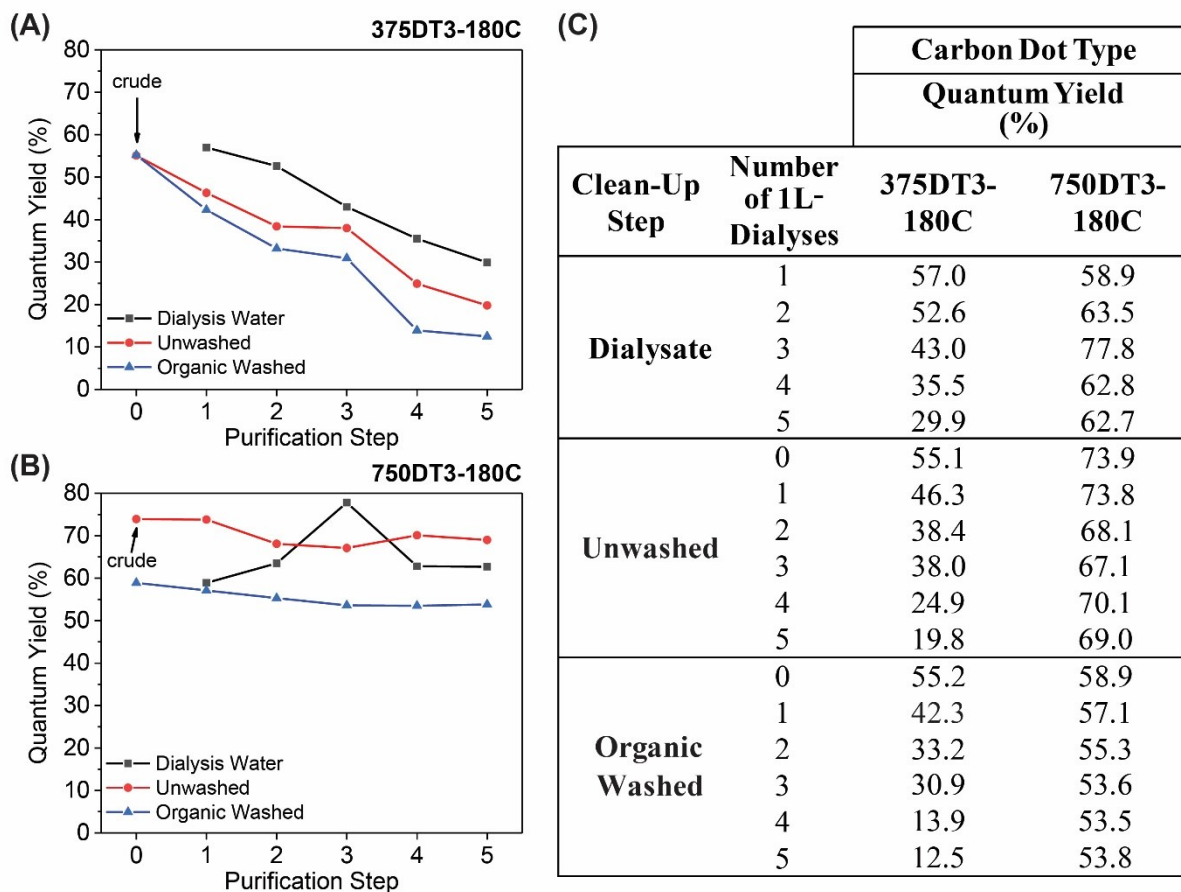
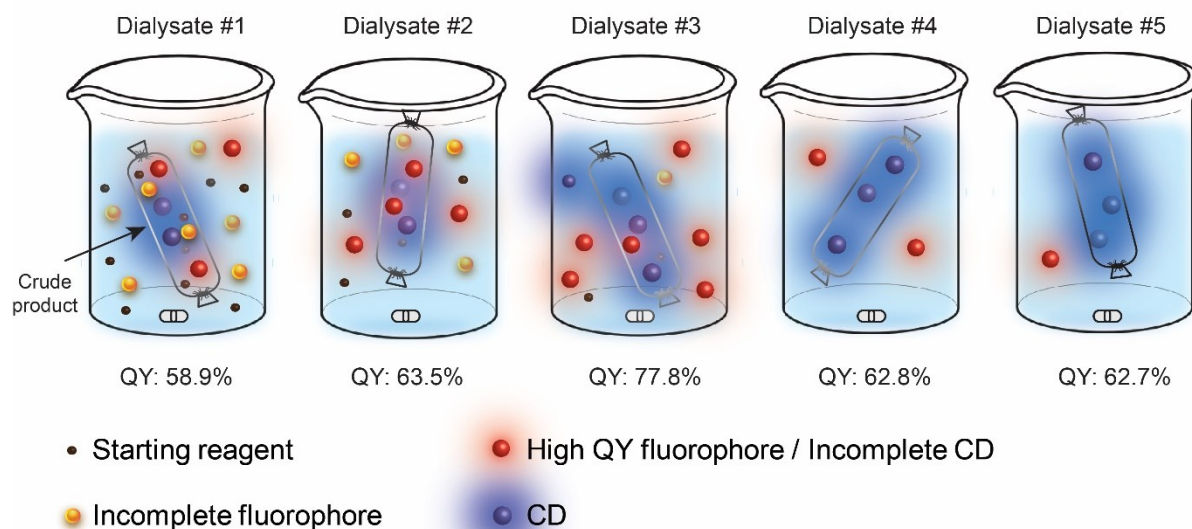


**Figure 16:** Effect of purification on the photoluminescence quantum yield values of CDs. Graphical representation of the changes in fluorescence quantum yield for (A) 375DT3 and (B) 750DT3 CDs, respectively. (C) Tabulation of quantum yield values for 375DT3 and 750DT3 CDs at each step of the purification process. The results illustrate that similar systems may yield drastically different purification profiles.

photons.<sup>123</sup> Although various components can emit at the same wavelength, their QY values can vary greatly based on the efficiency of their radiative pathways. Interestingly, the two different CD systems exhibit markedly different purification profiles (Figure 16A, B). The explanation for the purification profile of the 375DT3 CDs is rather simple. Briefly, the reaction yielded a crude mixture containing several components comprising of partially to fully formed fluorophores along with carbonized CDs, as well as any remaining unreacted starting materials. As all impurities within the sample are smaller than fully formed CDs, the dialysis process successively removes these smaller components, resulting in successively lower QY values at each step, eventually

reaching 19.8%. Subsequent purification via organic washes, further removes unwanted material, eventually converging to a QY value of approximately 12.5%, the true QY value of the 375DT3 CDs. In contrast, the purification profile for 750DT3 CDs, as is depicted in Figure 16B, shows a significantly smaller decrease in the QY value, reaching a plateau at a value of 53.8%. However, the trend observed in the dialysate may offer greater insight into what is occurring throughout purification. Here, the QY first increases with purification, then decreases after reaching a maximum value. As previously stated, the reaction results in a crude mixture containing various components of differing size, absorbance, fluorescence, and QY values. Figure 16B and C, reveal that the QY of the dialysate reaches a maximum at step 3 before dropping and then levelling off to ~ 63%. This unexpected result may be explained in terms of an average QY for the whole system, which is depicted in Figure 17. The first dialysate contains fluorophores with high QY values, as well as unreacted precursors and small non-fluorescent molecules that may absorb, but

#### Graphical Illustration of Dialysis Process for 750DT3 CDs



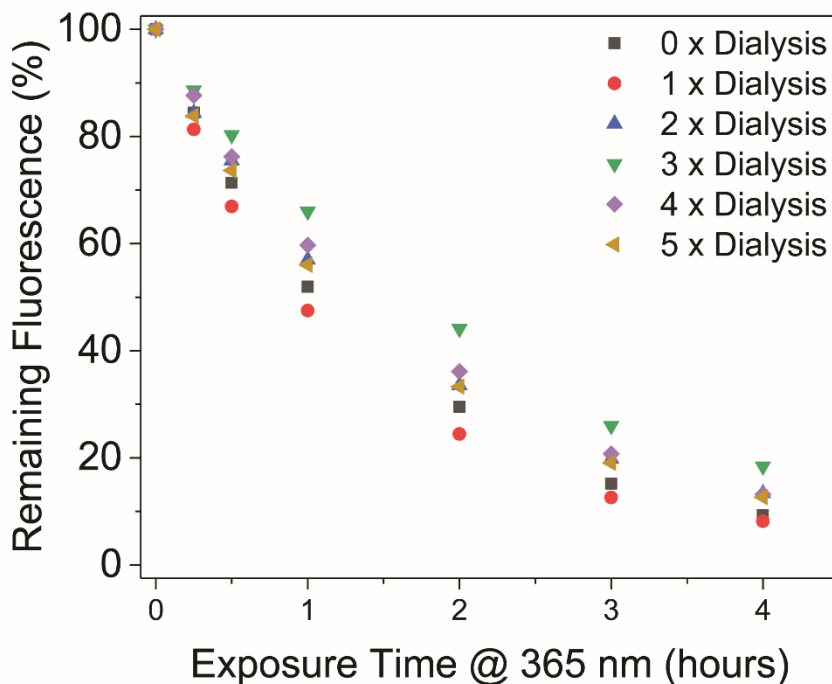
**Figure 17:** Graphic representation of the dialysis purification profile for crude 750DT3 CDs. Four main constituents comprise the crude sample, as described in the figure legend. Dialysis successively removes small, low QY particles, which increase the QY to its maximum value of 77.8% for Dialysate #3. Subsequent dialysis steps remove most high QY fluorophores and incomplete CDs, ultimately levelling off at ~63%. Proportions of the different components are for illustrative purposes only.

exhibit little to no fluorescence, resulting in a lower average QY value. In the ensuing dialysis steps, less abundant, smaller-sized and non-fluorescent components are removed along with the remaining, more abundant, highly luminescent fluorophores increasing the average QY to a maximum of 77.8%, before they are depleted, ultimately stabilizing the QY of the remaining dialysate components at ~63%. Further organic washes of the 750DT3 sample remove the larger, incompletely-formed CDs, resulting in a stable QY of ~53.8%, the apparent inherent value of the 750DT3 CDs. This value is significantly higher than that of the 375DT3 CDs due to the higher concentration of the amine passivating agent used during synthesis.

### **3.3.4. Insights Into Purification Through Photostability and Photobleaching**

We evaluated the photostability of these carbon dots following the various dialysis steps to further confirm the hypothesis put forth above. In this experiment, samples of the 750DT3 CDs that were subjected to 0-5 dialysis steps, were exposed to 365 nm light for 0.25 - 4 hours. Changes in the fluorescence intensity at the 445 nm emission maximum were then monitored and compared to the initial fluorescence value (Figure 18). The results follow a similar trend to that of the QY experiment. Once again, the crude product, which has not been dialyzed and is comprised of a mixture of partially and fully-formed CDs, as well as fluorophores and starting reagents, shows a steady decline in fluorescence to a stable plateau at 9.3% of the initial value. At the first dialysis step, smaller, and likely non-fluorescent impurities (such as unreacted starting reagents and incomplete fluorophores) are expelled from the sample. As such, a larger percentage of the sample is composed of non-photostable fluorophores which degrade upon exposure to the 365 nm light source. This causes a decrease of the fluorescence intensity of the 1 dialysis-step sample to a minimum of 8.2% fluorescence after 4 hours, the lowest value obtained for all samples. Upon further dialysis, the composition of the sample reflects a greater concentration of more photostable,

or possibly non-fluorescent, components. As such, the samples having undergone 2x and 3x



Exposure Time @ 365 nm	Remaining % Fluorescence					
	0 x Dialysis	1 x Dialysis	2 x Dialysis	3 x Dialysis	4 x Dialysis	5 x Dialysis
0 h	100	100	100	100	100	100
0.25 h	84.42	81.30	84.37	88.63	87.63	83.83
0.5 h	71.34	66.94	75.50	80.28	76.24	73.63
1 h	51.96	47.49	56.97	66.00	59.71	56.03
2 h	29.55	24.46	33.53	44.09	36.11	33.28
3 h	15.20	12.60	19.78	25.97	20.75	19.05
4 h	9.32	8.18	13.38	18.43	13.17	12.66

**Figure 18:** Plot and accompanying table showing percent fluorescence remaining compared to initial fluorescence intensity at 445 nm emission maximum after direct exposure to a 365 nm light source for a varying number of hours of 750DT3 CDs.

dialysis steps show progressively lower photodegradation with a maximum of 18.4% residual fluorescence intensity after 3 dialysis steps. Subsequent dialysis steps shift the sample composition and reflect a high purity CD dispersion. Following dialysis steps 4 and 5, a further decrease in the remaining fluorescence intensity is noted with the further removal of relatively photostable, strongly fluorescent non-CD components, until the sample reaches 12.7% of the original

fluorescence intensity. This value is seemingly the true value showing photodegradation in the carbon dots with little to no contribution from other fluorescent impurities within the sample. Consequently, the photodegradation profile of this sample, at various purification steps, reflects the changes in the sample composition, as well as the corresponding optical properties until the purification endpoint is reached.

Our results underscore the need to tailor purification protocols for each synthesis in order to obtain uniform physical and optical properties and highlights the fact that there is no “one-size-fits-all” purification method. As observed throughout the purification of the 750DT3 CDs, this synthesis required dialysis and organic washing for complete removal of impurities. According to the observed changes in their optical and surface properties, only 3 dialysis steps with organic washing were required before stabilization of their physico-optical properties. Conversely, the 375DT3 CDs, synthesized in an identical manner but with a lower concentration of passivating agent, showed continual change to their properties with each subsequent purification step as a result of more impurities and side-products from a less efficient synthesis process. It is also important to note that changes in the 375DT3 CDs properties were only studied up to 5 dialysis steps which could mean further steps are required to obtain purity. It is noteworthy to mention that with the current knowledge of the CD formation process and of the identity of the by-products formed, it is impossible to ascertain the removal of every impurity; however the observed plateaus of the physico—optical properties indicate a suitable endpoint suggesting no further gains from additional purification steps. Nevertheless, the overarching principle remains in that each synthesis of a new CD system should undergo rigorous tracking of changes in their physical and optical properties to optimize the efficiency of the synthesis and of the purification procedure, which leads to uniformity of the CD properties.

### ***3.4. The Importance of Tailoring Purification Protocols***

The literature provides many examples of CDs purified using the same purification protocol despite differences in CD synthesis and properties. However, we have observed here that under different synthesis conditions even systems with identical carbon sources and amine-passivating agents may result in different levels of impurities and side-products produced, which affect the observed properties. Due to the drastic differences in purification needs, system-specific purification procedures need to be developed for each CD system to ascertain their inherent physical and optical properties as well as provide a clear understanding of the functional groups present on the CD surface, thus guiding post-synthesis modifications if desired. Here we have outlined a method of tracking changes in the physical and optical properties of CD systems to help determine the effectiveness of a given purification process on the system and to ensure that the purification end-point is met. This will ensure that the proper purification methods are used for each system and that enough steps are used to obtain full purity of the product while eliminating wasteful and time-consuming additional steps. It is important to understand that this method will require tailoring of the purification techniques and purification time based on the needs of each system and that the proposed purification protocol described above serves only to provide a simple and elegant approach to track the purification endpoint following CD synthesis. The work outlined above is not restricted to CD systems, but can be expanded to monitor purification of other hydrophilic NPs and their properties.

## Chapter 4. Metal Sensing

Two types of systems were used throughout the project to study metal-based sensing and to assess the inherent metal quenching capabilities of CDs. The first type of system was a single-fluorescent CD, where the fluorescence arises from one band in the fluorescence spectrum ascribed to a single optical center in the dot. The second type was a dual-fluorescent system where fluorescence stems from two separate bands ascribed to two optical centers namely the core and surface states.

### 4.1. Characterization

Two different CDs in the single-fluorescent system were investigated and characterized namely ethylenediamine- (ED2) and diethylenetriamine-derived (DT3) CDs. It is important to note that although these systems were used at the onset of the metal quenching studies and optimization of the metal quenching assays, ultimately a different system was selected for the work. The information generated using single-fluorescent CDs however allowed for the development of a more sensitive, selective and robust carbon dot for metal sensing assays. Similar to the single-fluorescent CDs, the physical and optical properties of dual-fluorescent FG-CDs were thoroughly investigated in order to glean a deeper understanding of their surface as this would be critical in the study of the mechanistic aspects of metal sensing.

#### 4.1.1 Exploring Differences in Size and Composition

##### 4.1.1.1. Single-Fluorescent CDs

The size and morphology of the particles were estimated by TEM. Both quasi-spherical, the sizes of the particles were found to be  $2.2 \pm 0.4$  nm for ED2-CDs and  $2.6 \pm 0.4$  nm for DT3-CDs.<sup>64</sup> The TEM images and size distributions are shown in Figure 19A and B. It should also be noted that the contrast for the TEM images is quite poor due to the lack of crystallinity in the

amorphous CDs. This is confirmed by their XRD patterns in Figure 19C, which show an amorphous halo for both CDs.<sup>64</sup>

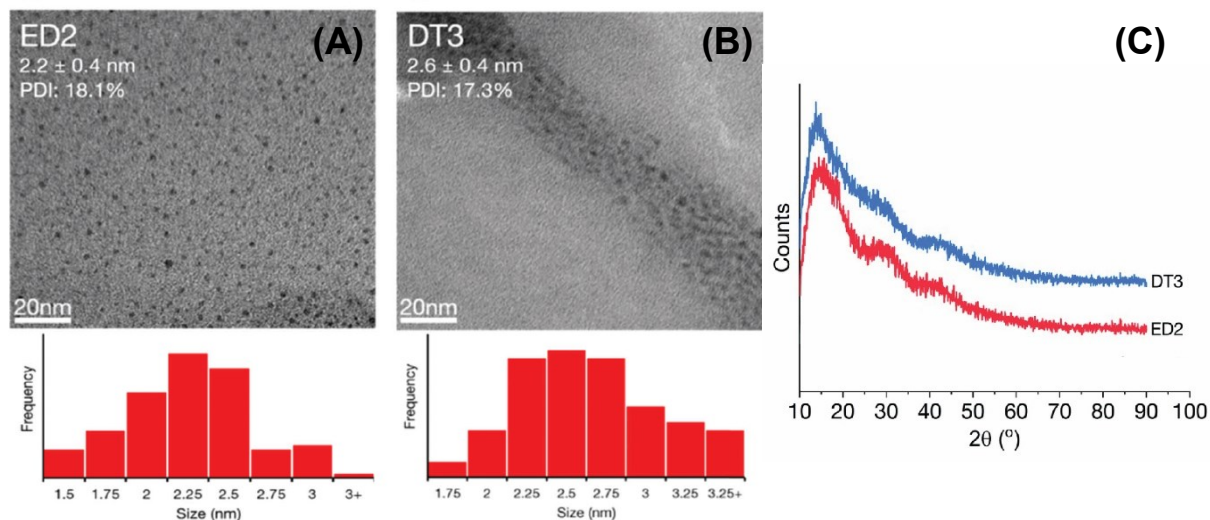


**Figure 19:** TEM image and size distribution plot of (A) ED2-CDs and (B) DT3-CDs alongside the (C) XRD patterns for both CDs. Images adapted from: Manioudakis *et. al.*<sup>64</sup>

The surface functional groups of the ED2-CDs were analysed using FTIR, as displayed in Figure 20A. In this spectrum, a strong stretch at  $1698\text{ cm}^{-1}$  shows the presence of carboxylic C=O groups, with a small shoulder at  $1655\text{ cm}^{-1}$  for amide C=O. Broad stretches between  $2668$  and  $3661\text{ cm}^{-1}$  are associated with N-H bonds in amines/amides and O-H bonds from hydroxyls and possibly carboxylic -OH groups. Another C-N stretch at  $1164\text{ cm}^{-1}$  further supports the idea that amine functional groups are present on the CD surface. N-H bend/C=C stretch are found at  $1576\text{ cm}^{-1}$ . Finally, bends at  $1399\text{ cm}^{-1}$  ascribed to C-H groups are observed. This is in accordance with published reports in the literature.<sup>64</sup>

Similarly, DT3-CDs were characterized by FTIR and showed many of the same stretches in Figure 20B. A broad stretch at  $3382\text{ cm}^{-1}$  is associated with amide and amine N-H groups, whereas at  $2947\text{ cm}^{-1}$  a wide stretch is noted and ascribed to O-H bonds from hydroxyl/carboxylic

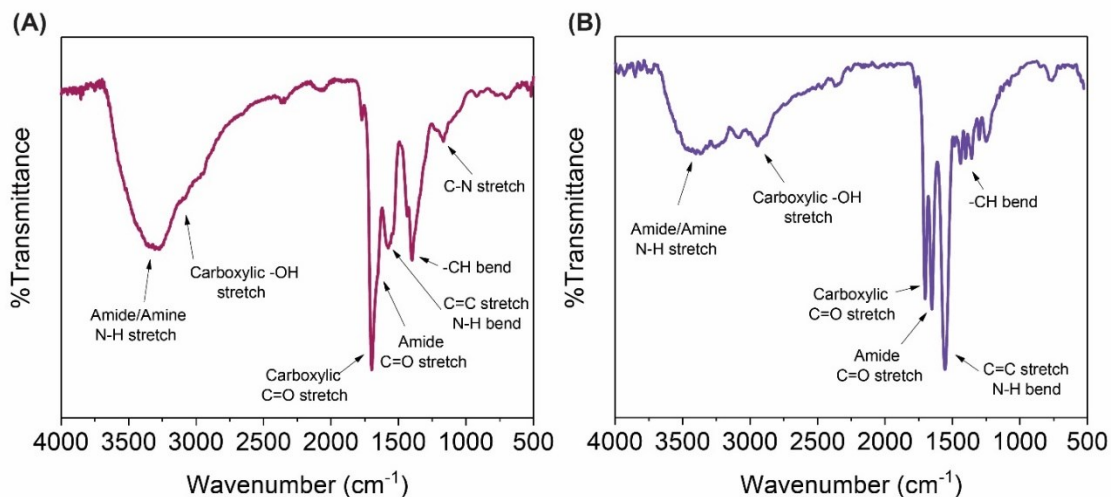


**Figure 20:** FTIR spectrum of (A) ED2-CDs and (B) DT3-CDs showing the presence of amide and carboxyl stretches as well as N-H, C-H and O-H functional groups.

-OH groups. Strong stretches at  $1705\text{ cm}^{-1}$  and  $1648\text{ cm}^{-1}$  correspond to carboxylic C=O groups and amide C=O groups, respectively. A strong stretch at  $1555\text{ cm}^{-1}$  correlates to a N-H bend/C=C stretch. Finally, observed at  $1441$ ,  $1401$ , and  $1357\text{ cm}^{-1}$  are alkane and aldehyde C-H bends.

Further analyses of the carbon dot surface and elemental composition analysis was carried out using XPS. Although XPS is typically deemed a surface technique with a penetration depth of approximately 10 nm, CDs are small enough in diameter that this technique can be used to penetrate through the entire CD and reveal its total composition.<sup>124</sup> ED2-CDs were found to be composed of 72.8 % carbon, 9.1 % nitrogen and 17.4 % oxygen.<sup>64</sup> Deconvolution of their C1s peak revealed binding energies at 285.09, 286.54 288.26 eV, which corresponded to C-C, C-O/C=O and amide/carboxylic C=O bonds, respectively. The deconvoluted N1s peak showed two binding energies at 400.42 and 402.20 eV. These were associated with both alkyl and amide N-C bonds and N-O bonds, respectively. Finally, the O1s was deconvoluted and the following binding energies were observed: 531.90 eV corresponding to amide/carboxylic O=C bonds and 534.91 eV

ascribed to O-C bonds.<sup>64</sup> The functional groups revealed through XPS are in accordance with the FTIR data collected for ED2-CDs.

The elemental composition of DT3-CDs was determined to be 65.2 % of carbon, while 15.0 % and 19.8 % were ascribed to nitrogen and oxygen respectively.<sup>64</sup> By deconvoluting the C1s peak, binding energies at 285.08 eV for C-C bonds, 286.32 eV for C-O bonds and 287.40 eV for amide C-N/N-C=O were observed. The deconvoluted N1s peak showed amide and alkyl N-C bonds at 400.38 eV and N-O bonds at 402.22 eV binding energies. Finally, the deconvolution of the O1s peak revealed two binding energies at 531.32 eV and 532.45 eV associated with amide and carboxylic O=C bonds, respectively.<sup>64</sup>

**Table 3:** Summary of characterization for ED2-CDs showing (A) the functional groups observed from FTIR analysis (B) the functional groups observed from XPS analysis and (C) the elemental composition of the dots.

**(A)** FTIR Analysis

Wavenumber (cm <sup>-1</sup> )	Type of vibration	Type of bond	Functional group
1164	stretch	C-N	amine/amide
1399	bend	C-H	alkane
1576	bend	N-H	amine/amide
1576	stretch	C=C	aromatic
1655	stretch	C=O	amide
1698	stretch	C=O	carboxylic acid
2668-3661	stretch	N-H	amine/amide
2668-3661	stretch	O-H	hydroxyl/carboxylic acid

**(B)** XPS Analysis

Peak	Binding energies (eV)	Type of bond	Functional group
<b>C1s</b>	285.09	C-C	-
	286.54	C-O/C=O	-
	288.26	C=O	amide/carboxylic
<b>N1s</b>	400.42	N-C	alkyl/amide
	402.2	N-O	-
<b>O1s</b>	531.9	O=C	amide/carboxylic
	534.91	O-C	-

**(C)** Elemental Analysis

Element	Percent Composition
Carbon	72.80%
Oxygen	17.40%
Nitrogen	9.10%

The results of the physical characterization for ED2-CDs and DT3-CDs are summarized in Tables 3 and 4, respectively.

**Table 4:** Summary of characterization for DT3-CDs showing (A) the functional groups observed from FTIR analysis (B) the functional groups observed from XPS analysis and (C) the elemental composition of the dots.

**(A)** FTIR Analysis

Wavenumber (cm <sup>-1</sup> )	Type of vibration	Type of bond	Functional group
1357, 1401 & 1441	bend	C-H	alkane/aldehyde
1555	bend	N-H	amine/amide
1555	stretch	C=C	aromatic
1648	stretch	C=O	amide
1705	stretch	C=O	carboxylic acid
2947	stretch	O-H	hydroxyl/carboxylic acid
3382	stretch	N-H	amine/amide

**(B)** XPS Analysis

Peak	Binding energies (eV)	Type of bond	Functional group
<b>C1s</b>	285.08	C-C	-
	286.32	C-O	-
	287.4	C-N/N-C=O	amide
<b>N1s</b>	400.38	N-C	alkyl/amide
	402.22	N-O	-
<b>O1s</b>	531.32	O=C	amide
	532.45	O=C	carboxylic

**(C)** Elemental Analysis

Element	Percent Composition
Carbon	65.20%
Oxygen	19.80%
Nitrogen	15.00%

4.1.1.2. Dual-Fluorescent CDs

As with the single-fluorescent systems, the size and morphology of the dual-fluorescent CDs (FG-CDs), prepared using formamide and glutathione precursors, were confirmed by TEM imaging. Figure 21A shows a TEM image of the CDs with an in-laid size distribution plot. These images reveal that the CDs are quasi-spherical with an average size of  $7.3 \pm 1.2$  nm, and a relatively broad size distribution.<sup>66</sup> Again, as with all CDs, a lack of crystallinity is observed via XRD, where

the diffraction pattern shows the lack of any distinct peaks (Figure 21B). Instead an amorphous halo is depicted, supporting the claim that these CDs are amorphous.<sup>66</sup>

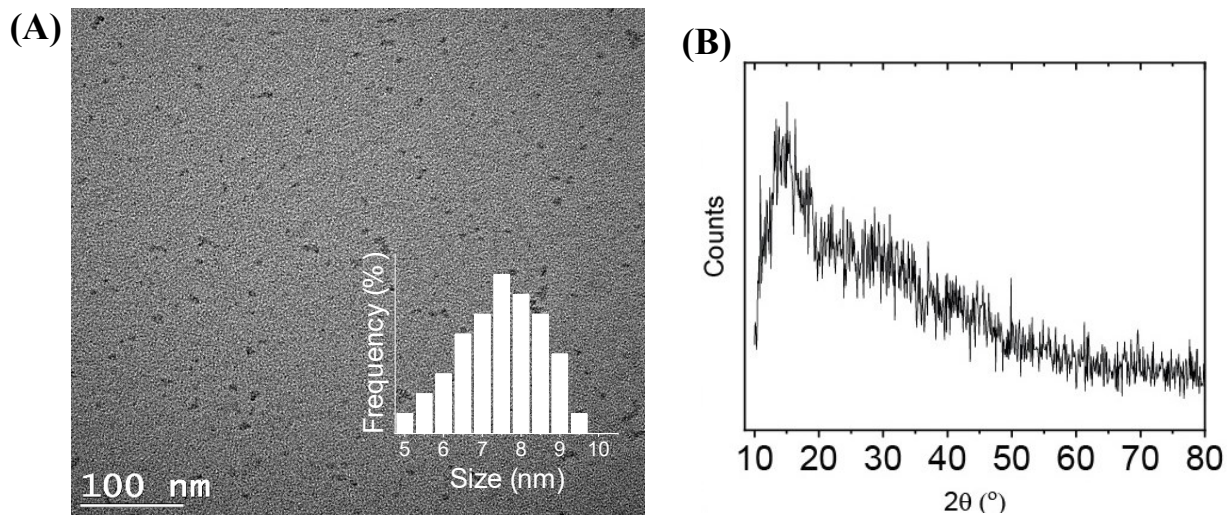


**Figure 21:**(A) TEM image of FG-CDs with in-laid size distribution plot showing an average size of  $7.3 \pm 1.2$  nm. (B) XRD pattern of FG-CDs showing an amorphous halo.

Their surface chemical groups were identified using FTIR-ATR spectroscopy. The FTIR spectrum, shown in Figure 22, exhibits broad stretches ranging from  $3000$  to  $3500$   $\text{cm}^{-1}$  associated

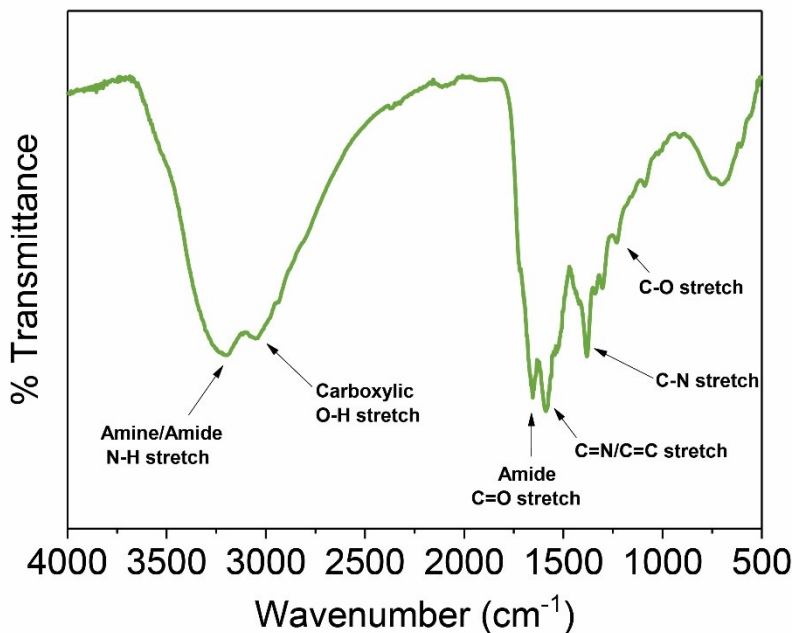


**Figure 22:** FTIR spectrum of FG-CDs showing the presence of amide and carboxyl stretches as well as N-H and O-H functional groups.

with N-H bonds in amines/amides and O-H bonds from hydroxyl/carboxylic acid groups on the CD surface. The presence of amide functional groups is indicated by the strong amide C=O stretch at 1645  $\text{cm}^{-1}$ . This is further supported by the presence of C-N amide stretches at 1307  $\text{cm}^{-1}$  and 1386  $\text{cm}^{-1}$ . A stretch at 1583  $\text{cm}^{-1}$  may also indicate the presence of C=C and C=N functional groups.<sup>66</sup>

These findings were also confirmed by the XPS data collected for these CDs shown in Figure 23. The survey spectrum revealed that the elemental composition of the CDs was broken down to 53.1 % carbon, 26.1 % oxygen, 17.4 % nitrogen and 3.4 % sulfur<sup>66</sup>. Deconvolution of the Carbon (C1s), nitrogen (N1s), oxygen (O1s) and sulfur (S2s) binding energies revealed the presence of the following functional groups within the CDs. First, deconvolution of the C1s (shown in Figure 23B) indicated binding energies at 288.68 eV, 286.89 eV and 285.58 eV associated with C-C/C=C, C-O and C=O/C=N functional groups, respectively. The oxygen O1s binding energies (Figure 23C) uncovered the presence of C-OH/C-OC and C=O functional groups at 533.26 and 532.02 eV, respectively. The deconvoluted N1s binding energies in Figure 23C at 402.71 and 400.58 eV were ascribed to  $\text{NH}_2$ /pyrrolic N and graphitic N, respectively. Finally, for S2p (Figure 23E), a thiol functional group shows a binding energy at 165.51 eV, while two thiophene groups were linked to binding energies at 164.14 and 163.38 eV.<sup>66</sup> The results of the physical characterization for FG-CDs are summarized in Table 5.

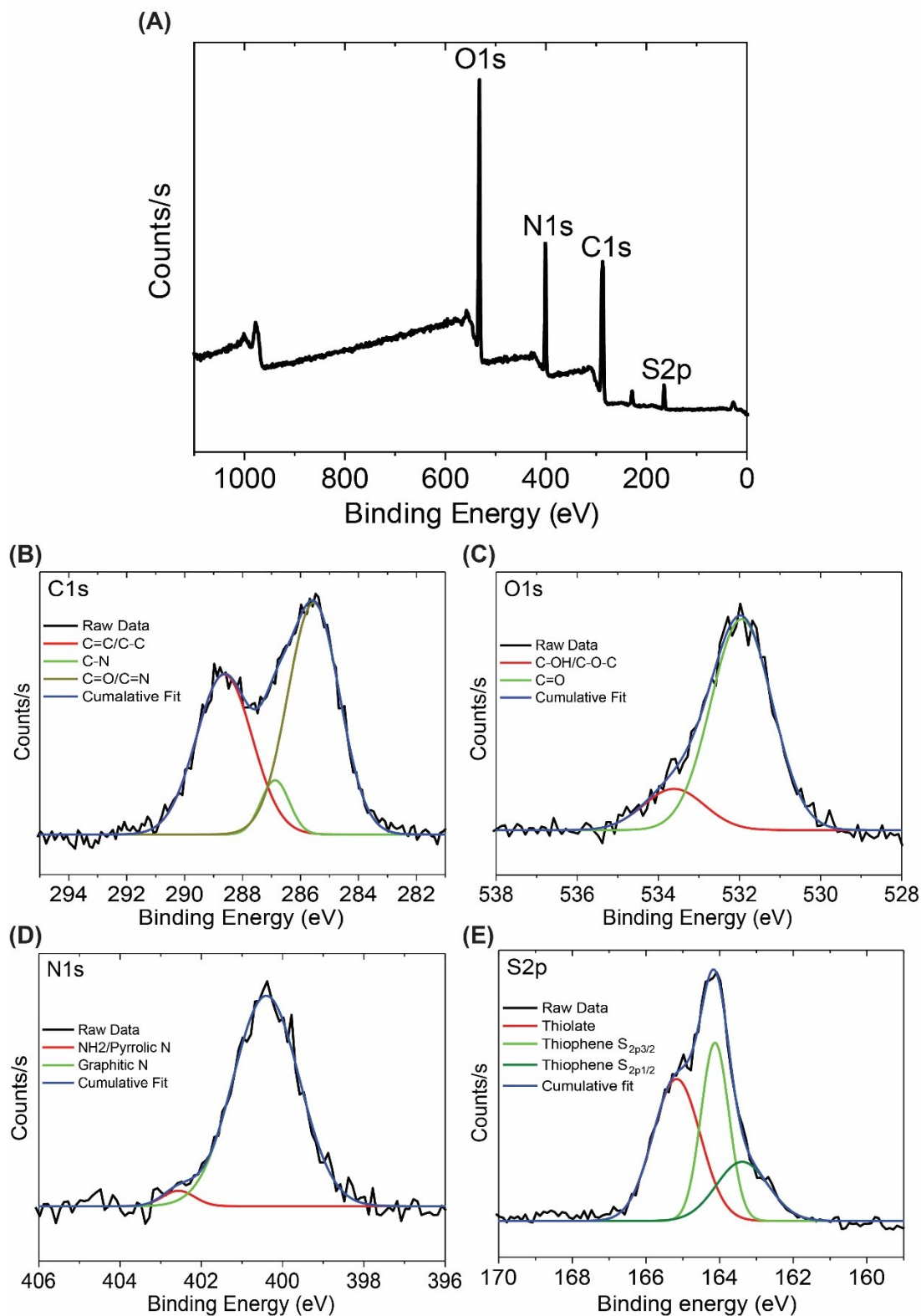
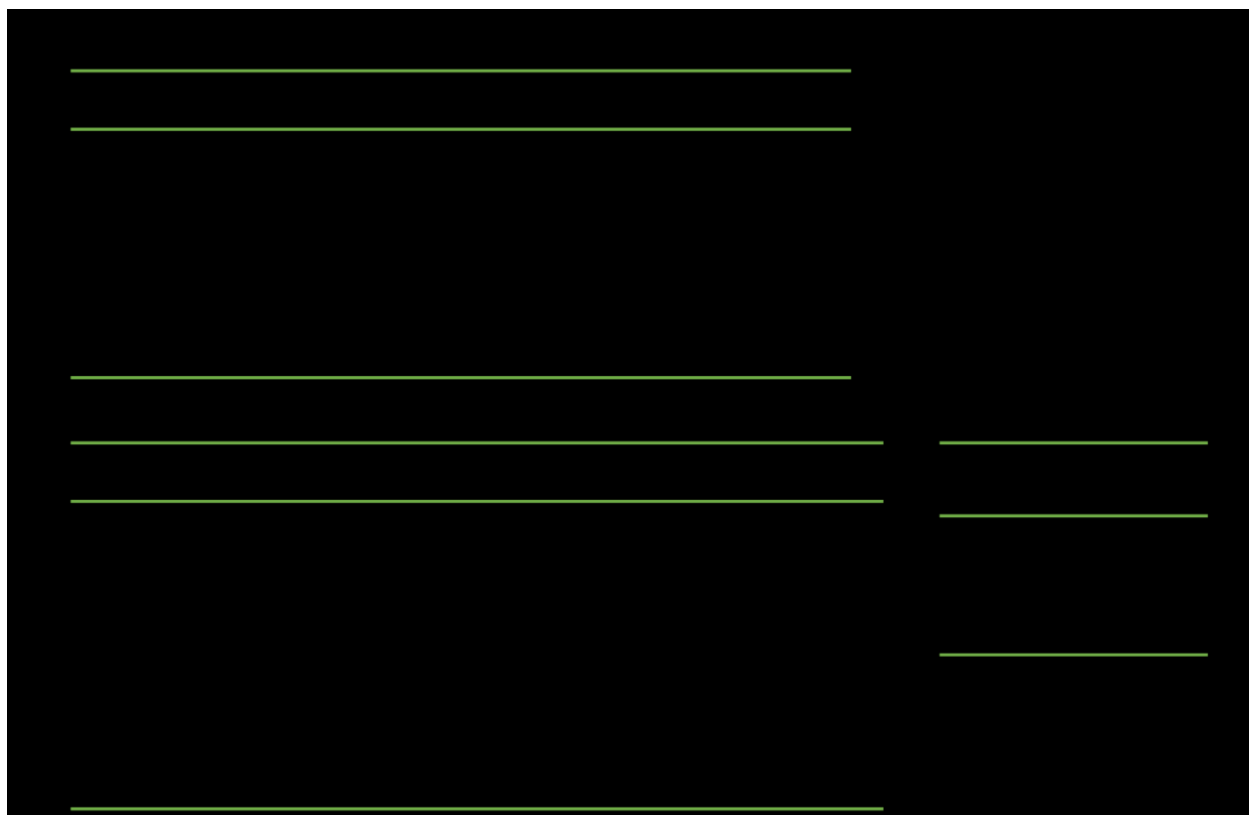


**Figure 23:** (A) XPS survey spectrum of FG-CDs showing binding energies of C1s, N1s, O1s and S2p. Spectra of deconvoluted binding energies reveal (B) a maximum for C1s at 286.08 eV, (C) a maximum at 400.08 eV for N1s (D) a maximum at 532.08 eV for O1s and (E) for S2p a maximum at 165.08 eV.

During the course of the initial experiments, it was suspected that the observed and often variable quenching was due to electrostatic interactions between the CDs and the metallic cations. To better understand the nature of these interactions, the surface charge of the CDs was investigated using zeta potential. The overall particle charge was found to be -22.3 mV. Despite the overall negative charge on the particle, both positive and negative components were found on the CD surface, which is consistent with the FTIR and XPS data showing the presence of various surface functional groups namely carboxyls, amides, amines, hydroxyls and thiols.

**Table 5:** Summary of characterization for FG-CDs showing (A) the functional groups observed from FTIR analysis (B) the functional groups observed from XPS analysis and (C) the elemental composition of the dots.



## 4.1.2. Investigating the Optical Properties

### 4.1.2.1. Single-Fluorescent CDs

The absorbance and fluorescence emission of both CDs were examined by UV-vis absorbance and fluorescence spectroscopies. Firstly, the absorbance and fluorescence spectra for ED2-CDs is displayed below in Figure 24A. Two absorption bands are visible at 245 nm and at 338 nm associated with the  $\pi \rightarrow \pi^*$  transition of the C=C  $sp^2$  domains in the CD core<sup>119, 120</sup> and the  $n \rightarrow \pi^*$  transition of carbonyl and/or amine functional groups<sup>64, 86, 119</sup>, respectively. The fluorescence emission shows an emission maximum centered at 447 nm following 350 nm excitation.

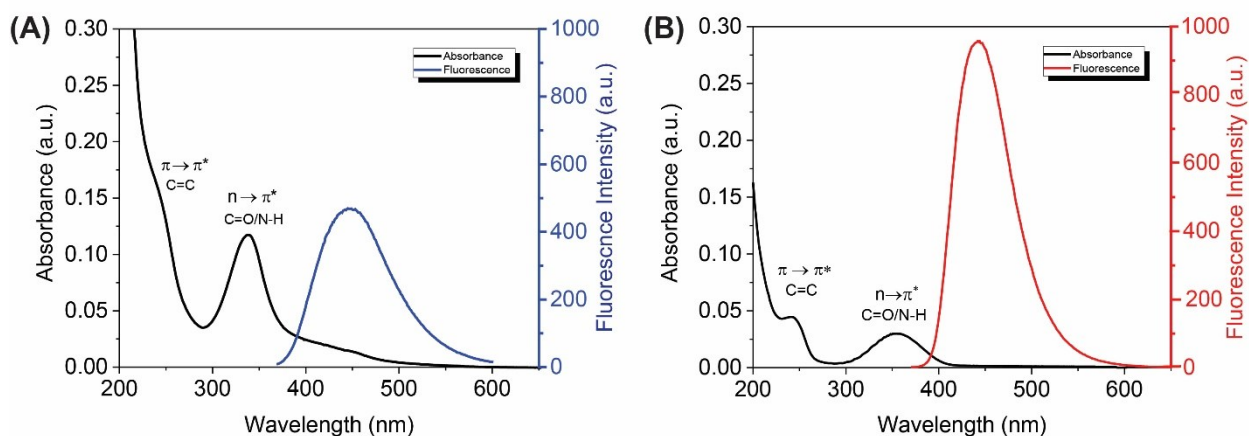


**Figure 24:** UV-vis and overlaid fluorescence spectrum for (A) ED2-CDs and (B) DT3-CDs. Both absorbance spectra show a  $\pi \rightarrow \pi^*$  electronic transition at  $\sim 245$  nm and a  $n \rightarrow \pi^*$  transition at  $\sim 350$  nm. Fluorescence shows a single emission at  $\sim 445$  nm in both spectra when excited at 350 nm.

The DT3-CDs were noted to possess similar absorbance and fluorescence profiles as shown in Figure 24B. Electronic transitions in the absorbance spectrum were observed at 243 nm, associated with C=C bonds in the aromatic core, and at 355 nm, ascribed to carboxylic or amide C=O and amine functional groups.<sup>64, 86, 119, 120</sup> Once more, the emission spectrum showed a single peak centered at 442 nm. It is important to also note that the DT3-CD emission is much stronger in comparison to that of the ED2-CDs despite a lower absorbance at 350 nm. This is due to the

significant increase in fluorescence QYs with increasing amounts of passivation by nitrogen functional groups on the CD surface. ED2-CDs exhibited a QY of 15.9%, whereas the value for DT3-CDs was almost twice that at 33%.<sup>64</sup>

Finally, fluorescence lifetime measurements were measured for both these CD systems with the results summarized in Table 6. Both systems evidence a short lifetime component, believed to be derived from the radiative relaxation on the surface of the NP, as well as a long lifetime component, which stems from a relaxation and energy transfer from the CD core to the surface.<sup>64, 83</sup> For ED2-CDs the short component of 0.3 ns accounts for 94.2% of the population, while the long component of 7.1 ns makes up only 5.8% of the population.<sup>64</sup> Similarly, DT3-CDs possess a short lifetime component of 0.3 ns, which accounts for 96.6% of the population, while the much longer component is of 11.2 ns, but only accounts for 3.4% of the population.<sup>64</sup>

**Table 6:** Summary of the fluorescence lifetime values for ED2-CDs and DT3-CDs with populations.

Carbon Dot	$\tau_1$ (ns)	Population 1 (%)	$\tau_2$ (ns)	Population 2 (%)	$\chi^2$
ED2	0.3	94.2	7.1	5.8	1.22
DT3	0.3	96.6	11.2	3.4	2.06

#### 4.1.2.2. Dual-Fluorescent CDs

The absorbance of the dual-fluorescent CDs was measured via UV-Vis absorbance spectroscopy (Figure 25A), which shows that the particles can be excited in several regions of the spectrum. First, there is a weak absorption band near 300 nm, which corresponds to the  $\pi \rightarrow \pi^*$  transition of the C=C  $sp^2$  domains in the carbon dot core.<sup>64</sup> The strongest absorption occurs between 350 and 425 nm, with a maximum at 420 nm associated with the  $n \rightarrow \pi^*$  transition of the carbonyl and/or amine groups within the CDs. The last transition is the  $n \rightarrow \pi^*$ , which occurs

between 600 - 700 nm, is ascribed to C=O, C=N and C=S functional groups in the aromatic carbon network.<sup>125, 126</sup>

Fluorescence spectroscopy was used to investigate their emission revealing that these CDs have a dual-fluorescent nature. Their fluorescence spectrum when excited at 420 nm, shown in Figure 25B, displays a weaker emission in the blue region, centered at 480 nm, along with a stronger emission in the red region of the spectrum at 680 nm with a shoulder at 650 nm. Based on literature reports<sup>52, 83-85</sup> and previous studies in our own research group<sup>66, 75</sup>, we believe the blue fluorescence stems from radiative re-combination in the aromatic core of the particle, meaning that the NP's environment minimally affects this fluorescence emission.<sup>52, 66, 75, 84</sup> However, the red fluorescence counterpart is thought to arise from radiative recombination in aromatic networks on the surface of the CDs, where the functional groups attached to this network have red-shifted the observed fluorescence band. As such, this emission suffers from changes in the CD's environment

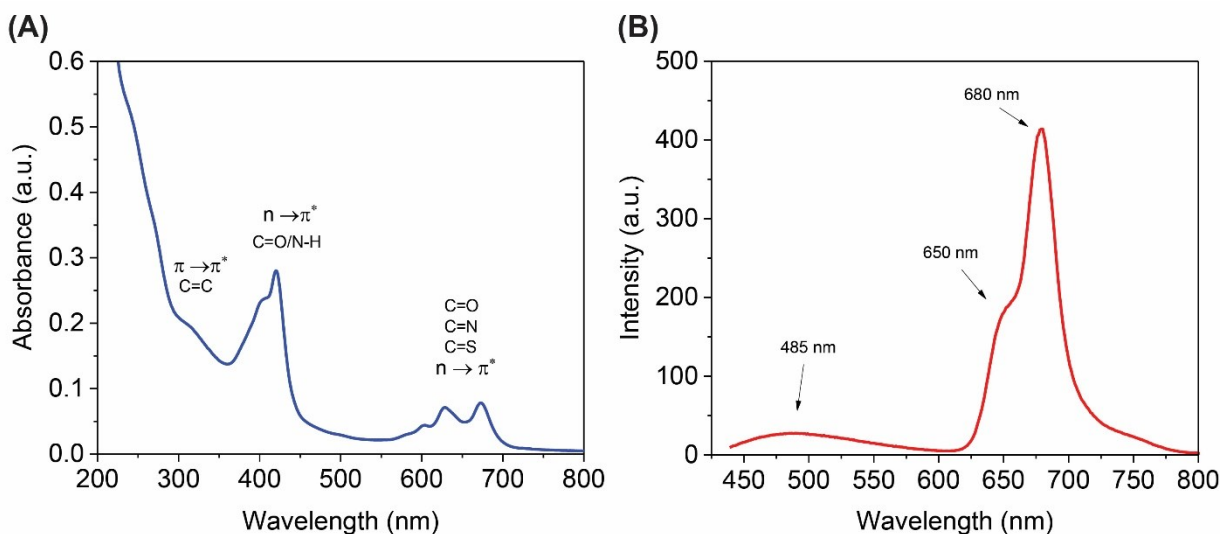


**Figure 25:** (A) The UV-Vis absorption spectrum of FG-CDs shows three main electronic transition regions: a  $\pi \rightarrow \pi^*$  transition at  $\sim 300$  nm; a  $n \rightarrow \pi^*$  transition at  $\sim 420$  nm; and a  $n \rightarrow \pi^*$  transitions from 600 to 700 nm. (B) The fluorescence spectrum of FG-CDs shows dual emission at 485 nm and 680 nm, with a shoulder at 650 nm.

far more prominently than the core.<sup>52, 66, 75, 83, 85</sup> This theory is further supported by the findings of the metal quenching assays (*vide infra*).

The fluorescence lifetimes for FG-CDs were measured and two lifetime components were noted namely a short component of 0.6 ns, comprising ~25% of the population, and a long component of 5.7 ns representing ~75% of the population. The long component is believed to be associated with the blue fluorescence, stemming from the core of the particle, and the short component with the red counterpart, originating from the surface of the dot. This is supported by previous data showing that the long component disappears when a bandpass filter, blocking the blue emission from reaching the detector, is used during fluorescence lifetime measurements.<sup>96</sup> As for the QY measurements, when excited at 450 nm, FG-CDs were found to have an average QY of 6.5%, with 6.1% being associated with the stronger red component and only 0.4% with the weaker blue fluorescence.<sup>66</sup>

#### ***4.2. Single vs. Dual-Fluorescent Systems***

The choice of CD systems was mainly determined by the nature of the fluorescence. Ultimately, the dual-fluorescent system was more advantageous to work with as ratiometric detection could be performed. When performing quenching assays, instead of measuring the absolute intensity of the maximum peak, the integrated area under the curve is measured to account for changes in peak shape. However, this can be problematic when working with a single-fluorescent system as these systems are more susceptible to changes in the environment or instrument response. In a single-fluorescent system, such as in Figure 26A, the integrated area under the curve is measured like in Figure 26C. However, if the instrument response changes suddenly, then the peak intensity drops, as in Figure 26E. Suppose this drop coincides with an overall integrated area that is half of the original value, then during a quenching assay, this drop

may be wrongfully ascribed to quenching by metal ions. However, if instead a dual-fluorescent system is used as in Figure 26B, the integrated area then becomes a ratio of the two fluorescence peaks. In Figure 26D, this area corresponds to the ratio of the integrated area of the red peak over the integrated area of the blue peak. When the instrument responses changes, this time both peaks

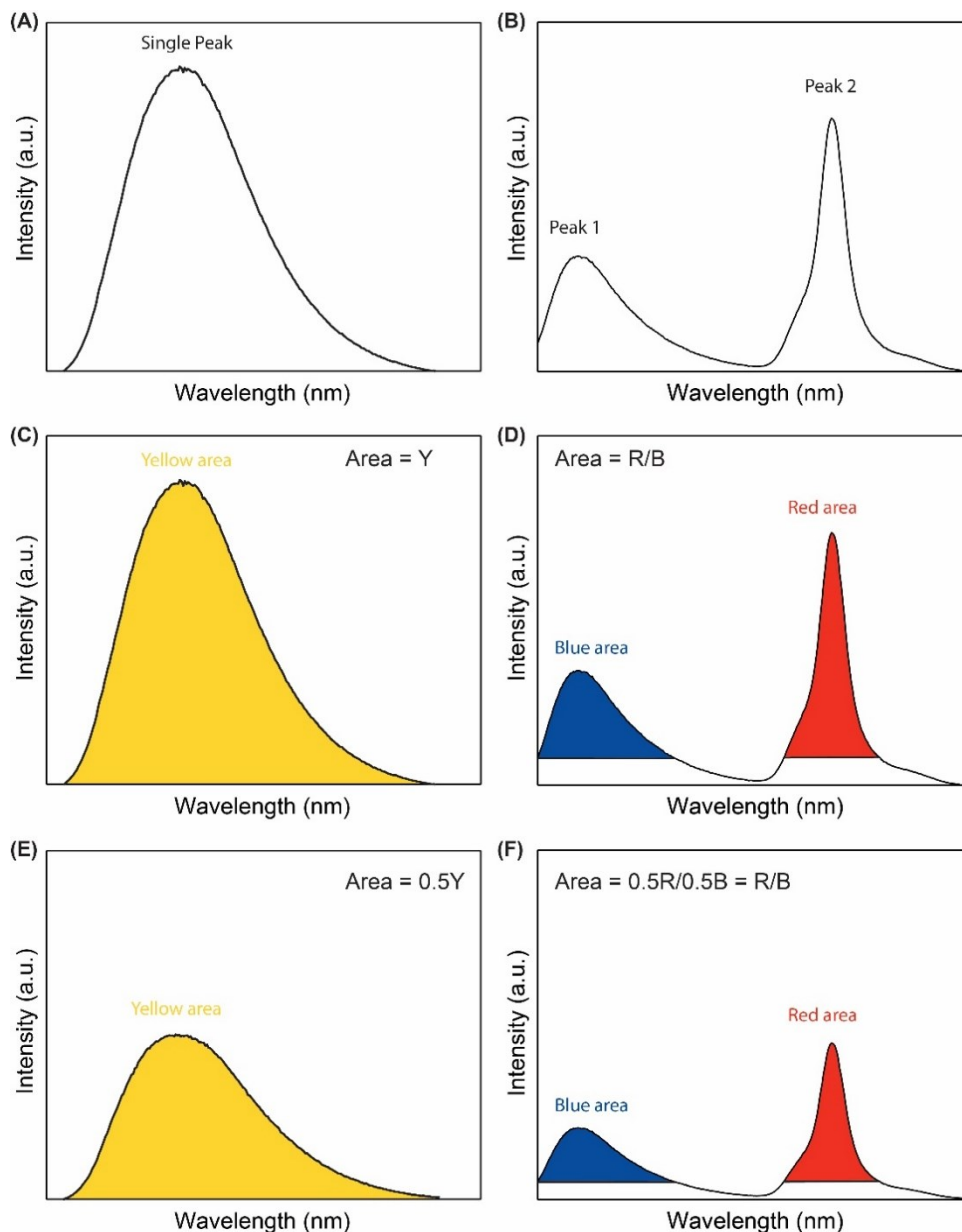


**Figure 26:** (A) Graphical representation of the single-fluorescent CD spectrum (B) Integrated area under the curve of the single-fluorescent CD system before and (C) after a reduction of the peak intensity (D) Graphical representation of the dual-fluorescent CD system (E) Integrated area under the curve of the dual-fluorescent CD system before and (F) after a reduction of the peak intensity.

in Figure 26F are reduced by the same amount. Again, assuming this drop coincides with an area that is half of the original value, the area then becomes half the red area over half the blue area. Therefore, the overall area remains the same as the original value. As such, ratiometric measurements account for fluctuations in the instrument response or environmental changes where both peaks will be affected equally. Therefore, despite the use of single-fluorescent CDs during optimization, the dual-fluorescent CDs were selected for the final metal quenching assays. In this case, the area of the 680 nm red peak was integrated and compared relative to the area of the 485 nm blue peak to determine the overall red-to-blue (R/B) ratio (*vide infra*). The R/B ratio was tracked as a function of metal concentration and plotted to build a calibration curve from which metal concentrations in unknown samples can be determined. It is important to note that for the sake of simplicity and to better compare all systems, following completion of the optimization steps, the initial R/B ratio was normalized to a value of 1 for all quenching assays.

### ***4.3 Optimizing and Determining the Quenching Capabilities of CDs***

Having characterized the physico-optical properties of the dots, metal quenching assays were carried out to assess the potential for metal sensing in model aqueous systems using these CD optical probes. It is noteworthy to highlight that initial works focused on the use of ED2- and DT3- CDs (single fluorescent band) prior to transitioning to FGCDs where a ratiometric sensing approach was adapted for enhanced performance and detection capabilities.

#### **4.3.1. Metal Selection**

The first aspect of metal sensing assays involves the selection of a wide variety of metals ions with which quenching assays will be performed. Here we aimed to select a representative sample of metal ions that would best showcase differences in quenching behaviour due to changes in metal oxidation state, ionic size, ionic charge and number of valence electrons. To accomplish

this, we turned our attention to common, and affordable, metals in the first row of the transition metals. Iron, cobalt, nickel and copper, first row transition metals with similar sizes, were all selected to showcase the effect of the difference in number of valence electrons on quenching. Of these metals, cobalt, nickel and copper all possessed a +2 oxidation state, whereas iron had a +3 oxidation state. This allowed for the comparison of quenching by metals with different oxidation states. To allow for further comparisons, a second first row transition metal with a +3 oxidation state, namely chromium, was also investigated. To explore the effect of size, lead and mercury were added as significantly larger ions than the first row transition metals.<sup>127</sup> Finally, since all the metals selected were predominantly transition metals, two lanthanides, gadolinium and dysprosium, were explored to evaluate quenching of the dots. All metals were used in the chloride salt form to ensure that no changes can be ascribed to a difference in the counter ion.

#### **4.3.2. Time Dependence**

One concern with quenching assays was that the CDs may require an equilibration time, to coordinate with the metal ions; meaning there would be a time dependence for the quenching assays. As such, time dependence experiments were performed to determine whether fluorescence intensity would change as a function of time at a given metal ion concentration. The time range selected was one over which quenching assays could be reasonably performed, therefore it could be determined whether at the end of the quenching assay there may be increased quenching due to delayed binding of metals to the CD. Figure 27 exhibits the fluorescence spectra of a 1.25  $\mu\text{g/mL}$  DT3-CD solution containing 30  $\mu\text{M}$  of cobalt (II) ions. Here, no changes in fluorescence intensity are observed as a function of time elapsed since the addition of the metal ions (between 0 and 20

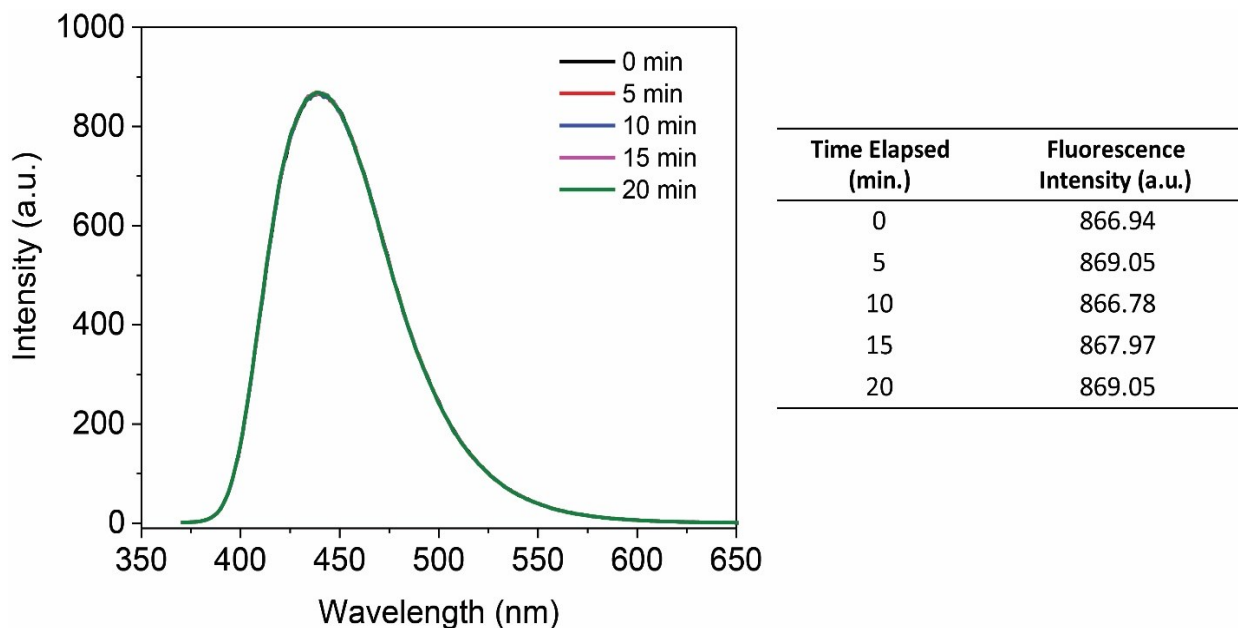


**Figure 27:** Fluorescence spectra of a 1.25 µg/mL DT3-CD solution with 30 µM of cobalt (II) ions showing no time dependence over a 20 minute interval with accompanying table listing fluorescence intensity values over time.

minutes). This experiment was repeated with different metal ions as well as with ED2-CDs. It was then concluded that time had no bearing on the quenching experiments, therefore shorter stirring times, following the addition of metal ions, of ~20 seconds were selected for all further experiments.

### 4.3.3. Concentrations

Next, we optimized the concentrations of both CDs and metal ions used during quenching assays. Very low CD concentrations were selected to avoid both inner-filter effects and fluorescence intensities exceeding the limits of the detector. Instead of a fixed CD concentration, a range of concentrations was used during experimentation to allow the absorbance to be adjusted to a specific value of 0.1 a.u. for the single-fluorescent CDs and 0.3 a.u. for the dual-fluorescent CDs (this value is higher due to lower QYs for these CDs, as well as previous experiments from our lab showing no inner-filter effects up to 0.45 a.u. for dual-fluorescent CDs), thus accounting for any batch-to-batch variation of the CDs' properties. As such, the following concentration

ranges were used: 1-10  $\mu\text{g}/\text{mL}$  for ED2-CDs and 0.2-1.5  $\mu\text{g}/\text{mL}$  for DT3-CDs. Additional experiments were performed to determine whether small variations in the CD

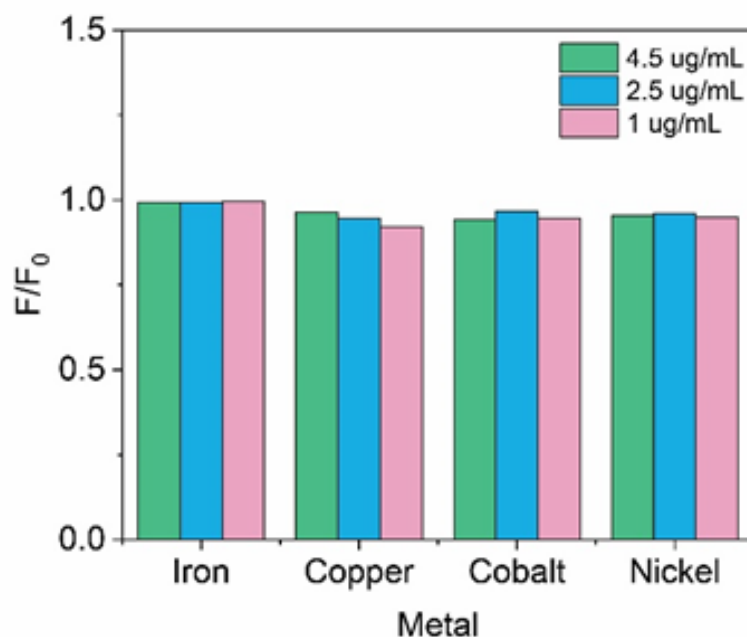


**Figure 28:** Ratio of the integrated fluorescence area, relative to the original fluorescence values, of 4.5, 2.5 and 1  $\mu\text{g}/\text{mL}$  ED2-CD solutions with 1  $\mu\text{M}$  concentrations of different metal cations.

concentrations greatly affected quenching. The results, displayed in Figure 28, show slight fluctuations, but no significant changes were noted.

Initial metal sensing assays were carried out with metal concentrations ranging from 0 to 1 mM, the results of which can be seen in Figure 29. Here, changes in the optical properties of a 2.5  $\mu\text{g}/\text{mL}$  ED2-CD solution were analyzed. Although strong quenching was observed in the fluorescence spectrum (Figure 29B), it was likely due to inner-filter effects from a highly concentrated solution as shown in the absorbance spectrum (Figure 29A). Here, the absorbance value is in excess of 1.75 a.u., well above the concentration where inner-filter effect can be observed.<sup>128</sup> Moreover, 1 mM (> 150 ppm) iron levels are far above both the safe drinking water concentration (0.3 ppm) as well as the concentration that is regularly found in natural waters (1

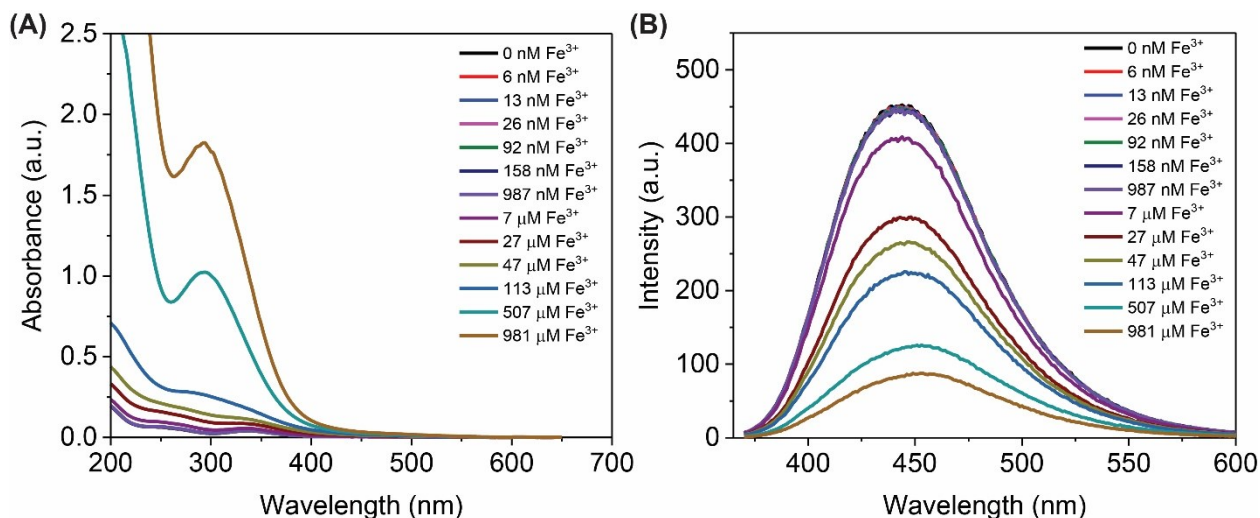


**Figure 29:** Quenching assay data for 2.5 µg/mL of ED2-CDs with concentration range from 0 – 1mM showing (A) absorbance spectra with evidence of inner-filter effect and (B) fluorescence spectra with excitation wavelength of 350 nm for maximum emission at 450 nm.

ppm) in Canada.<sup>18</sup> The same applies for most, if not all, metal contaminants tested throughout the course of this work. However, from Figure 29, it can be deduced that no significant quenching is observed below 1 µM. Therefore, this system seems ineffective at detecting metal ions at environmentally relevant concentrations (1ppm or less). These assays were repeated with DT3-CDs and showed similar results. This pointed to the challenge of working with single fluorescent CDs, which could not be used to detect lower concentrations of metal cations. As such, dual-fluorescent CDs were then investigated to determine whether metal detection at lower concentrations was possible.

In an attempt to determine the lowest LOD possible for the CDs tested, focus was placed on testing very small concentrations of metal ions, particularly in the sub 100 nM range. Figure 30 shows the result of such a quenching experiment performed using 35 µg/mL of FG-CDs with lead (II) ions. It was found that at these ranges of concentrations, quenching is difficult to assess and the linearity of the observed trend was compromised. This linear trend related to fluorescence area ratios will be further discussed in the following sections.

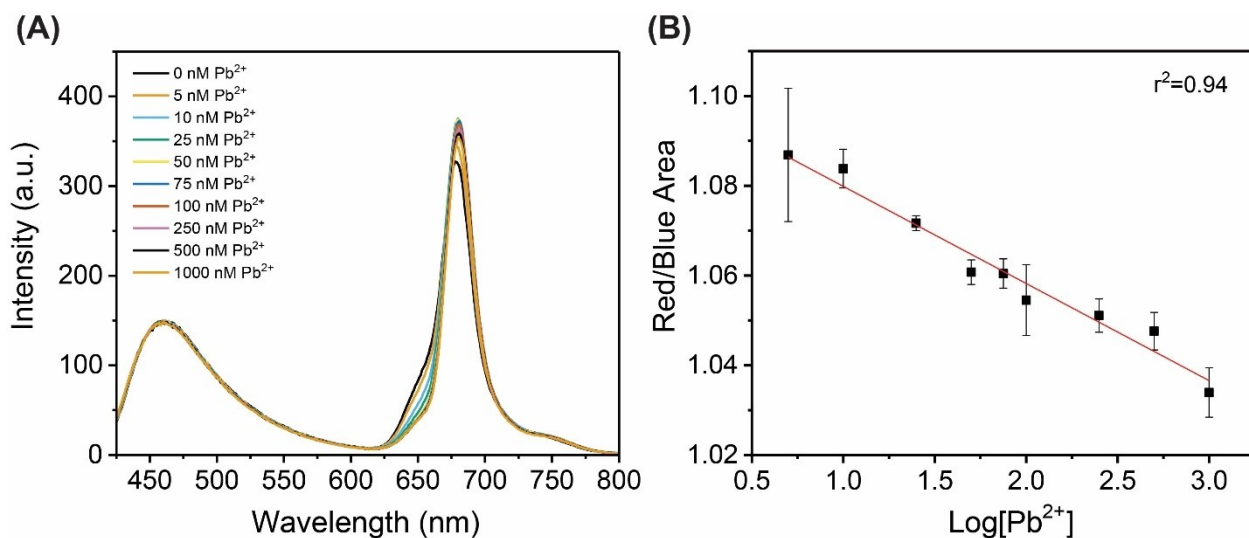


**Figure 30:** (A) Fluorescence spectra of a solution of 35  $\mu\text{g/mL}$  of FG-CDs in the presence of increasing concentrations of lead (II) ions (B) Linear trend of the decreasing fluorescence area ratio for FG-CDs showing poor linearity.

This optimization step allowed us to select the lowest metal cation concentration at 50 nM to avoid challenges associated with curve linearity and reproducibility. Therefore, to ensure that the detection was performed both accurately and at environmentally relevant concentrations, the concentration ranges of the metal cations selected for further experimentation were set as follows: 0, 50, 100, 250, 400, 550, 700, 850, and 1000 nM. Moreover, with proof that successful detection of metal cations below 1  $\mu\text{M}$  concentrations is possible, dual-fluorescent FG-CDs were used for the remainder of the optimization and quenching experiments at concentrations of 21-35  $\mu\text{g/mL}$ .

#### 4.3.5. Water vs. Buffer

During the optimization process, it was hypothesized that pH may play an important role in metal quenching. As such, we investigated the need for a buffer system to maintain a stable pH environment. However, a great number of buffers (such as EDTA, PBS, TrisHCl, etc.) are known to bind strongly with metals, affecting the pH and forming insoluble metal complexes.<sup>129, 130</sup> Figure 31 shows a quenching assay performed with 30  $\mu\text{g/mL}$  of FGCDs in PBS buffer, a good metal complexing agent, where no significant quenching is observed upon the addition of mercury (II)

ions. The plot in Figure 31B shows a decreasing trend in the R/B ratio as a function of increasing metal concentration with poor linearity.

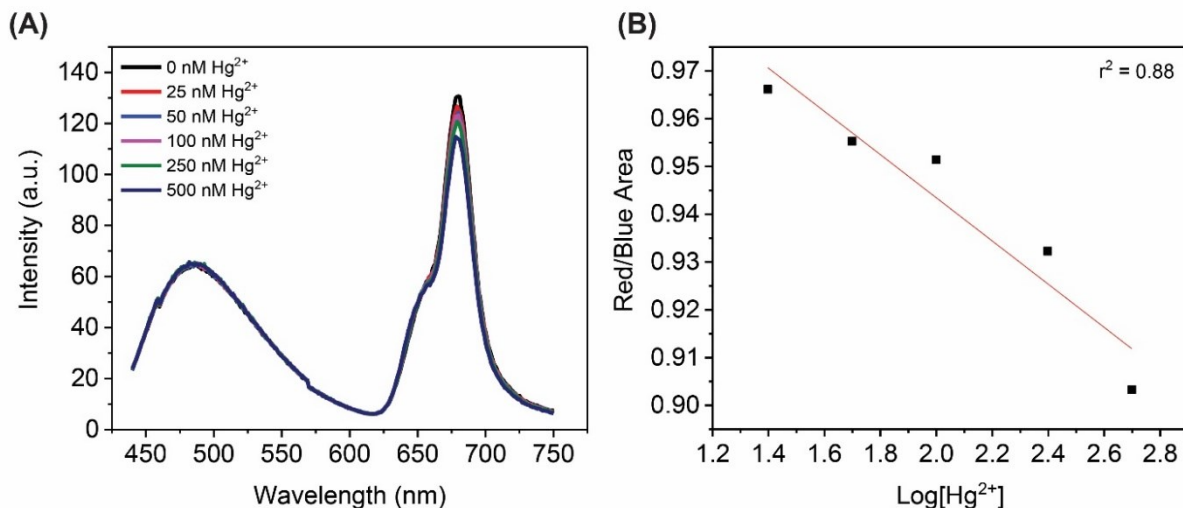


**Figure 31:** (A) Fluorescence spectra of 30  $\mu\text{g/mL}$  of FG-CDs in PBS buffer with increasing concentrations of  $\text{Hg}^{2+}$  (B) Plotted R/B ratio of FG-CDs as a function of metal concentration, showing a decreasing and poorly linear trend.

Further studies tracking pH changes during quenching assays revealed no significant changes in pH values with the addition of the metal salt solution to the CD dispersion. As such, no buffering of the solution was required. In addition, keeping in mind the long-term goal of the project, the primary use of these CDs would be for in-situ analysis of natural water samples (tap water, river water, lake water, etc.). Therefore, the system should be optimized for use in water without the presence of a buffer. For these reasons, quenching assays with FG-CDs were performed in water for the remainder of the project.

#### 4.3.6. Water Contamination

Having optimized the conditions for metal quenching assays, testing continued with FG-CDs. However, we noted periodic inconsistencies in the quenching assays. Previous experiments using FG-CDs in our research group<sup>96</sup> showed promising results for metal quenching, including a possibility of tracking metal concentrations through changes to the absorbance spectra of the metal-

CD complexes. Figure 32A shows the appearance of a peak at  $\sim 475$  nm in the absorbance spectrum of FG-CDs with the addition of lead (II) ions.<sup>96</sup> In contrast, Figure 32B shows the same experiment repeated, without the appearance of this peak. A number of variables, such as CD batch, pH, and age of the metal solution were explored to determine the origin of this variability. Ultimately, it was found that the MilliQ water, produced in-house, had eventually become contaminated with metal cations overtime, resulting in the observed variabilities. To confirm this observation, commercial LC-MS water was used to replicate the experiments showing once more the appearance of a peak  $\sim 475$  nm in Figure 32C. The contamination observed had resulted in a diminishing of the quenching response in the absorbance and fluorescence spectra and also resulted in the absence of peaks related to the formation of metal-CD complexes. This is

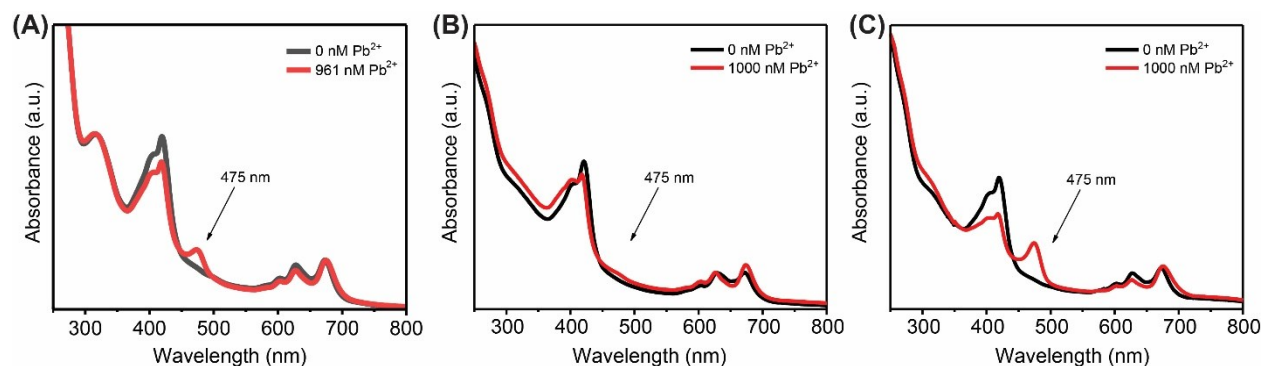


**Figure 32:** Absorbance spectrum for FG-CDs with the addition of  $\sim 1000$  nM  $\text{Pb}^{2+}$  (A) Previously obtained data, showing a peak at 475 nm associated with the lead-CD complex<sup>96</sup> (B) repeated in contaminated MilliQ water showing only a very small peak at 475 nm (C) repeated in LC-MS water, free of metal contaminants, showing a strong peak at 475 nm.

ascribed to the fact that as the CDs were already saturated with metallic cations and thus could not interact with the additional cations used in the quenching assays.

The remainder of the quenching experiments presented below were conducted solely using LC-MS water, as well as using rigorous glassware cleaning protocols to minimize potential sources of metal contamination.

### 4.3.7. Water Dilution Effects

The last control experiment performed focused on the effect of dilution upon addition of the metal cation solution throughout the quenching assays. Initially, this effect was thought to be negligible due to the small change in volume upon the addition of metal solution (1% total volume change as a result of the addition of a total of 80  $\mu\text{L}$  of metal solution into 8 mL of the CD dispersion). However, when a control quenching assay was performed using only LC-MS water instead of a metal solution, some changes were observed in the fluorescence spectra (Figure 33A). More notably, upon measuring the R/B ratio as a function of added water volume, a decreasing trend in Figure 33B was observed up until a 10% decrease in the total R/B ratio value. In the case where only a dilution effect was observed, it would be expected that both peaks would diminish in

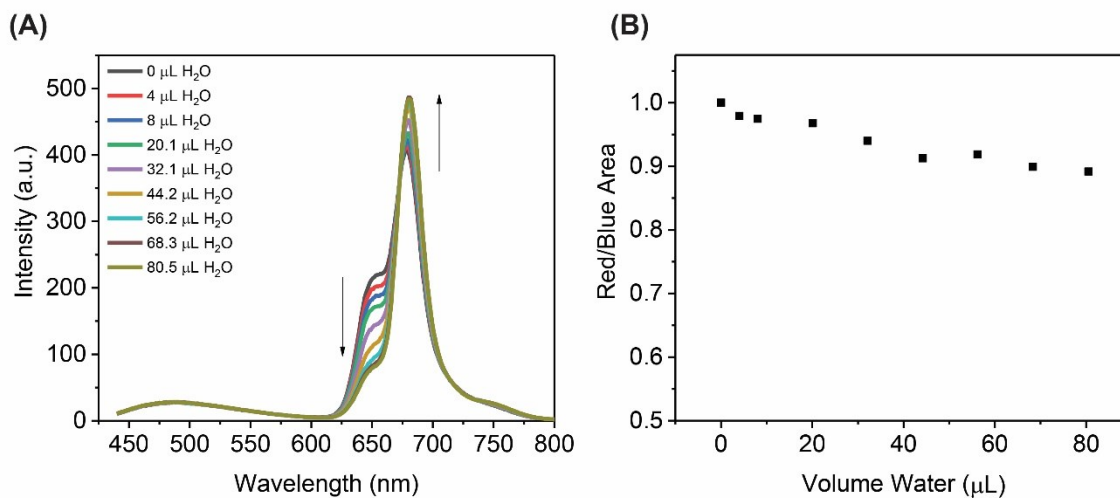


**Figure 33:** A dilution control experiment with water was performed on 35  $\mu\text{g}/\text{mL}$  FG-CDs showing (A) fluorescence spectra with a significant changes as a function of volume of water added and (B) the corresponding R/B ratio plot showing a decreasing trend down to 90% of the original R/B ratio value.

intensity but that the R/B ratio would remain unchanged as only a concentration change was occurring. However, changes in the R/B value indicate an effect where the surface emission (the red emission) is more strongly affected than the core emission (blue emission). It is known that LC-MS water contains trace metal contaminants, thus quenching by these contaminants may be

the cause of the decrease in red emission. As such, the water itself with its trace metal contamination must be accounted for in quenching assays. It should also be noted that while significant changes were noticed in the fluorescence spectra, only comparatively small changes in intensities were observed in the absorbance spectrum for the water control experiment in Figure 34. To correct for the water's effect, that is the quenching caused by trace-metal contamination upon addition of water separate from the quenching caused by the addition of a known concentration of metal in that same water, the values from the plot in Figure 33B were used. Here, at each step in the addition of solution, the decrease in the R/B value from the original value is used as a correction factor. Therefore, each R/B ratio value, at each point in the quenching assay, is multiplied by its corresponding dilution factor from the water control experiment. This results

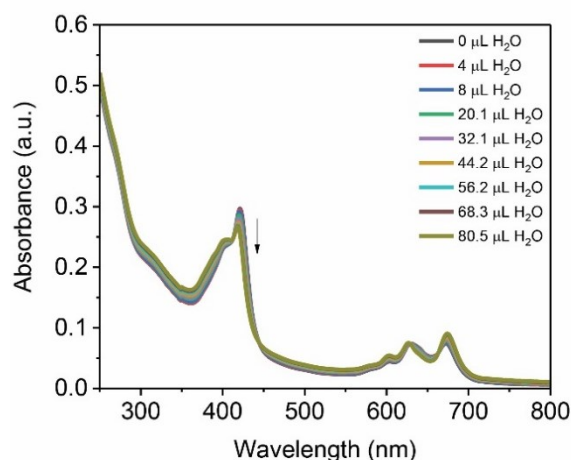


**Figure 34:** Absorbance spectra for dilution control experiment with water performed on 35  $\mu\text{g/mL}$  FG-CDs.

in the correction of a downward trend in the R/B ratio values wrongfully attributed to quenching by the known concentration of metals in the quenching assay. Figure 35 shows an example of a correction with results from a quenching assay using chromium (III) ions. Here, a downward trend is observed in Figure 35A before water dilution corrections up to the higher concentrations where the R/B plateaus. In Figure 35B, the same plot is shown after water dilution correction and the

decreasing trend disappears. This correction is therefore crucial for differentiating systems

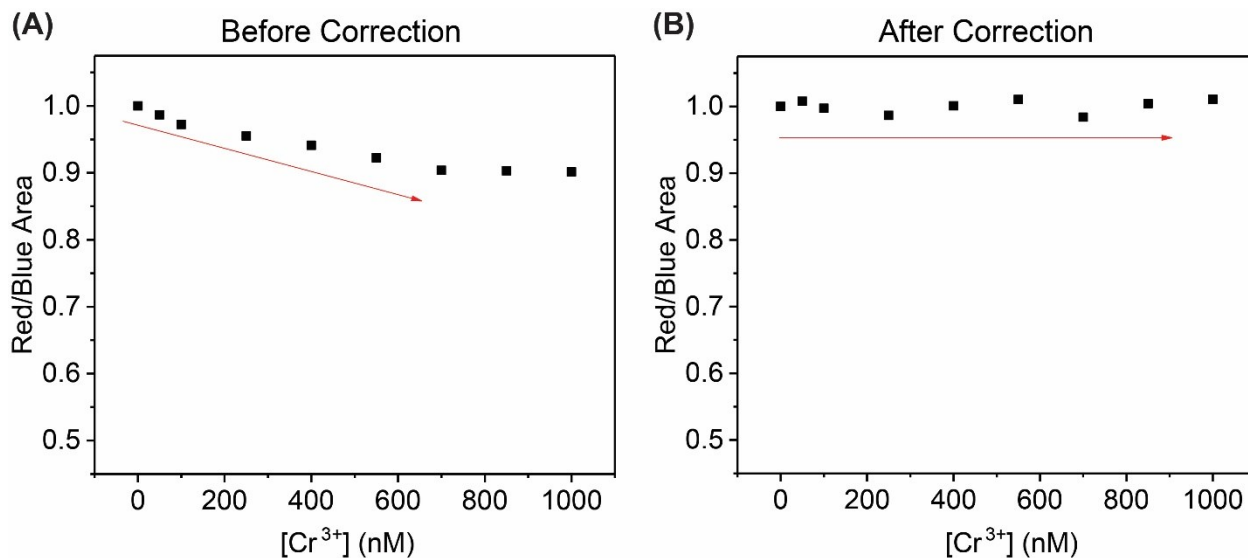


**Figure 35:** Plots showing R/B ratio as a function of metal concentration (A) before and (B) after water dilution correction.

where trace metal contaminants may be quenching the system, but where no additional quenching is observed for a known concentration of a specific metal ion being tested. In essence, the inclusion of this correction factor clearly demonstrate whether a particular metal cation can induce quenching in a CD system, or whether the observed quenching is an artefact.

#### 4.3.8. Quenching Assay Results

With the optimization efforts completed, the selected metal cations were tested with FG-CDs to determine differences in quenching behaviour. Changes in the CDs' fluorescence and absorbance spectra were tracked as a function of increasing metal concentration.

##### 4.3.8.1. Mercury Assay

The first assay was performed with mercury (II) ions from a mercury (II) chloride solution. The results in Figure 36A show the absorbance spectra taken for the FG-CD system at various concentrations of mercury (II) ions. Most notably, there is the appearance of a new peak at ~450 nm, which is exclusively observed with the CD-mercury complex. This peak will be discussed

further in the section relating to quenching mechanisms. Moreover, the peak at 420 nm, the same wavelength used for excitation in fluorescence spectra, shows a gradual decrease in intensity as metal concentrations increase. This correlates with an overall decrease in fluorescence intensity in Figure 36B and C, which show the fluorescence spectra of FG-CDs and the plot of the overall fluorescence R/B area ratio, respectively. It should be noted that although there is a decrease in the 650 nm shoulder peak in the fluorescence spectra, the main peak at 680 nm actually increases in intensity as metal concentration increases, up to a concentration of 250 nM, where it proceeds to decrease once more. This could be due to a transfer of energy, which occurs as a result of the quenching of the 650 nm emissive state at low  $\text{Hg}^{2+}$  concentrations and is then followed by

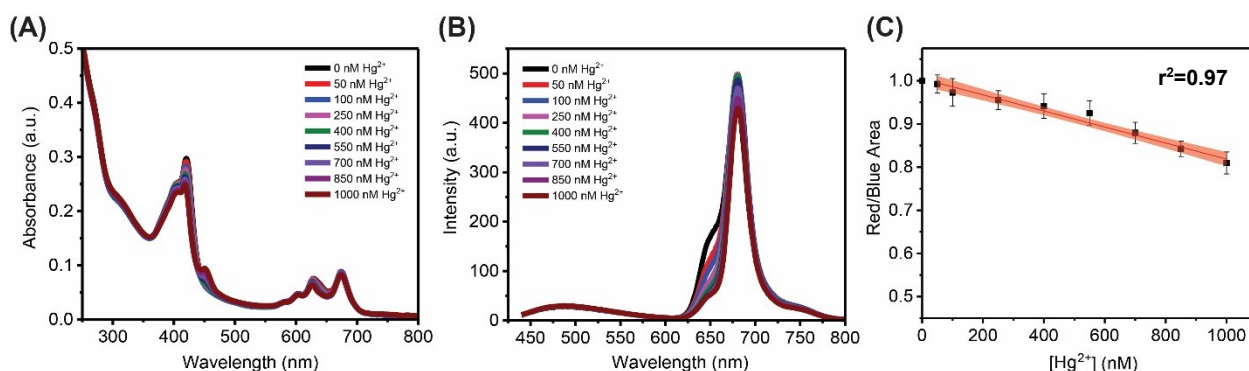


**Figure 36:** Results of a FG-CD quenching assay with mercury (II) ions showing (A) the absorbance spectrum with a decrease in the 420 nm peak and the appearance of a new peak at  $\sim 450$  nm related to the CD and mercury complex, (B) the fluorescence spectra showing changes in the 650 and 680 nm peak while the 485 nm peak remains unaffected by the presence of metal cations (C) the linear plot of the decreasing overall R/B area ratio with an  $r^2=0.97$ .

quenching of the 680 nm peak at higher concentrations thereafter. However, as seen by the plotted R/B area ratio, the overall R/B ratio decreases with increasing  $\text{Hg}^{2+}$  ions. The plot shows a decreasing linear trend with an  $r^2 = 0.97$ , where the R/B ratio decreases down to 80% of its initial value after the addition of 1000 nM of  $\text{Hg}^{2+}$ . The LOD was then calculated using the standard  $3\sigma$  error divided by the slope of the linear trend. The LOD was found to be equal to  $\sim 104$  nM (28 ppb). This is an encouraging result, as this shows that the LOD of our system corresponds to

concentrations that have previously been found in polluted Canadian waters, such as the Great Lakes.<sup>18</sup> This also shows the applicability of this CD metal sensor even with such preliminary results, where the CD system has not yet been fully optimized.

#### 4.3.8.2. Lead Assay

Next, quenching assays were performed with lead (II) chloride. Similarly, Figure 37A shows the absorbance spectra taken for the FG-CD system at various concentrations of lead (II) ions. Once more, a new peak appeared, however this time it was located at  $\sim 475$  nm. This peak was only observed following the formation of the CD-lead complex. We note the same decrease in the 420 nm absorbance peak, as well as the same increase and subsequent decrease in 680 nm fluorescence emission in Figure 37B with increasing metal concentration. Once more, the overall

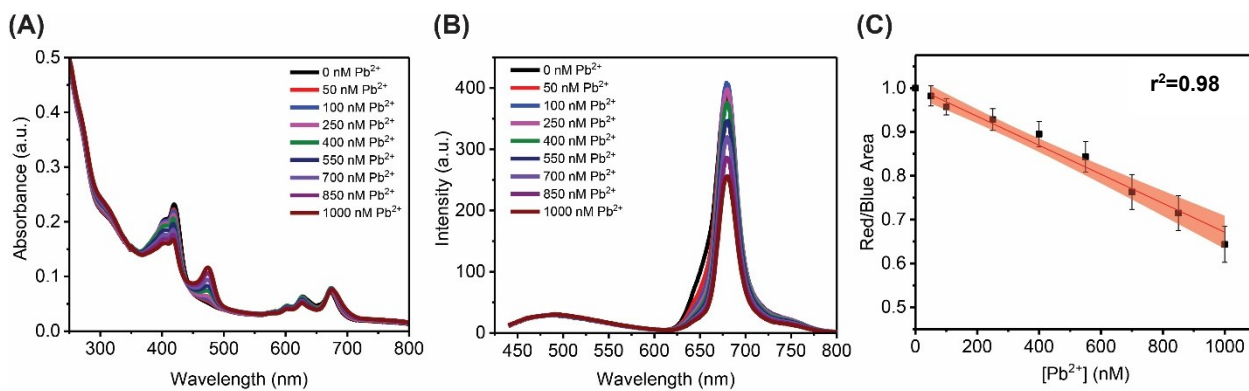


**Figure 37:** Results of a FG-CD quenching assay with lead (II) ions showing (A) the absorbance spectrum with a decrease in the 420 nm peak and the appearance of a new peak at  $\sim 475$  nm related to the CD and lead complex, (B) the fluorescence spectra showing changes in the 650 and 680 nm peak while the 485 nm peak remains unaffected by the presence of metal cations (C) the linear plot of the decreasing overall R/B area ratio with an  $r^2=0.98$ .

R/B area ratio plotted in Figure 37C shows a constant decrease in value regardless of the small increases seen in the 680 nm peak at the beginning of the quenching assay. The R/B area ratio plot shows another decreasing linear trend, however the linearity is slightly improved with an  $r^2 = 0.98$ . The Pb<sup>2+</sup> ions show significantly more quenching than the Hg<sup>2+</sup> ions, with the R/B ratio dropping down to  $\sim 63\%$  of its original value at a concentration of 1000 nM of Pb<sup>2+</sup>. The calculated LOD

was also lower at 81 nM (22 ppb). Once more the LOD for lead (II) ions with our CD metal sensor was within a reasonable concentration for its use in environmental waters in Canada. The safe limit set by the government for lead concentrations in drinking water in Quebec is of 5 ppb<sup>18</sup>, somewhat below our LOD. However, actual lead concentrations in drinking water in Quebec are found to be on average about 10 ppb, with this limit being surpassed at least 118 times from 2010-2014 with concentrations reaching up to 97 ppb, well above both the safe drinking limit and the LOD of our system.<sup>131</sup> With proper optimization of our CD system, lower LODs may be achieved to allow for detection of lead concentrations similar or below the maximum safe drinking water concentration set by Health Canada.

#### 4.3.8.3. Chromium, Cobalt, Copper, Nickel, Iron, Gadolinium & Dysprosium

Seven other metal cations were tested in quenching assays. However, no significant quenching was observed for any of these metals. The changes in the R/B area ratio following the addition of 1000 nM of a metal cation can be observed in Figure 38. In this plot, the R/B ratio

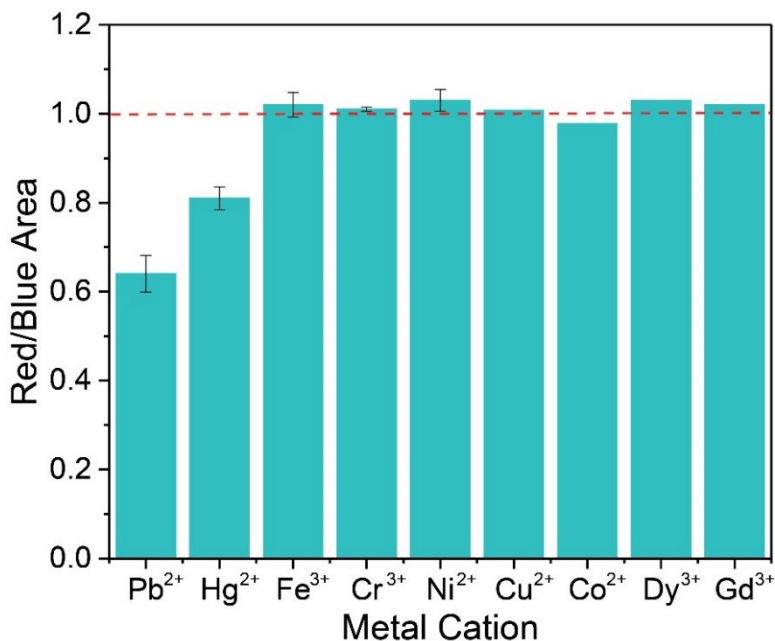


**Figure 38:** R/B area ratio of FG-CDs with 1000 nM of various metallic cations showing comparison of quenching effectiveness.

fluctuates around its initial value of 1 for the seven metal cations. Conversely, the R/B area ratio for  $\text{Pb}^{2+}$  is the lowest at  $\sim 63\%$  of its initial value, followed by  $\text{Hg}^{2+}$  at  $\sim 80\%$  of its initial value.

Figure 39 shows a representative quenching assay of FG-CDs with Iron (III) ions with results similar to those from all quenching assays that did not result in quenching. In Figure 39A, the absorbance spectrum shows a slight decrease in the 420 nm peak, a decrease which is much less pronounced than that shown in the quenching assays with  $\text{Pb}^{2+}$  and  $\text{Hg}^{2+}$ . This change in

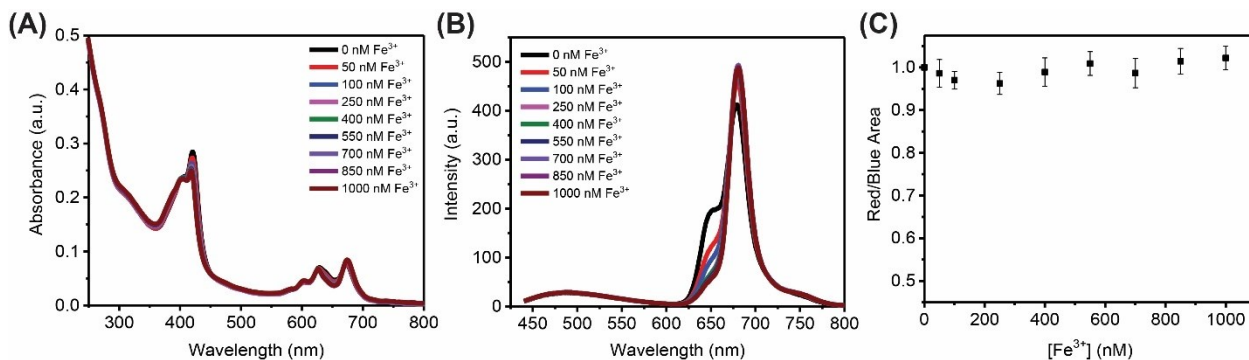


**Figure 39:** Results of a FG-CD quenching assay with iron (III) ions showing (A) the absorbance spectrum with a smaller decrease in the 420 nm peak than the metal quenching assays performed with lead (II) and mercury (II) ions (B) the fluorescence spectra showing changes in the 650 and 680 nm peak while the 485 nm peak remains unaffected by the presence of metal cations (C) the R/B area ratio showing fluctuations in R/B area ratio values without a significant trend.

absorbance spectrum is much more similar to those from the water control assay in Figure 34, which supports the idea that all changes are related to the addition of water containing trace metal contaminants. Similar to the first two quenching assays presented, initially, the fluorescence spectrum in Figure 39B shows an increase in the 680 nm peak with a simultaneous decrease in the 650 nm peak. However, here the similarities end, as the 680 nm peak does not subsequently decrease in intensity, but remains unchanged for the remainder of the quenching assay. This could be an indication that the initial 650 nm quenching and energy transfer causing an increase of the 680 nm peak intensity is due to trace metals within the LC-MS water used for the iron solution and that the absence of additional higher concentrations of metal ions prevented subsequent quenching

of the 680 nm peak. As the contribution of trace metal contaminants in the water is accounted for, the plot of the R/B area ratio in Figure 39C, shows no decreasing trend. Only slight fluctuations in the R/B area ratio values are observed with increasing metal concentration. Thus confirming that no fluorescence quenching is occurring. Chromium, Cobalt, Copper, Nickel, Gadolinium & Dysprosium all show similar behaviour. The results for these quenching assays can be found in Figures A8-10 of the Appendix.

#### 4.4. Quenching Mechanism

Following completion of the metal quenching assays, the quenching mechanism(s) was investigated. Firstly, data was extracted from the absorbance spectra collected during the quenching assays. Subsequently, fluorescence lifetime measurements were collected and examined for both the lead (II) and mercury (II) ion quenching assays. Finally, temperature studies were performed to confirm the quenching mechanism.

##### 4.4.1. Absorbance Spectra

It can be recalled from Chapter 1 that the absorbance spectra of CDs (the fluorophores) in the presence of metallic cations (the quenchers) can provide evidence as to the type of quenching occurring. In a statically quenched system, changes in the absorbance spectra related to the formation of a new CD-metal ion complex with its own unique absorbance band can be observed

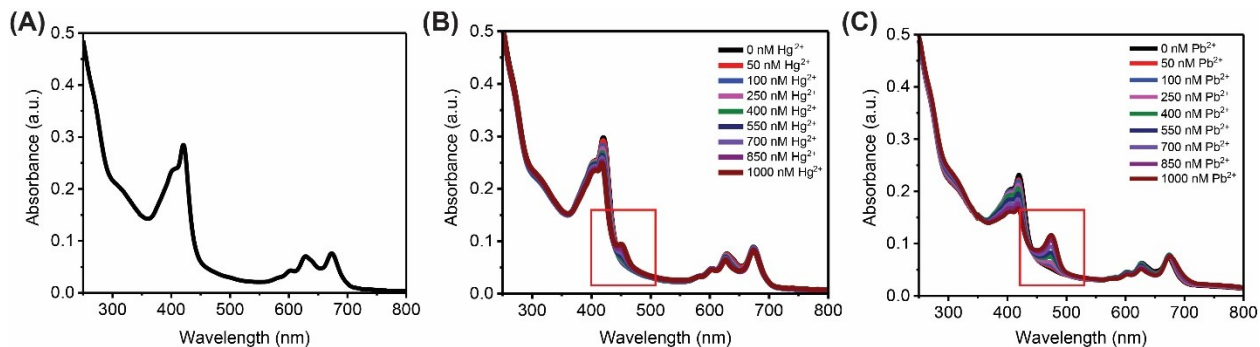


**Figure 40:** Absorbance spectra for FG-CDs (A) alone, (B) showing a new peak at ~450 nm in the presence of Hg<sup>2+</sup>, and (C) at ~475 nm in the presence of Pb<sup>2+</sup>.

with increasing concentrations of metal cations. However, in a dynamically quenched system, no such changes are observed.<sup>53, 54</sup> With this knowledge, the absorbance spectra of FGCDs in the presence of  $\text{Hg}^{2+}$  and  $\text{Pb}^{2+}$  were examined to seek evidence of the type of quenching mechanism taking place. Figure 40 shows the absorbance spectra of the carbon dots alone, in the presence of mercury (II) ions and in the presence of lead (II) ions, respectively. We note in Figure 40B and C the appearance of new peaks at  $\sim 450$  and  $475$  nm, related to the formation of new CD-mercury and CD-lead complexes, respectively. Therefore, the changes in the absorbance spectra indicate that a static quenching mechanism is likely occurring for this CD system with these two metal cations.

#### 4.4.2. Fluorescence Lifetimes

Fluorescence lifetime measurements are also an important tool for identifying the quenching mechanism at play in a given system. Recalling Chapter 1, in the presence of a quencher (in this case the metal cations) statically quenched systems do not show any changes in fluorescence lifetimes. However, dynamically quenched systems exhibit changes in fluorescence lifetimes as a function of metal concentration.<sup>53, 54</sup> Therefore, fluorescence lifetime measurements were obtained for FG-CDs in the presence of lead (II) and mercury (II) ions. Table 7 summarizes

**Table 7:** Fluorescence lifetimes of FG-CDs at various concentrations of mercury (II) ions.

<b>[Hg<sup>2+</sup>]</b>	<b>Lifetime 1 (ns)</b>	<b>+/-</b>	<b>Lifetime 2 (ns)</b>	<b>+/-</b>	<b><math>\chi^2</math></b>
0 nM	0.4	2.9E-03	5.5	1.1E-02	1.09
400 nM	0.4	1.1E-02	5.5	2.2E-02	1.33
1000 nM	0.4	7.1E-03	5.6	2.3E-02	1.11
<b>Average:</b>	<b>0.4 ns</b>		<b>5.6 ns</b>		

the results of the CD lifetimes, in the presence of mercury (II) ions, which evidence two components. A short component of 0.4 ns and a long component of 5.6 ns. These two lifetimes remain unchanged regardless of mercury (II) concentration. This further supports the idea that a static quenching mechanism is occurring.

Similarly, two lifetime components, displayed in Table 8, are found when measuring FG-CDs with and without lead (II) ions. The values of the lifetime components in the absence of any metal ions are of 0.8 ns and 5.8 ns. When lead (II) ions are introduced to the system, no significant changes are perceived for the two components. Once more, evidence of a static quenching mechanism is clearly observed.

**Table 8:** Fluorescence lifetimes of FG-CDs at various concentrations of lead (II) ions.

<b>[Pb<sup>2+</sup>]</b>	<b>Lifetime 1 (ns)</b>	<b>+/-</b>	<b>Lifetime 2 (ns)</b>	<b>+/-</b>	<b>χ<sup>2</sup></b>
0 nM	0.8	2.8E-03	5.7	4.5E-03	1.17
400 nM	0.8	4.1E-03	5.9	8.1E-03	1.07
1000 nM	0.8	3.3E-02	5.7	3.5E-02	1.14
<b>Average:</b>	<b>0.8 ns</b>		<b>5.8 ns</b>		

#### 4.4.3. Temperature Studies

Finally, temperature studies were also performed to confirm the prior findings. As previously mentioned, the two quenching mechanisms display opposite trends with temperature changes. In the case of a temperature increase, the statically quenched system undergoes destabilization of the formed complex between the CD and metal ion with this increased energy within the system. In this case, the complexes are more likely to break apart, thus reducing the

observed quenching; and fluorescence is recovered in the system. However, in dynamically quenched systems, the increase in temperature results in increased particle movement, thus causing a higher probability of collisions between the CDs and the metal cations. Since quenching is a result of an energy transfer between the CD and the metal cations at the time of collision, additional fluorescence quenching would be observed at higher temperatures.<sup>53, 54</sup>

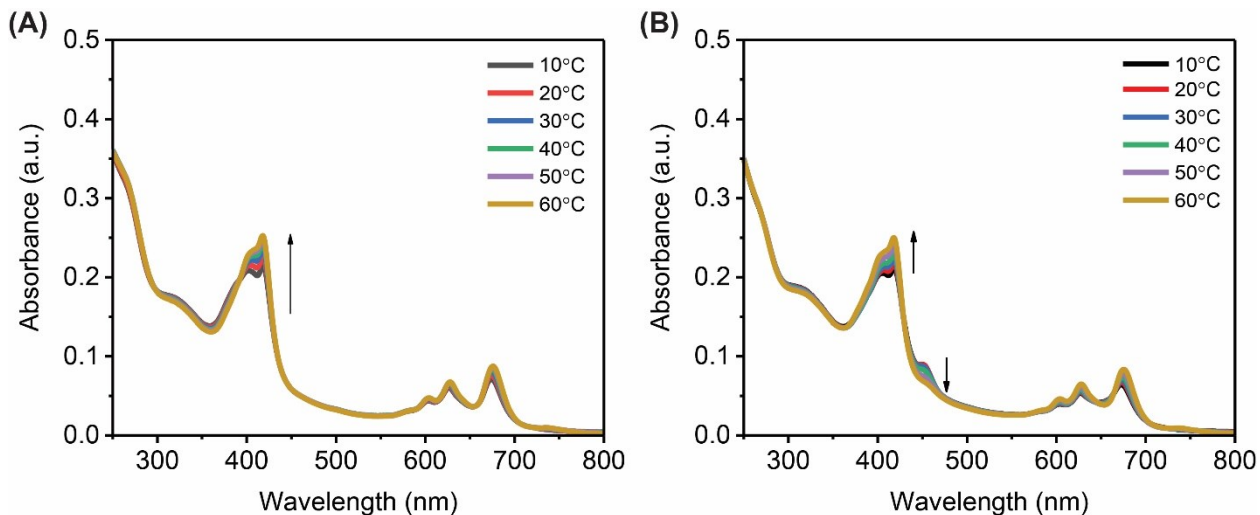


**Figure 41:** Absorbance spectra of FG-CDs showing changes as a function of increasing temperatures (A) with 0 nM of Hg<sup>2+</sup> (B) with 1000 nM of Hg<sup>2+</sup>.

As both the absorbance spectra and fluorescence lifetimes are typically sufficient in confirming which quenching mechanism is occurring, temperature studies were only performed on one of the systems as a proof of concept. The absorbance spectra of the FG-CDs were taken at increasing temperatures both with and without the presence of 1000 nM Hg<sup>2+</sup>. Figure 41 shows the changes in both of these spectra as a function of temperature. It can be seen that the control FG-CDs, in the absence of the metal cations, display an increase in the 420 nm peak as a function of temperature. This correlates with the enhancement of the red fluorescence emission reported for these CDs at increasing temperatures.<sup>66</sup> We postulate that this could be due to Förster resonance energy transfer (FRET) pathways within the sample which are promoted at higher temperatures.<sup>132,</sup>  
<sup>133</sup> FG-CDs meet the spectral overlap requirements of FRET, wherein there is an overlap of their

absorbance and emission spectra in several regions.<sup>54, 132</sup> Increased particle movement and collisions due to higher temperatures may help the system meet the 1-10 nm distance requirement of FRET.<sup>54, 134</sup> These energy transfers typically flow from higher to lower energy states, thus promoting red fluorescence over blue fluorescence.

However, more notably, one change occurs in the system in the presence of mercury ions. The 450 nm peak associated with the CD-mercury complex in Figure 41B decreases in intensity with increasing temperature. This indicates the de-stabilization and the breaking apart of the formed complex at higher temperatures, which results in the loss of its absorbance peak. As such, it can be concluded that a static quenching mechanism is indeed occurring with these CDs.

#### 4.5. The Root of Metal-CD Interactions

Finally, although we understand that a complex is being formed between the CDs and the metal cations, it is important to determine how and why this formation takes place. This understanding can help direct application development and aid in the design of CDs with lower LODs. The metal cations tested were selected for their unique set of characteristics, which allowed

**Table 9:** Classification of various ions based on the HSAB theory. Table adapted from: EPA<sup>138</sup>

HSAB Classification	Ions
<b>Hard acids</b>	Al <sup>3+</sup> , Ba <sup>2+</sup> , Be <sup>2+</sup> , Co <sup>3+</sup> , Cr <sup>3+</sup> , Fe <sup>3+</sup> , Mn <sup>2+</sup> , Sr <sup>2+</sup> , U <sup>4+</sup> , UO <sub>2</sub> <sup>2+</sup> , VO <sup>2+</sup>
<b>Borderline acids (between hard and soft)</b>	Co <sup>2+</sup> , Cu <sup>2+</sup> , Fe <sup>2+</sup> , Ni <sup>2+</sup> , Pb <sup>2+</sup> , Zn <sup>2+</sup>
<b>Soft acids</b>	Ag <sup>+</sup> , Cd <sup>2+</sup> , Cu <sup>+</sup> , Hg <sup>2+</sup> , Hg <sup>+</sup> , CH <sub>3</sub> Hg <sup>+</sup> , Tl <sup>3+</sup> , Tl <sup>+</sup>
<b>Hard bases</b>	F <sup>-</sup> , H <sub>2</sub> O, oxyanions: OH <sup>-</sup> , SO <sub>4</sub> <sup>2-</sup> , CO <sub>3</sub> <sup>2-</sup> , HCO <sub>3</sub> <sup>-</sup> , C <sub>2</sub> O <sub>4</sub> <sup>2-</sup> , CrO <sub>4</sub> <sup>2-</sup> , MoO <sub>4</sub> <sup>2-</sup> , H <sub>n</sub> PO <sub>4</sub> <sup>n-</sup> , H <sub>n</sub> AsO <sub>4</sub> <sup>n-3</sup> , SeO <sub>4</sub> <sup>2-</sup> , H <sub>2</sub> VO <sub>4</sub> <sup>-</sup> , NH <sub>3</sub> ,

	RNH <sub>2</sub> , N <sub>2</sub> H <sub>4</sub> , ROH, RO, R <sub>2</sub> O, CH <sub>3</sub> COO <sup>-</sup> , etc.
<b>Borderline bases (between hard and soft)</b>	Cl <sup>-</sup> , Br <sup>-</sup> , NO <sub>2</sub> <sup>-</sup> , SO <sub>3</sub> <sup>2-</sup> , H <sub>n</sub> AsO <sub>3</sub> <sup>n-3</sup> , C <sub>6</sub> H <sub>5</sub> NH <sub>2</sub> , C <sub>5</sub> H <sub>5</sub> N, N <sub>3</sub> <sup>-</sup> , N <sub>2</sub>
<b>Soft bases</b>	I <sup>-</sup> , HS <sup>-</sup> , S <sup>2-</sup> , CN <sup>-</sup> , SCN <sup>-</sup> , Se <sup>2-</sup> , S <sub>2</sub> O <sub>3</sub> <sup>2-</sup> , - SH, -SCH <sub>3</sub> , NH <sub>2</sub> , R <sup>-</sup> , C <sub>2</sub> H <sub>4</sub> , C <sub>6</sub> H <sub>6</sub> , RNC, CO, R <sub>3</sub> P, (RO) <sub>3</sub> P, R <sub>3</sub> As, R <sub>2</sub> S, RSH, RS

---

us to examine changes in quenching behaviour based on a select number of properties. Lead and mercury in particular were selected due to their significantly larger ionic radii; and these were the only two metals to show quenching of the CD fluorescence. Therefore, a closer examination of these metals and the differences in their properties compared to all other tested metals was necessary. It has long been known that lead and mercury have particularly strong interactions with sulfur-containing compounds.<sup>135-137</sup> This can be reasoned through the Hard-and-Soft Acid-Base (HSAB) theory. A hard ion is described as one with a low polarizability, a large charge density and a small ionic radius; these ions tend to form ionic type bonds. Conversely, a soft ion is one with a high polarizability, a small charge density and a large ionic radius; these ions tend to form covalent type bonds. A list of metal cations and their classification can be seen in Table 9, which was adapted from the EPA's Framework for Metals Risk Assessment.<sup>138</sup>

It is known that soft and borderline acids, such as mercury and lead (respectively), bind more strongly with soft bases, such as thiols, which are present on the FG-CD surface.<sup>138-140</sup> Lead in particular is shown to have an especially strong affinity to soft, sulfur-containing ligands compared to a number of other soft and borderline acids.<sup>138</sup> This can explain why lead (II) and mercury (II) ions readily bind to thiols on the CD surface. However, since other tested metals are also considered soft and borderline acids, this does not explain their inability to bind and quench

**Table 10:** Charge, ionic radii and charge densities of tested metal cations. Table adapted from: Rayner-Canham<sup>127</sup>

<b>Metal Ion</b>	<b>Charge</b>	<b>Ionic Radius (Å)</b>	<b>Charge Density (C mm<sup>-1</sup>)</b>
<b>Fe<sup>3+</sup></b>	3+	0.785	232
<b>Pb<sup>2+</sup></b>	2+	1.19	32
<b>Cu<sup>2+</sup></b>	2+	0.87	116
<b>Co<sup>2+</sup></b>	2+	0.88	108
<b>Hg<sup>2+</sup></b>	2+	1.02	49
<b>Ni<sup>2+</sup></b>	2+	0.83	134
<b>Cr<sup>3+</sup></b>	3+	0.52	261
<b>Gd<sup>3+</sup></b>	3+	0.938	91
<b>Dy<sup>3+</sup></b>	3+	0.912	99

FG-CD fluorescence. For this, an in-depth study of the properties of the selected metal cations is required. Table 10 displays the charge densities of the metal cations tested during quenching assays. It is quickly remarked that Pb<sup>2+</sup> and Hg<sup>2+</sup> clearly possess the lowest charge densities among all the metals tested.<sup>127</sup> As such, it seems that their lower charge densities play an important role in their ability to bind and quench FG-CDs. This can be explained by repulsion occurring between the CDs and metal ions. The FG-CDs are known to have both positively and negatively charged surface functional groups, causing a repulsion with the positively charged metal cations that have a larger charge density. It is possible that the charge densities of mercury (II) and lead (II) ions may be low enough to avoid repulsion with the positively charged surface functional groups of the FG-CDs. Thus, they are still able to bind with the negatively charged surface thiols and cause quenching of the FG-CDs. Consequently, we have provided explanations and supporting evidence for the quenching mechanism and the functional groups responsible for causing the quenching of FG-CDs.

## Chapter 5. Conclusion & Future Works

With growing concerns over the environmental and health impacts of metal contamination, this project aimed to further our knowledge of metal-CD interactions to give researchers the necessary understanding to design more sensitive metal sensing CD systems. For this purpose, steady-state and dynamic optical characterization techniques were used to elucidate the quenching mechanism occurring and the functional groups responsible for this phenomenon. As a result, surface functional groups on the CDs were altered using various precursors to better understand how these changes affect metal-CD interactions. In addition to the synthesis, the purification procedure of these CDs was also optimized to allow for the study of the inherent CD properties. It was found that similar CD systems, prepared from the same precursors have vastly different purification needs. Overlooking these differences can lead to ambiguity and variability in CD properties, including their ability to detect metal ions. Therefore, purification procedures need to be tailored to each CD system by observing changes in physical and optical properties throughout their purification to determine the efficiency of each method.

With proper purification protocols established, the sensing capabilities of CDs can be explored. Although several CD systems were found to be capable of detecting metal cations at varying concentrations, the most sensitive dots were dual-fluorescent in nature and could be used in a ratiometric sensing approach. These dots could be used to detect both lead and mercury cations with LODs of 22 and 28 ppb, respectively. In the case of mercury ions, this concentration is comparable to those of mercury ions found in natural waters found in Canada, thus showing potential future applicability of this system in natural waters.<sup>18</sup> Future optimization could further lower these detection limits, thus expanding this system's applicability to a wider array of metal cations. Quenching of FG-CDs, in the presence of both lead and mercury, was determined to occur

through a static mechanism as evidenced by steady-state and dynamic optical characterization techniques. It was further theorized that the metal-CD interaction stems from the electrostatic attraction of the positively charged metal cations and the negatively charged thiols on the surface of the CD, as lead and mercury are known to be strongly attracted to sulfur containing compounds.<sup>135-137</sup> Moreover, the selectivity observed (wherein FG-CDs only detect mercury and lead out of a number of various metal cations) is seemingly due to the lower charge density of these two metals in comparison to all other cations tested.<sup>127</sup> The presence of positively charged functional groups on the CD surface may be causing significant repulsion with metallic cations possessing larger charge densities.

This work is only the first step in understanding metal-CD interactions. Therefore, a number of future works are proposed to further this understanding. First, to support the hypothesis that only low charge density metal cations can be detected with these CDs, future work should investigate a number of other metal cations with low charge densities including  $K^+$ ,  $Li^+$ ,  $Na^+$  and  $Ba^{2+}$ . Another experiment to support this same claim would be to perform quenching assays at different pH values. Due to the possible repulsion caused by positively charge surface functional groups, the effect of protonating and deprotonating the CD surface on metal sensing should be investigated. As mentioned above, further optimization of these CDs could lead to lower detection limits. Experiments that could help in achieving this include optimizing the thiol concentration on the CD surface, as well as the addition or removal of other functional groups such as amines (which could cause electrostatic repulsion) and carboxylic acids (which may play a role in detection as well). As signature absorbance peaks are observed due to static quenching, the potential for multiplex sensing should be tested.

Finally, to determine how well this system may perform in various environments, it is important to attempt metal sensing in natural water samples, which contain a more complex matrix as well as possible interfering species. Although our systems have proven efficient in binding free metal cations in water, metal cations found in natural waters are often chelated by dissolved organic matter (DOM). Binding efficiencies may vary greatly depending on the nature of the molecules making up the DOM, however, in some cases, this binding may be strong enough to hinder any interaction with our CD system, thus leaving these metals undetected.<sup>141, 142</sup> Detailed studies will be required to determine the binding efficiency of our CDs with various metal cations. These results will shed light on the range of applicability of our system in natural water samples.

## References

1. Perutz, M. F., Regulation of Oxygen Affinity of Hemoglobin: Influence of Structure of the Globin on the Heme Iron. *Annual Review of Biochemistry* **1979**, *48* (1), 327-386.
2. Klotz, I. M.; Klotz, T. A., Oxygen-Carrying Proteins: A Comparison of the Oxygenation Reaction in Hemocyanin and Hemerythrin with That in Hemoglobin. *Science* **1955**, *121* (3145), 477-480.
3. Castiglioni, S.; Cazzaniga, A.; Albisetti, W.; Maier, J. A. M., Magnesium and osteoporosis: current state of knowledge and future research directions. *Nutrients* **2013**, *5* (8), 3022-3033.
4. Anderson, R. A., Chromium, glucose intolerance and diabetes. *J Am Coll Nutr* **1998**, *17* (6), 548-55.
5. Vincent, J. B., The Biochemistry of Chromium. *The Journal of Nutrition* **2000**, *130* (4), 715-718.
6. Anderson, R. A., Chromium and insulin resistance. *Nutrition Research Reviews* **2003**, *16* (2), 267-275.
7. World Health Organization (WHO), Guidelines for Drinking-water Quality. 4th edition ed.; 2017.
8. Jaishankar, M.; Tseten, T.; Anbalagan, N.; Mathew, B. B.; Beeregowda, K. N., Toxicity, mechanism and health effects of some heavy metals. *Interdiscip Toxicol* **2014**, *7* (2), 60-72.
9. Ibrahim, D.; Froberg, B.; Wolf, A.; Rusyniak, D. E., Heavy metal poisoning: clinical presentations and pathophysiology. *Clin Lab Med* **2006**, *26* (1), 67-97, viii.
10. Rusyniak, D. E.; Arroyo, A.; Acciani, J.; Froberg, B.; Kao, L.; Furbee, B., Heavy metal poisoning: management of intoxication and antidotes. *Exs* **2010**, *100*, 365-96.
11. Aragay, G.; Pons, J.; Merkoçi, A., Recent Trends in Macro-, Micro-, and Nanomaterial-Based Tools and Strategies for Heavy-Metal Detection. *Chemical Reviews* **2011**, *111* (5), 3433-3458.
12. The Mining Association of Canada (MAC) *Facts and Figures 2019: The State of Canada's Mining Industry*; 2019.
13. Environment and Climate Change Canada, Canadian Mercury Science Assessment: Summary of Key Results. Canada, G. o., Ed. 2016.
14. The Regional District of Nanaimo, Water Stewardship Information Series. In *Iron & Manganese in Groundwater*, 2007.
15. Natural Resources Canada (NRC) Iron Ore Facts. <https://www.nrcan.gc.ca/our-natural-resources/minerals-mining/iron-ore-facts/20517>.
16. Li, C.; Zhou, K.; Qin, W.; Tian, C.; Qi, M.; Yan, X.; Han, W., A Review on Heavy Metals Contamination in Soil: Effects, Sources, and Remediation Techniques. *Soil and Sediment Contamination: An International Journal* **2019**, *28* (4), 380-394.
17. Natural Resources Canada (NRC) Lead Facts. <https://www.nrcan.gc.ca/our-natural-resources/minerals-mining/minerals-metals-facts/lead-facts/20518>.
18. Health Canada, Guidelines for Canadian Drinking Water Quality: Guideline Technical Document. Water and Air Quality Bureau, H. E. a. C. S. B., Health Canada, Ed. Ottawa, Ontario, 2019.
19. Global News and the Institute for Investigative Journalism, Is Montreal's lead problem worse than Flint, Michigan's? *Global News* 2019.
20. Bienvenu, L.; Bergeron, K. The end of mercury mines. <https://mern.gouv.qc.ca/english/mines/quebec-mines/2015-02/mine-mercure.asp>.
21. D'Amato, I., Global Shift Towards Renewable Energy Happening at a 'Phenomenal' Pace, According to Experts. The Climate Group: London, 2017.
22. Roser, H. R. a. M., Renewable Energy. In *Our World in Data*, 2017.
23. United States Environmental Protection Agency (EPA) How People are Exposed to Mercury. <https://www.epa.gov/mercury/how-people-are-exposed-mercury#main-content>

24. Ministry of the Environment Conservation and Parks Mercury in Ontario. <https://www.ontario.ca/page/mercury-ontario>.
25. Natural Resources Canada (NRC), Natural Resources: Major Projects Planned or Under Construction – 2019 to 2029. In *Energy and Mines Ministers' Conference*, Cranbrook, BC, 2019.
26. Mungall, J., Column: Stalled Ring of Fire worth more than \$117 billion. *The Sudbury Star* 2020.
27. Sharp, A., Doug Ford still chasing Ring of Fire mining dream. *Canada's National Observer* 2020.
28. Noront Resources Ltd., Ontario Map 2020 02 06. 2020; p Noront's Eagle's Nest Deposit is located in Northwestern Ontario in the heart of the Ring of Fire.
29. García, R.; Báez, A. P., Atomic Absorption Spectrometry (AAS). In *Atomic Absorption Spectrometry (AAS)*, Farrukh, M. A., Ed. IntechOpen: 2012.
30. Hung, D. Q.; Nekrassova, O.; Compton, R. G., Analytical methods for inorganic arsenic in water: a review. *Talanta* **2004**, *64* (2), 269-277.
31. Harvey, D., *Modern Analytical Chemistry*. McGraw-Hill Companies Inc. : New York, 2000.
32. Davidson, H., Spectroscopy in Soil Analysis. AWE International Magazine: 2018.
33. Wilbur, S., A Comparison of the Relative Cost and Productivity of Traditional Metals Analysis Techniques Versus ICP-MS in High Throughput Commercial Laboratories. Inc., A. T., Ed. Bellevue, Washington, 2005.
34. Christensen, W. M.; Tokhtuev, E.; Carlson, B. P.; Kraus, P. R.; Pesigan, B. F.; Klegin, J. M.; Hartz, A. E.; Kremer, M. P. Handheld fluorometer and method of use US8269193B2, 2010.
35. Nelson, N.; Sander, D.; Dandin, M.; Prakash, S. B.; Sarje, A.; Abshire, P., Handheld Fluorometers for Lab-on-a-Chip Applications. *IEEE Transactions on Biomedical Circuits and Systems* **2009**, *3* (2), 97-107.
36. Shin, Y.-H.; Gutierrez-Wing, M. T.; Choi, J.-W., A field-deployable and handheld fluorometer for environmental water quality monitoring. *Micro and Nano Systems Letters* **2018**, *6* (1), 16.
37. Bellan, L. M.; Wu, D.; Langer, R. S., Current trends in nanobiosensor technology. *WIREs Nanomedicine and Nanobiotechnology* **2011**, *3* (3), 229-246.
38. Rosi, N. L.; Mirkin, C. A., Nanostructures in Biodiagnostics. *Chemical Reviews* **2005**, *105* (4), 1547-1562.
39. Auffan, M.; Rose, J.; Bottero, J.-Y.; Lowry, G. V.; Jolivet, J.-P.; Wiesner, M. R., Towards a definition of inorganic nanoparticles from an environmental, health and safety perspective. *Nature Nanotechnology* **2009**, *4* (10), 634-641.
40. Jana, J.; Ganguly, M.; Pal, T., Enlightening surface plasmon resonance effect of metal nanoparticles for practical spectroscopic application. *RSC Advances* **2016**, *6* (89), 86174-86211.
41. Parveen, K.; Banse, V.; Ledwani, L., Green synthesis of nanoparticles: Their advantages and disadvantages. *AIP Conference Proceedings* **2016**, *1724* (1), 020048.
42. Hoshino, A.; Fujioka, K.; Oku, T.; Suga, M.; Sasaki, Y. F.; Ohta, T.; Yasuhara, M.; Suzuki, K.; Yamamoto, K., Physicochemical Properties and Cellular Toxicity of Nanocrystal Quantum Dots Depend on Their Surface Modification. *Nano Letters* **2004**, *4* (11), 2163-2169.
43. Wang, Y.; Hu, A., Carbon quantum dots: synthesis, properties and applications. *Journal of Materials Chemistry C* **2014**, *2* (34), 6921-6939.
44. Proposito, P.; Mochi, F.; Ciotta, E.; Casalboni, M.; De Matteis, F.; Venditti, I.; Fontana, L.; Testa, G.; Fratoddi, I., Hydrophilic silver nanoparticles with tunable optical properties: application for the detection of heavy metals in water. *Beilstein Journal of Nanotechnology* **2016**, *7*, 1654-1661.
45. Yoo, S. M.; Lee, S. Y., Optical Biosensors for the Detection of Pathogenic Microorganisms. *Trends in Biotechnology* **2016**, *34* (1), 7-25.

46. Velasco-Garcia, M. N., Optical biosensors for probing at the cellular level: A review of recent progress and future prospects. *Seminars in Cell & Developmental Biology* **2009**, *20* (1), 27-33.
47. Jeong, H. Programmable chiral nanocolloids. Ph.D. Thesis, École polytechnique fédérale de lausanne (EPFL), Switzerland, 2017.
48. Huang, H.; Qu, C.; Liu, X.; Huang, S.; Xu, Z.; Zhu, Y.; Chu, P. K., Amplification of localized surface plasmon resonance signals by a gold nanorod assembly and ultra-sensitive detection of mercury. *Chemical Communications* **2011**, *47* (24), 6897-6899.
49. Shaheen, T. I.; El-Naggar, M. E.; Hussein, J. S.; El-Bana, M.; Emara, E.; El-Khayat, Z.; Fouda, M. M. G.; Ebaid, H.; Hebeish, A., Antidiabetic assessment; in vivo study of gold and core-shell silver-gold nanoparticles on streptozotocin-induced diabetic rats. *Biomedicine & Pharmacotherapy* **2016**, *83*, 865-875.
50. Wilson, R., The use of gold nanoparticles in diagnostics and detection. *Chemical Society Reviews* **2008**, *37* (9), 2028-2045.
51. Bera, D.; Qian, L.; Tseng, T.-K.; Holloway, P. H., Quantum Dots and Their Multimodal Applications: A Review. *Materials* **2010**, *3* (4), 2260-2345.
52. Zhu, S.; Song, Y.; Zhao, X.; Shao, J.; Zhang, J.; Yang, B., The photoluminescence mechanism in carbon dots (graphene quantum dots, carbon nanodots, and polymer dots): current state and future perspective. *Nano Research* **2015**, *8* (2), 355-381.
53. Lakowicz, J. R., *Principles of Fluorescence Spectroscopy*. 3rd Edition ed.; Springer Science+Business Media,: 2006.
54. Zu, F.; Yan, F.; Bai, Z.; Xu, J.; Wang, Y.; Huang, Y.; Zhou, X., The quenching of the fluorescence of carbon dots: A review on mechanisms and applications. *Microchimica Acta* **2017**, *184* (7), 1899-1914.
55. Elmizadeh, H.; Soleimani, M.; Faridbod, F.; Bardajee, G. R., A sensitive nano-sensor based on synthetic ligand-coated CdTe quantum dots for rapid detection of Cr(III) ions in water and wastewater samples. *Colloid and Polymer Science* **2018**, *296* (9), 1581-1590.
56. Hardman, R., A Toxicologic Review of Quantum Dots: Toxicity Depends on Physicochemical and Environmental Factors. *Environmental Health Perspectives* **2006**, *114* (2), 165-172.
57. Zhang, Q.; Wu, B.; Zhong, D.; Zhan, X.; Wang, G., Polymer Dots of Peryleneimide-Functionalized Polyethyleneimine: Facile Synthesis and Effective Fluorescent Sensing of Iron (III) Ions. *Macromolecular Rapid Communications* **2016**, *37* (24), 2052-2056.
58. Wu, C.; Chiu, D. T., Highly Fluorescent Semiconducting Polymer Dots for Biology and Medicine. *Angewandte Chemie International Edition* **2013**, *52* (11), 3086-3109.
59. Gupta, R.; Peveler, W. J.; Lix, K.; Algar, W. R., Comparison of Semiconducting Polymer Dots and Semiconductor Quantum Dots for Smartphone-Based Fluorescence Assays. *Analytical Chemistry* **2019**, *91* (17), 10955-10960.
60. Xu, X.; Ray, R.; Gu, Y.; Ploehn, H. J.; Gearheart, L.; Raker, K.; Scrivens, W. A., Electrophoretic Analysis and Purification of Fluorescent Single-Walled Carbon Nanotube Fragments. *Journal of the American Chemical Society* **2004**, *126* (40), 12736-12737.
61. de Medeiros, T. V.; Manioudakis, J.; Noun, F.; Macairan, J.-R.; Victoria, F.; Naccache, R., Microwave-assisted synthesis of carbon dots and their applications. *Journal of Materials Chemistry C* **2019**, *7* (24), 7175-7195.
62. Zuo, P.; Lu, X.; Sun, Z.; Guo, Y.; He, H., A review on syntheses, properties, characterization and bioanalytical applications of fluorescent carbon dots. *Microchimica Acta* **2016**, *183* (2), 519-542.

63. Zhang, J.; Yu, S.-H., Carbon dots: large-scale synthesis, sensing and bioimaging. *Materials Today* **2016**, *19* (7), 382-393.
64. Manioudakis, J.; Victoria, F.; Thompson, C. A.; Brown, L.; Movsum, M.; Lucifero, R.; Naccache, R., Effects of nitrogen-doping on the photophysical properties of carbon dots. *Journal of Materials Chemistry C* **2019**, *7* (4), 853-862.
65. Simões, E. F. C.; Leitão, J. M. M.; da Silva, J. C. G. E., Carbon dots prepared from citric acid and urea as fluorescent probes for hypochlorite and peroxyxynitrite. *Microchimica Acta* **2016**, *183* (5), 1769-1777.
66. Macairan, J.-R.; Jaunky, D. B.; Piekny, A.; Naccache, R., Intracellular ratiometric temperature sensing using fluorescent carbon dots. *Nanoscale Advances* **2019**, *1* (1), 105-113.
67. Wang, Z.; Xu, C.; Lu, Y.; Chen, X.; Yuan, H.; Wei, G.; Ye, G.; Chen, J., Fluorescence sensor array based on amino acid derived carbon dots for pattern-based detection of toxic metal ions. *Sensors and Actuators B: Chemical* **2017**, *241*, 1324-1330.
68. Babar, D. G.; Sonkar, S. K.; Tripathi, K. M.; Sarkar, S., P2O5 Assisted Green Synthesis of Multicolor Fluorescent Water Soluble Carbon Dots. *Journal of Nanoscience and Nanotechnology* **2014**, *14* (3), 2334-2342.
69. Hill, S. A.; Benito-Alifonso, D.; Morgan, D. J.; Davis, S. A.; Berry, M.; Galan, M. C., Three-minute synthesis of sp<sup>3</sup> nanocrystalline carbon dots as non-toxic fluorescent platforms for intracellular delivery. *Nanoscale* **2016**, *8* (44), 18630-18634.
70. Yang, X.; Zhuo, Y.; Zhu, S.; Luo, Y.; Feng, Y.; Dou, Y., Novel and green synthesis of high-fluorescent carbon dots originated from honey for sensing and imaging. *Biosensors and Bioelectronics* **2014**, *60*, 292-298.
71. Sharma, V.; Tiwari, P.; Mobin, S. M., Sustainable carbon-dots: recent advances in green carbon dots for sensing and bioimaging. *Journal of Materials Chemistry B* **2017**, *5* (45), 8904-8924.
72. Sahu, S.; Behera, B.; Maiti, T. K.; Mohapatra, S., Simple one-step synthesis of highly luminescent carbon dots from orange juice: application as excellent bio-imaging agents. *Chemical Communications* **2012**, *48* (70), 8835-8837.
73. Wang, L.; Zhou, H. S., Green Synthesis of Luminescent Nitrogen-Doped Carbon Dots from Milk and Its Imaging Application. *Analytical Chemistry* **2014**, *86* (18), 8902-8905.
74. Wang, D.; Wang, X.; Guo, Y.; Liu, W.; Qin, W., Luminescent properties of milk carbon dots and their sulphur and nitrogen doped analogues. *RSC Advances* **2014**, *4* (93), 51658-51665.
75. Macairan, J.-R.; Zhang, I.; Clermont-Paquette, A.; Naccache, R.; Maysinger, D., Ratiometric pH Sensing in Living Cells Using Carbon Dots. *Particle & Particle Systems Characterization* **2020**, *37* (1), 1900430.
76. Bagheri, Z.; Ehtesabi, H.; Hallaji, Z.; Latifi, H.; Behroodi, E., Investigation the cytotoxicity and photo-induced toxicity of carbon dot on yeast cell. *Ecotoxicology and Environmental Safety* **2018**, *161*, 245-250.
77. Luo, P. G.; Sahu, S.; Yang, S.-T.; Sonkar, S. K.; Wang, J.; Wang, H.; LeCroy, G. E.; Cao, L.; Sun, Y.-P., Carbon “quantum” dots for optical bioimaging. *Journal of Materials Chemistry B* **2013**, *1* (16), 2116-2127.
78. Lim, S. Y.; Shen, W.; Gao, Z., Carbon quantum dots and their applications. *Chemical Society Reviews* **2015**, *44* (1), 362-381.
79. Kokorina, A. A.; Prikhozhenko, E. S.; Sukhorukov, G. B.; Sapelkin, A. V.; Goryacheva, I. Y., Luminescent carbon nanoparticles: synthesis, methods of investigation, applications. *Russian Chemical Reviews* **2017**, *86* (11), 1157-1171.

80. Li, X.; Zhang, S.; Kulinich, S. A.; Liu, Y.; Zeng, H., Engineering surface states of carbon dots to achieve controllable luminescence for solid-luminescent composites and sensitive Be<sup>2+</sup> detection. *Scientific Reports* **2014**, *4* (1), 4976.
81. Bhattacharya, A.; Chatterjee, S.; Prajapati, R.; Mukherjee, T. K., Size-dependent penetration of carbon dots inside the ferritin nanocages: evidence for the quantum confinement effect in carbon dots. *Physical Chemistry Chemical Physics* **2015**, *17* (19), 12833-12840.
82. Gan, Z.; Xu, H.; Hao, Y., Mechanism for excitation-dependent photoluminescence from graphene quantum dots and other graphene oxide derivatives: consensus, debates and challenges. *Nanoscale* **2016**, *8* (15), 7794-7807.
83. Sciortino, A.; Marino, E.; Dam, B. v.; Schall, P.; Cannas, M.; Messina, F., Solvatochromism Unravels the Emission Mechanism of Carbon Nanodots. *The Journal of Physical Chemistry Letters* **2016**, *7* (17), 3419-3423.
84. Wen, Z.-H.; Yin, X.-B., Excitation-independent carbon dots, from photoluminescence mechanism to single-color application. *RSC Advances* **2016**, *6* (33), 27829-27835.
85. Yu, J.; Liu, C.; Yuan, K.; Lu, Z.; Cheng, Y.; Li, L.; Zhang, X.; Jin, P.; Meng, F.; Liu, H., Luminescence Mechanism of Carbon Dots by Tailoring Functional Groups for Sensing Fe<sup>3+</sup> Ions. *Nanomaterials* **2018**, *8* (4), 233.
86. Nie, H.; Li, M.; Li, Q.; Liang, S.; Tan, Y.; Sheng, L.; Shi, W.; Zhang, S. X.-A., Carbon Dots with Continuously Tunable Full-Color Emission and Their Application in Ratiometric pH Sensing. *Chemistry of Materials* **2014**, *26* (10), 3104-3112.
87. Du, F.; Zeng, F.; Ming, Y.; Wu, S., Carbon dots-based fluorescent probes for sensitive and selective detection of iodide. *Microchimica Acta* **2013**, *180* (5), 453-460.
88. Liang, Y.; Zhang, H.; Zhang, Y.; Chen, F., Simple hydrothermal preparation of carbon nanodots and their application in colorimetric and fluorimetric detection of mercury ions. *Analytical Methods* **2015**, *7* (18), 7540-7547.
89. Ninwong, B.; Sangkaew, P.; Hapa, P.; Ratnarathorn, N.; Menger, R. F.; Henry, C. S.; Dungchai, W., Sensitive distance-based paper-based quantification of mercury ions using carbon nanodots and heating-based preconcentration. *RSC Advances* **2020**, *10* (17), 9884-9893.
90. Ye, J.; Geng, Y.; Cao, F.; Sun, D.; Xu, S.; Chang, J.; Xu, W.; Chen, Q., A Smartphone-assisted Paper-based Analytical Device for Fluorescence Assay of Hg<sup>2+</sup>. *Chemical Research in Chinese Universities* **2019**, *35* (6), 972-977.
91. Yan, F.; Zou, Y.; Wang, M.; Mu, X.; Yang, N.; Chen, L., Highly photoluminescent carbon dots-based fluorescent chemosensors for sensitive and selective detection of mercury ions and application of imaging in living cells. *Sensors and Actuators B: Chemical* **2014**, *192*, 488-495.
92. Zhang, R.; Chen, W., Nitrogen-doped carbon quantum dots: Facile synthesis and application as a "turn-off" fluorescent probe for detection of Hg<sup>2+</sup> ions. *Biosensors and Bioelectronics* **2014**, *55*, 83-90.
93. Gong, X.; Lu, W.; Paau, M. C.; Hu, Q.; Wu, X.; Shuang, S.; Dong, C.; Choi, M. M. F., Facile synthesis of nitrogen-doped carbon dots for Fe<sup>3+</sup> sensing and cellular imaging. *Analytica Chimica Acta* **2015**, *861*, 74-84.
94. Xu, Q.; Pu, P.; Zhao, J.; Dong, C.; Gao, C.; Chen, Y.; Chen, J.; Liu, Y.; Zhou, H., Preparation of highly photoluminescent sulfur-doped carbon dots for Fe(III) detection. *Journal of Materials Chemistry A* **2015**, *3* (2), 542-546.
95. Liu, Y.; Zhou, Q.; Li, J.; Lei, M.; Yan, X., Selective and sensitive chemosensor for lead ions using fluorescent carbon dots prepared from chocolate by one-step hydrothermal method. *Sensors and Actuators B: Chemical* **2016**, *237*, 597-604.

96. Yarur, F.; Macairan, J.-R.; Naccache, R., Ratiometric detection of heavy metal ions using fluorescent carbon dots. *Environmental Science: Nano* **2019**, *6* (4), 1121-1130.
97. Schindelin, J.; Arganda-Carreras, I.; Frise, E.; Kaynig, V.; Longair, M.; Pietzsch, T.; Preibisch, S.; Rueden, C.; Saalfeld, S.; Schmid, B.; Tinevez, J. Y.; White, D. J.; Hartenstein, V.; Eliceiri, K.; Tomancak, P.; Cardona, A., Fiji: an open-source platform for biological-image analysis. *Nat Methods* **2012**, *9* (7), 676-82.
98. Boldyrev, I. A.; Zhai, X.; Momsen, M. M.; Brockman, H. L.; Brown, R. E.; Molotkovsky, J. G., New BODIPY lipid probes for fluorescence studies of membranes. *Journal of Lipid Research* **2007**, *48* (7), 1518-1532.
99. Kasparek, A.; Smyk, B., A new approach to the old problem: Inner filter effect type I and II in fluorescence. *Spectrochimica Acta Part A: Molecular and Biomolecular Spectroscopy* **2018**, *198*, 297-303.
100. Rao, L.; Tang, Y.; Lu, H.; Yu, S.; Ding, X.; Xu, K.; Li, Z.; Zhang, J. Z., Highly Photoluminescent and Stable N-Doped Carbon Dots as Nanoprobes for Hg<sup>2+</sup> Detection. *Nanomaterials* **2018**, *8* (11), 900.
101. Loukanov, A.; Sekiya, R.; Yoshikawa, M.; Kobayashi, N.; Moriyasu, Y.; Nakabayashi, S., Photosensitizer-Conjugated Ultrasmall Carbon Nanodots as Multifunctional Fluorescent Probes for Bioimaging. *The Journal of Physical Chemistry C* **2016**, *120* (29), 15867-15874.
102. Dong, X.; Su, Y.; Geng, H.; Li, Z.; Yang, C.; Li, X.; Zhang, Y., Fast one-step synthesis of N-doped carbon dots by pyrolyzing ethanolamine. *Journal of Materials Chemistry C* **2014**, *2* (36), 7477-7481.
103. Zhou, J.; Shan, X.; Ma, J.; Gu, Y.; Qian, Z.; Chen, J.; Feng, H., Facile synthesis of P-doped carbon quantum dots with highly efficient photoluminescence. *RSC Advances* **2014**, *4* (11), 5465-5468.
104. Wang, J.; Qiu, J., A review of carbon dots in biological applications. *Journal of Materials Science* **2016**, *51* (10), 4728-4738.
105. Liu, H.; Li, Z.; Sun, Y.; Geng, X.; Hu, Y.; Meng, H.; Ge, J.; Qu, L., Synthesis of Luminescent Carbon Dots with Ultrahigh Quantum Yield and Inherent Folate Receptor-Positive Cancer Cell Targetability. *Scientific Reports* **2018**, *8* (1), 1086.
106. Hou, J.; Wang, W.; Zhou, T.; Wang, B.; Li, H.; Ding, L., Synthesis and formation mechanistic investigation of nitrogen-doped carbon dots with high quantum yields and yellowish-green fluorescence. *Nanoscale* **2016**, *8* (21), 11185-11193.
107. Himaja, A. L.; Karthik, P. S.; Singh, S. P., Carbon Dots: The Newest Member of the Carbon Nanomaterials Family. *The Chemical Record* **2015**, *15* (3), 595-615.
108. Schneider, J.; Reckmeier, C. J.; Xiong, Y.; von Seckendorff, M.; Susha, A. S.; Kasák, P.; Rogach, A. L., Molecular Fluorescence in Citric Acid-Based Carbon Dots. *The Journal of Physical Chemistry C* **2017**, *121* (3), 2014-2022.
109. Song, Y.; Zhu, S.; Zhang, S.; Fu, Y.; Wang, L.; Zhao, X.; Yang, B., Investigation from chemical structure to photoluminescent mechanism: a type of carbon dots from the pyrolysis of citric acid and an amine. *Journal of Materials Chemistry C* **2015**, *3* (23), 5976-5984.
110. Hu, Y.; Yang, J.; Tian, J.; Yu, J.-S., How do nitrogen-doped carbon dots generate from molecular precursors? An investigation of the formation mechanism and a solution-based large-scale synthesis. *Journal of Materials Chemistry B* **2015**, *3* (27), 5608-5614.
111. Repligen Corporation, Relative Pore Size Chart. 2019; pp The following chart shows the different pore sizes and molecules ideal for ultrafiltration, diafiltration, microfiltration, dialysis, and macrofiltration.

112. Zeng, Y.-W.; Ma, D.-K.; Wang, W.; Chen, J.-J.; Zhou, L.; Zheng, Y.-Z.; Yu, K.; Huang, S.-M., N, S co-doped carbon dots with orange luminescence synthesized through polymerization and carbonization reaction of amino acids. *Applied Surface Science* **2015**, *342*, 136-143.
113. Shen, L.; Zhang, L.; Chen, M.; Chen, X.; Wang, J., The production of pH-sensitive photoluminescent carbon nanoparticles by the carbonization of polyethylenimine and their use for bioimaging. *Carbon* **2013**, *55*, 343-349.
114. Ehrat, F.; Bhattacharyya, S.; Schneider, J.; Löf, A.; Wyrwich, R.; Rogach, A. L.; Stolarczyk, J. K.; Urban, A. S.; Feldmann, J., Tracking the Source of Carbon Dot Photoluminescence: Aromatic Domains versus Molecular Fluorophores. *Nano Letters* **2017**, *17* (12), 7710-7716.
115. Zhu, S.; Zhao, X.; Song, Y.; Lu, S.; Yang, B., Beyond bottom-up carbon nanodots: Citric-acid derived organic molecules. *Nano Today* **2016**, *11* (2), 128-132.
116. Xie, Z.; Kim, J. P.; Cai, Q.; Zhang, Y.; Guo, J.; Dhimi, R. S.; Li, L.; Kong, B.; Su, Y.; Schug, K. A.; Yang, J., Synthesis and characterization of citrate-based fluorescent small molecules and biodegradable polymers. *Acta Biomaterialia* **2017**, *50*, 361-369.
117. Sell, W. J.; Easterfield, T. H., LXXIII.—Studies on citrazinic acid. Part I. *Journal of the Chemical Society, Transactions* **1893**, *63* (0), 1035-1051.
118. Kasprzyk, W.; Bednarsz, S.; Żmudzki, P.; Galica, M.; Bogdał, D., Novel efficient fluorophores synthesized from citric acid. *RSC Advances* **2015**, *5* (44), 34795-34799.
119. Liu, Y.; Liu, C.-y.; Zhang, Z.-y., Synthesis of highly luminescent graphitized carbon dots and the application in the Hg<sup>2+</sup> detection. *Applied Surface Science* **2012**, *263*, 481-485.
120. Bao, L.; Liu, C.; Zhang, Z.-L.; Pang, D.-W., Photoluminescence-Tunable Carbon Nanodots: Surface-State Energy-Gap Tuning. *Advanced Materials* **2015**, *27* (10), 1663-1667.
121. Stagi, L.; Mura, S.; Malfatti, L.; Carbonaro, C. M.; Ricci, P. C.; Porcu, S.; Secci, F.; Innocenzi, P., Anomalous Optical Properties of Citrazinic Acid under Extreme pH Conditions. *ACS Omega* **2020**.
122. Reckmeier, C. J.; Schneider, J.; Xiong, Y.; Häusler, J.; Kasák, P.; Schnick, W.; Rogach, A. L., Aggregated Molecular Fluorophores in the Ammonothermal Synthesis of Carbon Dots. *Chemistry of Materials* **2017**, *29* (24), 10352-10361.
123. Würth, C.; Grabolle, M.; Pauli, J.; Spieles, M.; Resch-Genger, U., Relative and absolute determination of fluorescence quantum yields of transparent samples. *Nature Protocols* **2013**, *8* (8), 1535-1550.
124. Shen, Q.; Mikkola, P.; Rosenholm, J. B., Quantitative characterization of the subsurface acid–base properties of wood by XPS and Fowkes theory. *Colloids and Surfaces A: Physicochemical and Engineering Aspects* **1998**, *145* (1), 235-241.
125. Pan, L.; Sun, S.; Zhang, L.; Jiang, K.; Lin, H., Near-infrared emissive carbon dots for two-photon fluorescence bioimaging. *Nanoscale* **2016**, *8* (39), 17350-17356.
126. Qu, D.; Zheng, M.; Du, P.; Zhou, Y.; Zhang, L.; Li, D.; Tan, H.; Zhao, Z.; Xie, Z.; Sun, Z., Highly luminescent S, N co-doped graphene quantum dots with broad visible absorption bands for visible light photocatalysts. *Nanoscale* **2013**, *5* (24), 12272-12277.
127. Rayner-Canham, G.; Overton, T., *Descriptive Inorganic Chemistry*. 6th ed.; W. H. Freeman & Co.: 2013.
128. Chen, S.; Yu, Y.-L.; Wang, J.-H., Inner filter effect-based fluorescent sensing systems: A review. *Analytica Chimica Acta* **2018**, *999*, 13-26.
129. Ferreira, C. M. H.; Pinto, I. S. S.; Soares, E. V.; Soares, H. M. V. M., (Un)suitability of the use of pH buffers in biological, biochemical and environmental studies and their interaction with metal ions – a review. *RSC Advances* **2015**, *5* (39), 30989-31003.

130. Sokołowska, M.; Pawlas, K.; Bal, W., Effect of Common Buffers and Heterocyclic Ligands on the Binding of Cu(II) at the Multimetal Binding Site in Human Serum Albumin. *Bioinorganic Chemistry and Applications* **2010**, 2010.
131. Ministère du développement durable de l'environnement et de la lutte contre les changements climatiques, Bilan de la qualité de l'eau potable au Québec 2010-2014. 2016; p 80.
132. Klep, O.; Bandera, Y.; Foulger, S. H., Temperature responsive nanoparticles: poloxamers as a modulator of Förster resonance energy transfer (FRET). *Nanoscale* **2018**, 10 (19), 9401-9409.
133. Hemmer, E.; Quintanilla, M.; Légaré, F.; Vetrone, F., Temperature-Induced Energy Transfer in Dye-Conjugated Upconverting Nanoparticles: A New Candidate for Nanothermometry. *Chemistry of Materials* **2015**, 27 (1), 235-244.
134. Chen, N.-T.; Cheng, S.-H.; Liu, C.-P.; Souris, J. S.; Chen, C.-T.; Mou, C.-Y.; Lo, L.-W., Recent advances in nanoparticle-based Förster resonance energy transfer for biosensing, molecular imaging and drug release profiling. *International journal of molecular sciences* **2012**, 13 (12), 16598-16623.
135. Cangelosi, V.; Ruckthong, L.; Pecoraro, V. L., Lead(II) Binding in Natural and Artificial Proteins. *Met Ions Life Sci* **2017**, 17, /books/9783110434330/9783110434330-010/9783110434330-010.xml.
136. Magyar, J. S.; Weng, T.-C.; Stern, C. M.; Dye, D. F.; Rous, B. W.; Payne, J. C.; Bridgewater, B. M.; Mijovilovich, A.; Parkin, G.; Zaleski, J. M.; Penner-Hahn, J. E.; Godwin, H. A., Reexamination of Lead(II) Coordination Preferences in Sulfur-Rich Sites: Implications for a Critical Mechanism of Lead Poisoning. *Journal of the American Chemical Society* **2005**, 127 (26), 9495-9505.
137. Melnick, J. G.; Yurkerwich, K.; Parkin, G., On the chalcogenophilicity of mercury: evidence for a strong Hg-Se bond in [Tm(Bu(t))]<sub>2</sub>HgSePh and its relevance to the toxicity of mercury. *Journal of the American Chemical Society* **2010**, 132 (2), 647-655.
138. United States Environmental Protection Agency (EPA), Framework for Metals Risk Assessment. Agency, U. S. E. P., Ed. Washington, D.C., 2007; p 172.
139. Suzuki, K.; Yamasaki, K., The stability of some metal complexes incorporating oxygen or sulphur as donor atoms. *Journal of Inorganic and Nuclear Chemistry* **1962**, 24 (9), 1093-1103.
140. Vahrenkamp, H., Sulfur Atoms as Ligands in Metal Complexes. *Angewandte Chemie International Edition in English* **1975**, 14 (5), 322-329.
141. Aiken, G. R.; Hsu-Kim, H.; Ryan, J. N., Influence of Dissolved Organic Matter on the Environmental Fate of Metals, Nanoparticles, and Colloids. *Environmental Science & Technology* **2011**, 45 (8), 3196-3201.
142. Baken, S.; Degryse, F.; Verheyen, L.; Merckx, R.; Smolders, E., Metal Complexation Properties of Freshwater Dissolved Organic Matter Are Explained by Its Aromaticity and by Anthropogenic Ligands. *Environmental Science & Technology* **2011**, 45 (7), 2584-2590.

## Appendix

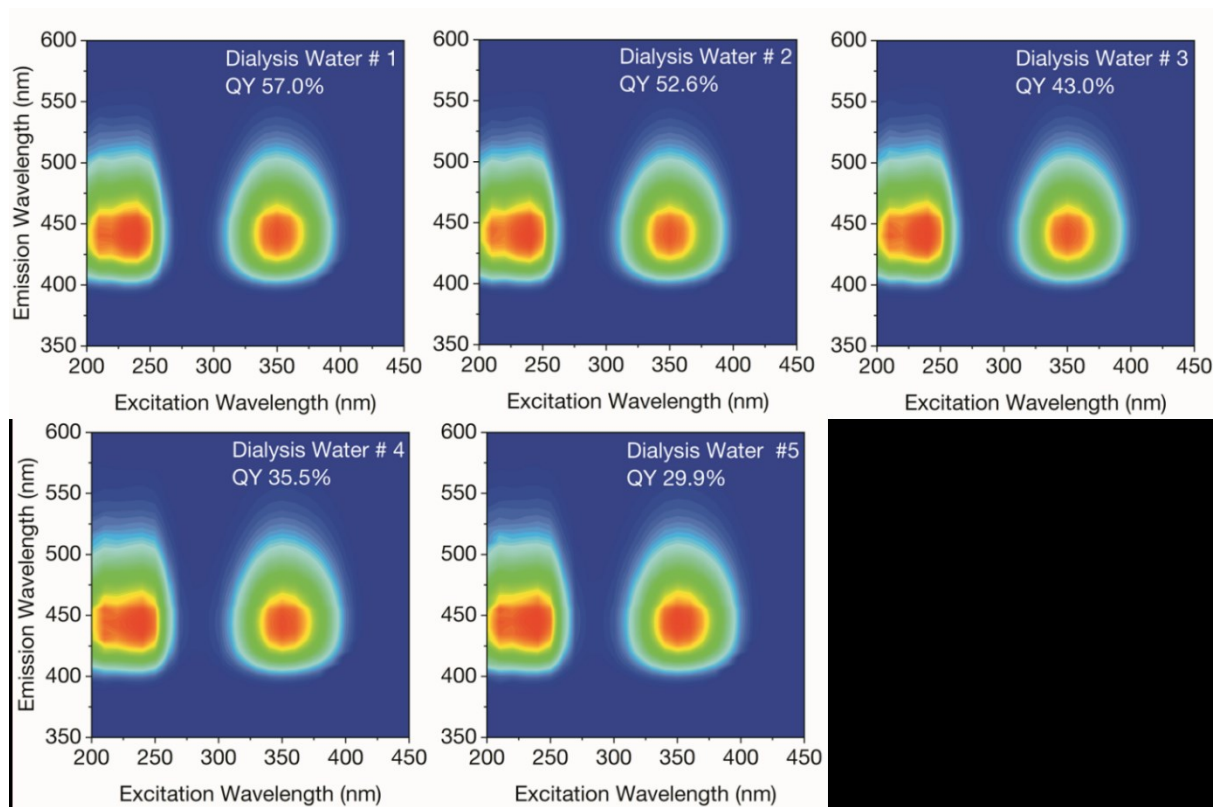


**Figure A 1:** Fluorescence contour plot for the **dialysate of 375DT3-CDs** at various dialysis steps without any organic washes. We observe excitation-independent fluorescence with an emission maximum centered at  $\sim 445$  nm.

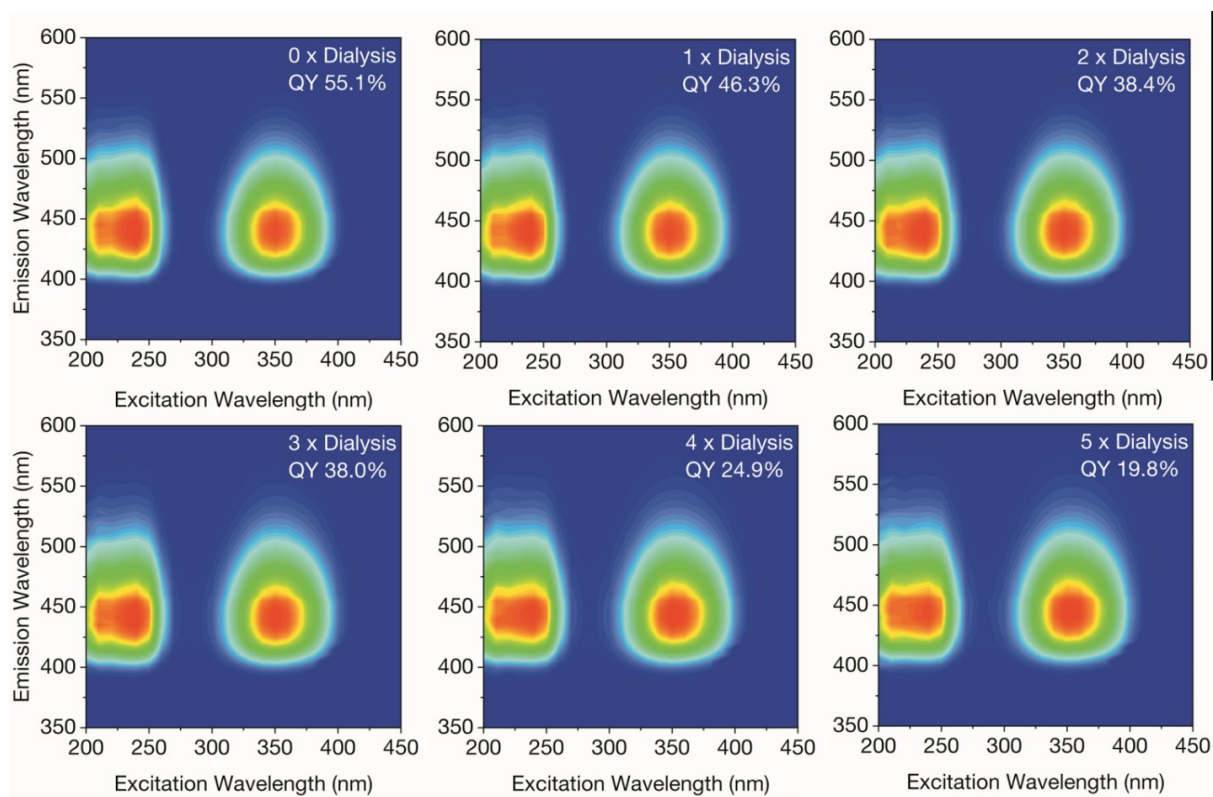


**Figure A 2:** Fluorescence contour plot for 375DT3-CDs purified via **several dialysis steps without any organic washes**. We observe excitation-independent fluorescence with an emission maximum centered at  $\sim 445$  nm.

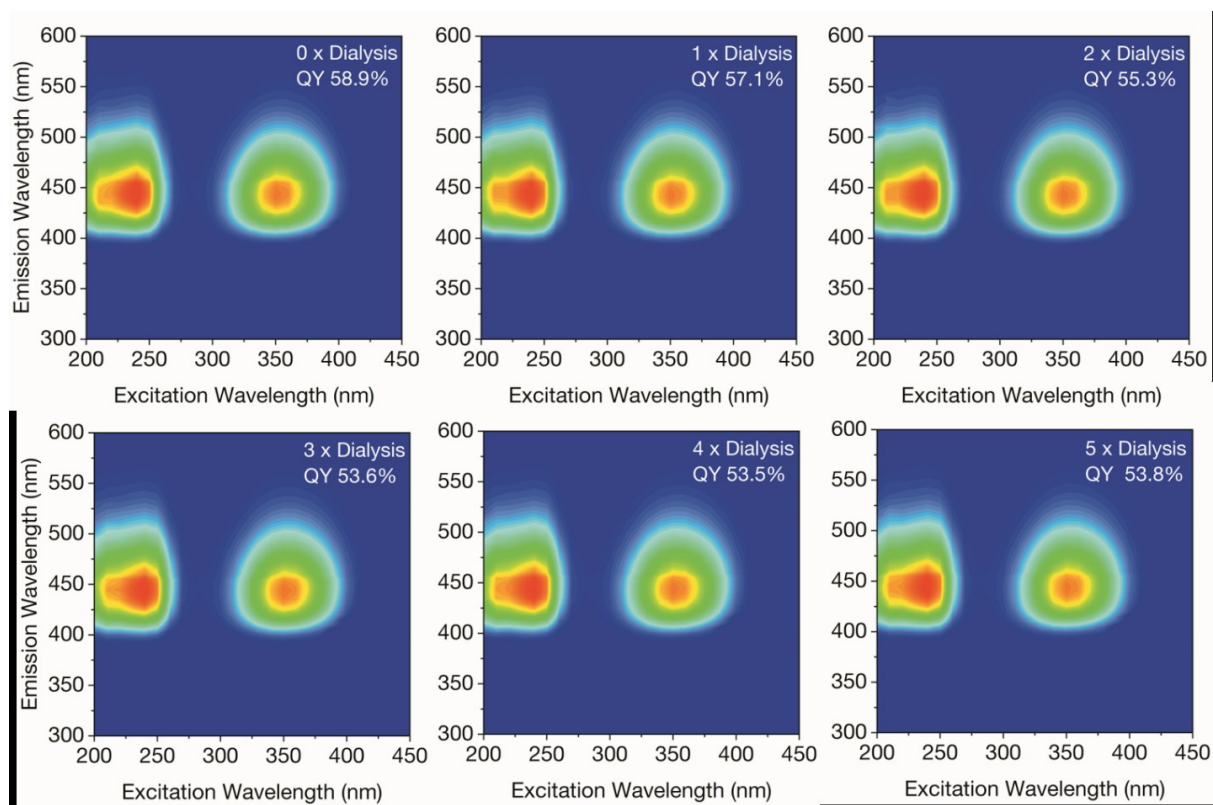


**Figure A 3:** Fluorescence contour plot for 375DT3-CDs purified via **several dialysis steps and subsequent organic washes**. We observe excitation-independent fluorescence with an emission maximum centered at  $\sim 445$  nm.

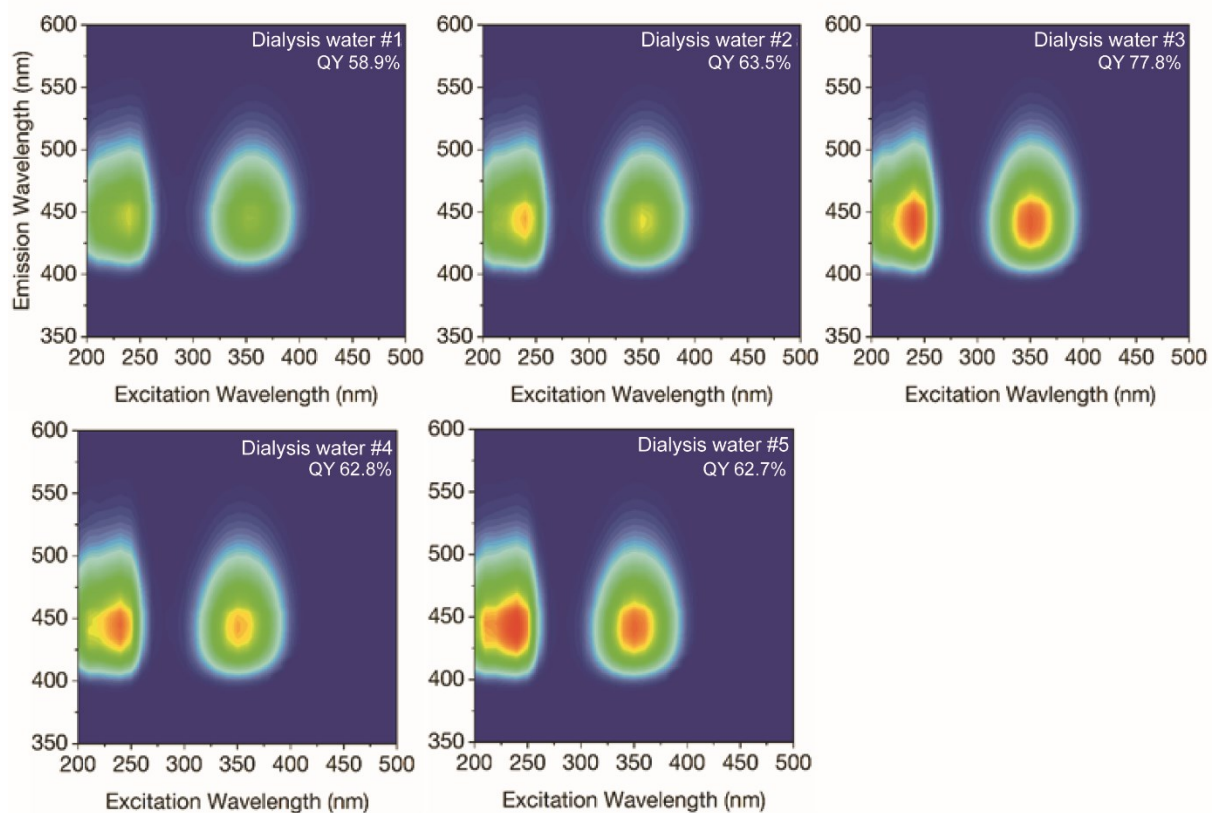


**Figure A 4:** Fluorescence contour plot for **dialysate of 750DT3-CDs** at various dialysis steps without any organic washes. We observe excitation-independent fluorescence with an emission maximum centered at  $\sim 445$  nm.

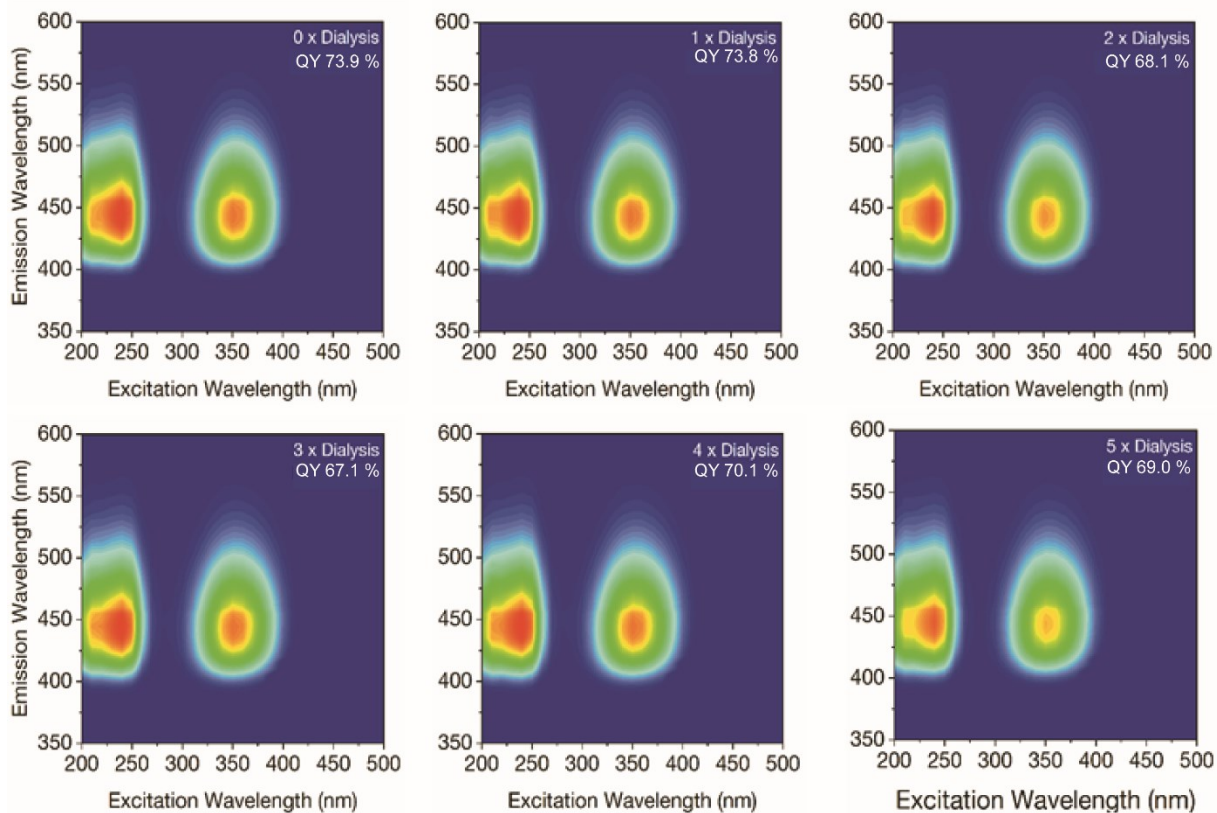


**Figure A 5:** Fluorescence contour plot for 750DT3-CDs purified via **various dialysis steps without any organic washes**. We observe excitation-independent fluorescence with an emission maximum centered at  $\sim 445$  nm.

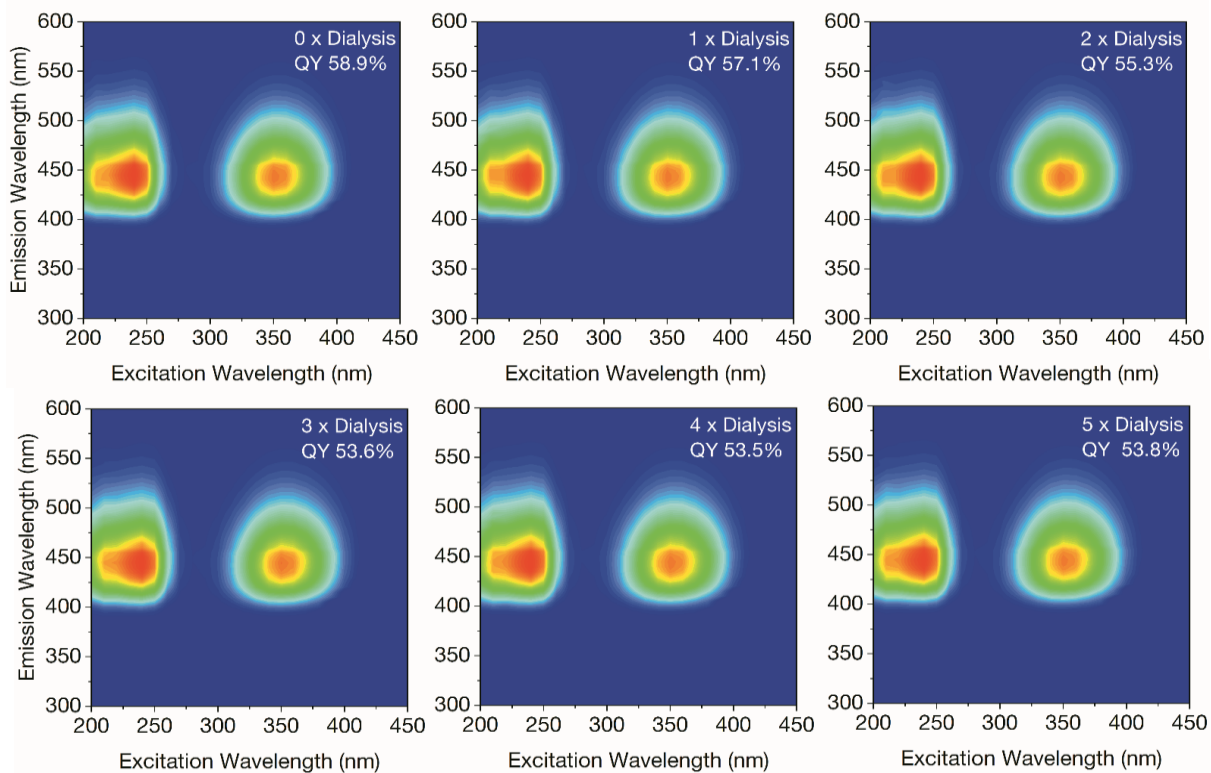


**Figure A 6:** Fluorescence contour plot for 750DT3-CDs purified via **various dialysis steps and subsequent organic washes**. We observe excitation-independent fluorescence with an emission maximum centered at  $\sim 445$  nm.

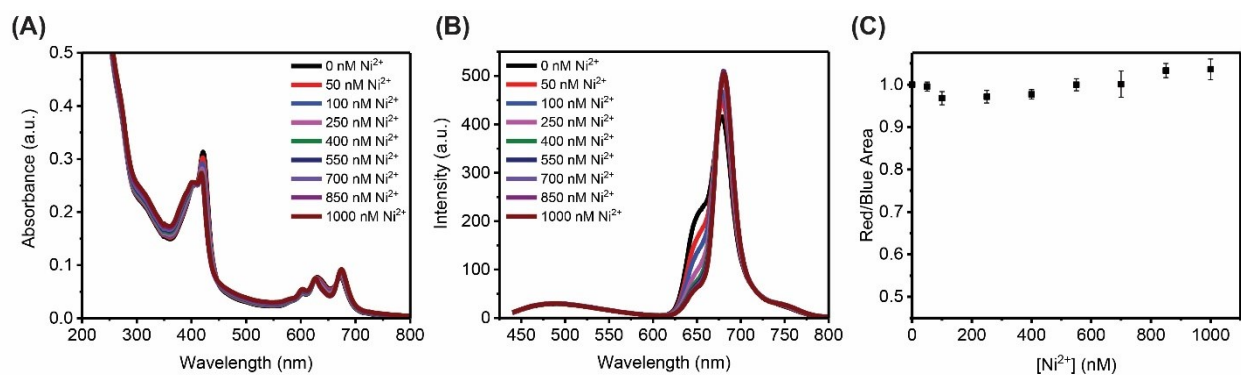


**Figure A 9:** Results of the quenching assay performed on FG-CDs using  $\text{Ni}^{2+}$  showing changes in (A) the absorbance spectrum (B) the fluorescence spectrum and (C) the Red/Blue area ratio. No significant quenching is observed with this metal cation.

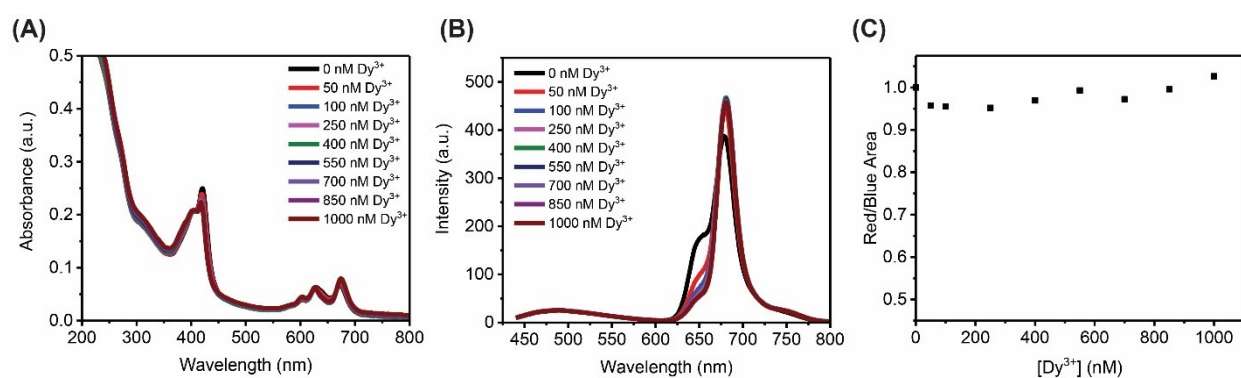


**Figure A 8:** Results of the quenching assay performed on FG-CDs using  $\text{Dy}^{3+}$  showing changes in (A) the absorbance spectrum (B) the fluorescence spectrum and (C) the Red/Blue area ratio. No significant quenching is observed with this metal cation.

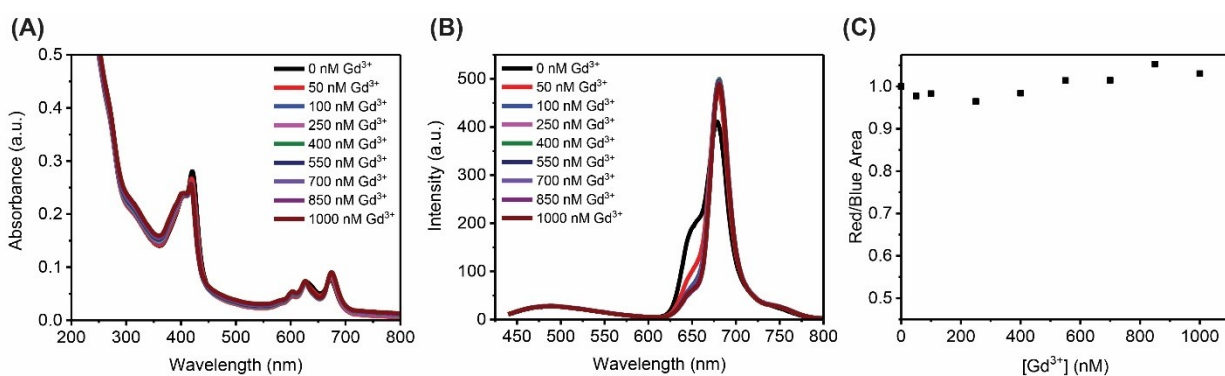


**Figure A 7:** Results of the quenching assay performed on FG-CDs using  $\text{Gd}^{3+}$  showing changes in (A) the absorbance spectrum (B) the fluorescence spectrum and (C) the Red/Blue area ratio. No significant quenching is observed with this metal cation.

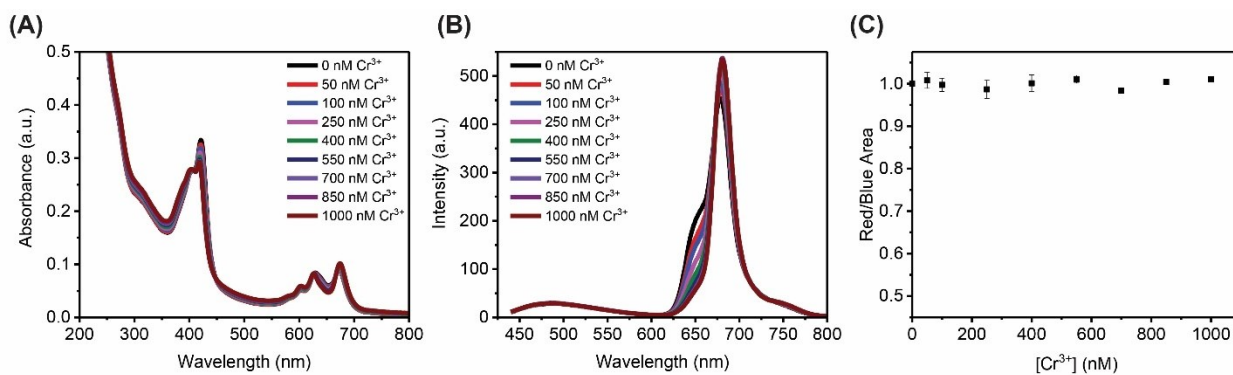


**Figure A 10:** Results of the quenching assay performed on FG-CDs using  $\text{Cr}^{3+}$  showing changes in (A) the absorbance spectrum (B) the fluorescence spectrum and (C) the Red/Blue area ratio. No significant quenching is observed with this metal cation.

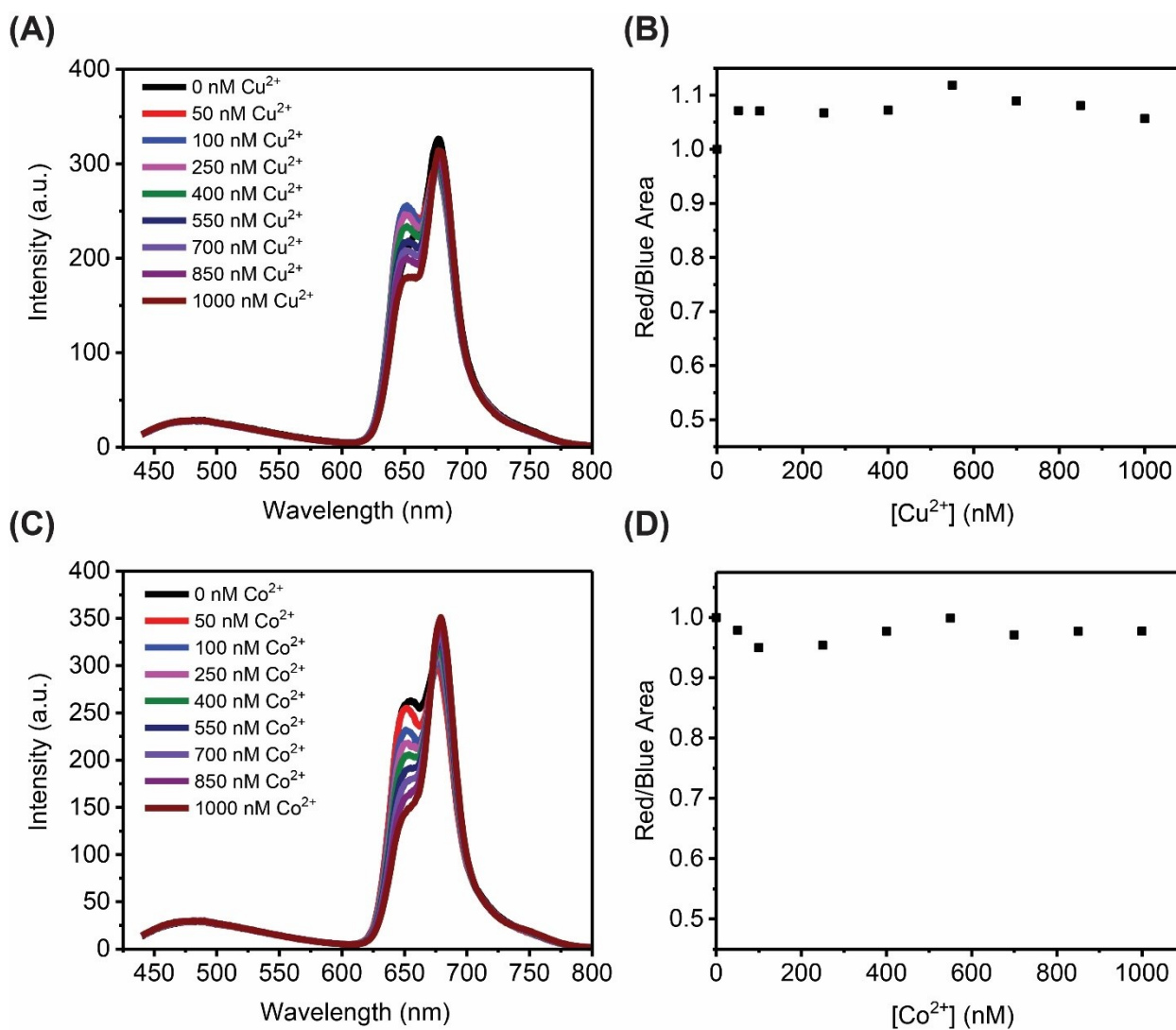


**Figure A 11:** Results of the quenching assay performed on FG-CDs showing changes in the fluorescence spectrum and the Red/Blue area ratio using (A-B)  $\text{Cu}^{2+}$  and (C-D)  $\text{Co}^{2+}$ . No significant quenching is observed with this metal cation.